University of Alberta

Particle Deposition onto Charge Heterogeneous Surfaces in a Radial Impinging Jet System

By

Neda Nazemifard ©

A thesis submitted to the Faculty of Graduate Studies and Research in partial fulfillment of the requirements for the degree of **Master of Science.**

Department of Mechanical Engineering

Edmonton, Alberta
Spring 2006

Your file Votre référence
ISBN: 0-494-13859-9
Our file Notre référence
ISBN: 0-494-13859-9

To my parents.

Abstract

The role of surface charge heterogeneity on particle deposition and particle trajectory has been investigated in the vicinity of a heterogeneous surface inside the radial impinging jet flow geometry. The charge heterogeneity is modelled as concentric circular bands bearing different surface charges. Particle deposition is studied in context of Lagrangian approach (trajectory analysis) as well as Eulerian approach (convection-diffusion equation). The presence of surface charge heterogeneity on the substrate gives rise to an oscillating particle trajectory near the collector surface. It was observed that when the collector is initially fully unfavorable, the presence of charge heterogeneity in form of a small fraction of favorably charged bands enhances the deposition rate substantially. In contrast, when the collector is initially fully favorable, the presence of charge heterogeneity in form of a small fraction of unfavorably charged bands does not affect the particle deposition rate significantly.

Acknowledgements

I would like to take this opportunity to express my gratitude to my supervisor Dr. Subir Bhattacharjee for his constant help and uncountable words of advice. He was the one who showed me by his own example that working on colloidal science can be exciting. I also wish to thank my supervisor Dr. Jacob Masliyah for being the constant source of encouragement during my research. I am always impressed by his sharp insight into physical aspects of the problems. I would like to sincerely thank my both supervisors for providing me opportunities to involve a wide spectrum of research projects and for believing in me to independently conduct a research.

In addition, I wish to thank all of my colleagues in CCFLab including Farshid, Tania, Jeff, and Prodip for creating such a friendly working environment. I would like to specially thank my office mate, Shahnawaz, for his friendship, help in preparation of this thesis, and sharing ideas of research.

Finally, I would like to thank to my dear husband, Farshid, for his support and for listening to my problems when nobody else was there for me.

Edmonton, Alberta — Neda Nazemifard

October 27, 2005

Table of Contents

1 Introduction **1**

1.1 Background and Overview 1

1.2 Objectives and Scope 4

1.3 Organization of the Thesis 6

2 Fluid Flow Field in an Impinging Jet System **10**

2.1 Introduction 10

2.2 Impinging Jet Flow Geometry and Governing Equations 11

2.3 Computational Domain and Boundary Conditions 13

2.4 Numerical Methods 14

2.4.1 Finite Element Analysis Using FEMLAB ® 14

2.4.2 Mesh Generation 16

2.4.3 Validation of Numerical Results 17

2.5 Numerical Simulation Results 19

2.6 Summary 20

3 External Forces **33**

3.1 Introduction 33

3.2 Gravity Force 34

3.3 Hydrodynamic Drag Force 34

3.4 Colloidal Interactions 36

3.4.1 van der Waals Interactions 37

3.4.2 EDL Interactions in the Presence of Charge Heterogeneity 38

3.5 Summary 43

4 Lagrangian Approach: Trajectory Analysis **50**

4.1 Introduction 50

4.2 Trajectory Model 51

4.2.1 Numerical Simulation 53
4.2.2 Collector Deposition Efficiency 54
4.3 Numerical Results for Particle Trajectories 55
4.3.1 Effect of Collector Surface Potential 56
4.3.2 Effect of Band Width at Constant Favorable Area Fraction 59
4.3.3 Effect of Solution Ionic Strength 60
4.4 Particle Distribution Over heterogeneous Substrate 61
4.4.1 Effect of Collector Favorable Area Fraction 63
4.4.2 Effect of Band Width at Constant Favorable Area Fraction 65
4.4.3 Effect of Fluid Velocity 65
4.5 Particle Deposition in Context of Trajectory Analysis 66
4.5.1 Available Model Predicting Particle Deposition Rate: Patch-wise Heterogeneity Model 67
4.5.2 Numerical Results for Collector Deposition Efficiency . . 72
4.6 Summary 76

5 Eulerian Approach: Particle Transport Equation 91
5.1 Introduction 91
5.2 Convection-Diffusion-Migration Equation 92
5.2.1 Particle Diffusion Coefficient 93
5.3 Particle Transport Equation 94
5.4 Computational Domain and Boundary Conditions 96
5.5 Particle Deposition Rate 98
5.6 Numerical Method 99
5.6.1 Numerical Simulation Using FEMLAB® 99
5.6.2 Mesh Generation 100
5.6.3 Numerical procedure: Multi-Geometry Method 102
5.7 Validation of Numerical Results 104
5.7.1 Diffusion Dominant Deposition (Levich Equation) 104
5.7.2 Unfavorable Deposition 107
5.7.3 Variation of Particle Deposition with Particle Size 108
5.8 Numerical Results for Particle Deposition: Homogeneous Collectors 109
5.9 Numerical Results for Particle Deposition: Heterogeneous Collectors 111
5.9.1 Particle Concentration Profile 112

5.9.2 Local Particle Deposition Rate 115
5.9.3 Averaged Particle Deposition Rate 117
5.10 Summary 122

6 Conclusion and Future Work **136**
6.1 Concluding Remarks 136
6.2 Future Works 138

Bibliography **142**

List of Tables

2.1 Dimensions of the Radial Impinging Jet System Used in the Simulations 22
2.2 Dependence of Numerically Obtained Fluid Velocity on the Number of Elements 23

3.1 Physical and Chemical Properties of the System Used in Simulations 44

List of Figures

1.1 A schematic representation of a radial impinging jet system along with the fluid streamlines. 8

1.2 A schematic representation of the distribution of charge heterogeneity on a solid surface. The surface contains two types of surface charges, favorable and unfavorable. 9

2.1 (a) A schematic representations of fluid streamlines and coordinate system of an impinging jet flow field. (b) Computation domain considered for numerically solving of Navier-Stokes equations, Eq. (2.3). In this figure, OA is the axis of symmetry and O is the origin of the cylindrical coordinate system. AB is the exit of the jet nozzle, OD is the collector surface, BC is the exit plane along the jet wall and DC is the outflow. 24

2.2 A schematic representation of the mesh configuration in the computational domain in the impinging jet geometry. 25

2.3 Variation of scaled (a) Radial and (b) Normal components of the fluid velocity with radial distance (r) at two different vertical distances from the substrate (i.e., z=1 μm and z=5 μm). The corresponding Reynolds number is 100. Solid lines denote the numerically calculated fluid velocity using Eq. (2.3). Dashed lines denote the analytically calculated fluid velocity using Eq. (2.6). 26

2.4 Velocity field streamlines inside the impinging jet flow system. These streamlines correspond to *Re* of 100. The nozzle is at the upper left-hand corner (AB), with the main flow moving from left to right. Hatched lines represent the collector surface (OD), nozzle wall and exit plane along the jet wall (BC). 27

2.5 The radial fluid velocity distributions inside the impinging jet flow geometry. These results correspond to Re=100. 28
2.6 The normal fluid velocity distributions inside the impinging jet flow geometry. These results correspond to Re=100. 29
2.7 Variation of scaled radial component of the fluid velocity with radial distance (r) for three different vertical distances from the substrate (i.e., z=1 μm, z=10 μm and z=100 μm). 30
2.8 Variation of scaled normal component of the fluid velocity with radial distance (r) for three different vertical distances from the substrate (i.e., z=1 μm, z=10 μm and z=100 μm). 31
2.9 Dependence of the ratio of radial to normal fluid velocity, $\bar{u}_r/\bar{u}_z$, on radial distance, r, at z=100 μm. The corresponding Re=100. 32

3.1 A schematic representation of the position of a colloidal particle with respect to the collector surface. a_p is the particle radius, z is the normal distance of the particle center from the collector surface, s is the normal surface to surface distance between the particle and the collector surface and h is the dimensionless separation distance between the particle and the collector surface ($h = s/a_p$). 45
3.2 Variation of universal hydrodynamic correction functions with respect to dimensionless separation distance between a particle and the collector surface. 46
3.3 A schematic representation of the modelled surface charge heterogeneity. A collector surface consists of concentric circular bands with alternate negative and positive surface potentials with width of w_n and w_p, respectively. The total width of a negative and a positive band is pitch, p. N_b is a number assigned to each pair of negative and positive band along the radial direction on the collector surface. 47

3.4 (a) Illustration of a step function employed to represent the variation of scaled collector surface potential with r for a heterogeneous collector with $\Psi_s = (-1, +1)$. (b) The resulting values of scaled F_{edl} between a negatively charged particle with $\Psi_p = -1$ and a heterogeneous collector with surface potential as shown in part (a). The values of $\bar{F}_{edl}$ were obtained using Eq. (3.12) for h=0.001, $a_p = 1\ \mu m$. 48

3.5 (a) Illustration of a smoothing sigmoidal function employed to represent the variation of scaled collector surface potential with r for a heterogeneous collector with $\Psi_s = (-1, +1)$. (b) The resulting values of scaled F_{edl} between a negatively charged particle with $\Psi_p = -1$, and a heterogeneous collector with surface potential as shown in part (a). The values of $\bar{F}_{edl}$ were obtained using Eq. (3.12) for h=0.001, $a_p = 1\ \mu m$. 49

4.1 A schematic illustration of the trajectory of a negatively charged particle over a micropatterned substrate consisting of alternate negative and positive bands. Plain stripes represent negatively charged regions and shaded stripes represent positively charged regions. 79

4.2 A schematic representation of limiting trajectory. Dashed lines represent two particle trajectories. The limiting trajectory corresponding to the distance R_c from the stagnation point on the collector starts from the jet tip at the radial distance of $r_{0,\ lim}$. All the other trajectories start at the jet tip with the radial position less than $r_{0,\ lim}$ will terminate on the collector inside the circle with radius R_c. 80

4.3 Illustration of particle trajectories obtained by numerically solving of Eq. (4.8) for different values of collector surface potentials. Dashed lines represent the particle trajectories over an unfavorable surface. Dotted lines denote particle trajectories over a favorable surface. Solid lines represent the particle trajectories over a heterogeneous charged surface with $w_n = w_p = 2\ \mu m$. The simulations were obtained for two different regions (a) Near Stagnation point and (b) Far from stagnation point. 81

4.4 (a) Illustration of particle trajectories over a heterogeneous charged surface consists of alternate negative and positive bands with scaled surface potentials of -2 and +2, respectively. (b) Zoomed in trajectories inside the dashed box in Figure 4.4a. Λ represents the wavelength of the oscillating particle trajectory. 82
4.5 Illustration of particle trajectories in impinging jet flow field over a charged substrate for two different values of solution ionic strength i.e. 10^{-3}M and $10^{-3.5}$M. Dashed lines denote the particle trajectories over a homogeneous, fully favorable substrate $\Psi_s = +1$. Solid lines denote particle trajectories over a micropatterned substrate consisting of alternate negative and positive bands, $w_n = w_p = 2\ \mu m$, and $\Psi_s = (-1, +1)$. 83
4.6 A schematic depiction of procedure used to evaluate the inaccessible part at the beginning of favorable stripes. Each favorable stripe was discretized into N segments. Starting from the end of each such segment, the trajectory equations were solved backward to determine the initial release location of the particle. The initial release position was deemed feasible if it originated from within the impinging jet nozzle (solid line). Termination of the trajectory at any other point in the computational domain constituted an infeasible trajectory (dashed line). 84
4.7 Accessible fraction of a favorable band (AF_F) presented for all of the favorable bands on the collector surface. The horizontal axis represents the band number along the radial direction on the collector surface. The results correspond to different values of positive and negative band width while the pitch is maintained constant and equal to 20 μm. $\Psi_s = (-2, +2)$, $a_p = 1\ \mu m$, $I = 10^{-3.5}$M. 85
4.8 Accessible fraction of a favorable band (AF_F) presented for all of the favorable bands on the collector surface for three different values of pitch. The horizontal axis denotes the band number along the radial direction on the collector surface. The favorable area fraction of the collector is maintained constant and equal to 50%. All the other parameters are the same as in Figure 4.7 . . 86

4.9 Accessible fraction of a favorable band (AF_F) presented for all of the favorable bands on the collector surface for different values of fluid velocity corresponding to Re=50, 100 and 200. The collector surface consists of alternate favorable and unfavorable bands with the width of 5 μm. The favorable are fraction of the collector is 50%. All the other parameters are the same as in Figure 4.7 . . 87

4.10 The dependence of reduced deposition efficiency (η/η_f) on favorable area fraction of the collector ($\lambda_{patterned}$). Dashed line denoted the effective deposition efficiency obtained using the original patchwise heterogeneity model, Eq. (4.14). Symbol-lines represent the effective deposition efficiency obtained using the modified patchwise heterogeneity model, Eq. (4.17) for two different distances from the stagnation point, $R_c = 60$ μm (square-legend line) and $R_c = 800$ μm (circle-legend line). All parameters are the same as in Figure 4.7. 88

4.11 The dependence of the collector deposition efficiency (η) on the radial distance from the stagnation point. R_c represents the distance of the end of each favorable band from the stagnation point. Solid line denotes the deposition efficiency for a homogeneous fully favorable collector (η_f), while other lines denote the collector deposition efficiency for a heterogeneous micropatterned collector. All the other parameters are the same as in Figure 4.7. 89

4.12 The dependence of the scaled collector deposition efficiency (η/η_f) on the collector favorable area fraction. The collector radius, R_c, is assumed to be 300 μm. Triangle-legend line denotes the deposition efficiency for a heterogeneous collector predicted by the original patchwise heterogeneity model while circle-legend line denotes the deposition efficiency for a heterogeneous collector predicted by the modified patchwise heterogeneity model. Square-legend line denotes the deposition efficiency for a heterogeneous collector calculated using trajectory model. 90

5.1 (a) A schematic presentation of impinging jet system geometry. The dashed rectangular depicts the computational domain shown in detail in part(b). (b) Computational domain used in solving convection-diffusion equation by finite element method. 124

5.2 Variation of overall deposition rate with respect to Peclet number for a homogeneous fully favorable collector in the absence of energy barrier, inside the stagnation point region. Solid line denotes the values of Sh_{ave_f} calculated by Levich equation whereas symbols represents the Sh_{ave_f} obtained by solving convection-diffusion equation numerically. 125

5.3 Variation of overall deposition rate with respect to flow Reynolds number for a homogeneous unfavorable collector in the presence of energy barrier, inside the stagnation point region. Solid line denotes the values of Sh_{ave} caculated numerically by Dabros and van de Ven for three different values of double layer parameter, Dl . Dashed line represents the Sh_{ave} obtained by solving convection-diffusion equation numerically. 126

5.4 Variation of overall deposition efficiency, η_f, with respect to particle radius for a homogeneous fully favorable collector inside the stagnation point flow domain. Solid line with circular symbols denotes the values of η_f calculated by solving convection-diffusion equation numerically ($\Psi_s = +1$, $\Psi_p = -1$, $Re = 100$, $I = 10^{-3}$ M). Dashed line denoted the η_f obtained using Levich equation. 127

5.5 Variation of particle concentration with the vertical distance from the collector surface, z, at the stagnation point, $r = 0$. The results are obtained by solving convection-diffusion numerically inside the impinging get flow geometry. Solid line depicts the particle concentration profile over a homogeneous fully favorable collector with $\Psi_s = +1$. Dashed line denotes the particle concentration profile over a homogeneous fully unfavorable collector with $\Psi_s = -1$. All the other parameters are the same as in Figure 5.4. . . . 128

5.6 Variation of local particle deposition rate, Sh with the radial distance from the collector surface, r. Solid line depicts the particle concentration profile over a homogeneous fully favorable collector with $\Psi_s = +1$. Dashed line denotes the particle concentration profile over a homogeneous fully unfavorable collector with $\Psi_s = -1$. All the other parameters are the same as in Figure 5.4. 129

5.7 Variation of scaled particle concentration with the radial distance from the stagnation point, r, at two different vertical distances from the collector surface, (a) $s = 5\ nm$ where the regions between $500\ \mu m < r < 600\ \mu m$ is enlarged in (b).(c)$s = 72\ nm$. . . 130

5.8 Variation of scaled radial (a) convective (b) diffusive flux on the radial distance from the stagnation point, r, at the vertical distance from the collector surface around the secondary minimum. Particle radius is assumed to be 1 μm. All the other parameters are the same as in Figure 5.7 131

5.9 Variation of scaled radial (a) convective (b) diffusive flux on the radial distance from the stagnation point, r, at the vertical distance from the collector surface around the secondary minimum. Particle radius is assumed to be 0.1 μm. All the other parameters are the same as in Figure 5.7 132

5.10 Variation of local particle deposition rate, Sh, with radial distance from the stagnation point, r, at the collector surface. The region with $0 < r < 100\ \mu m$ of this figure is enlarged in part (b). The region with $500\ \mu m < r < 600\ \mu m$ of this figure is enlarged in part (c). 133

5.11 Variation of Sh_{ave} with band number, N_b for four particle sizes i.e., (a) $a_p = 1\ \mu m$, (b) $a_p = 0.5\ \mu m$, (c) $a_p = 0.25\ \mu m$, (d) $a_p = 0.1\ \mu m$. Square-legend line denotes Sh_{ave} over a heterogeneous collector with $\psi_s = (-1, +1)$ obtained by numerical simulation. Triangle-legend line denotes Sh_{ave} predicted by the patchwise heterogeneity model over a heterogeneous collector with $\psi_s = (-1, +1)$ and circle-legend line denotes Sh_{ave_f} over a homogeneous fully favorable collector with $\psi_s = +1$.All the other parameters are the same as in Figure 5.7. 134

5.12 Variation of scaled overall particle deposition rate, Sh_{ave}/Sh_{ave_f}, with favorable area fraction of the collector, $\lambda_{patterned}$. The square-legend line denotes the overall deposition rate obtained by solving convection-diffusion equation. The triangle-legend line denotes values of overall deposition rate obtained by the original patchwise heterogeneity model. The circle-legend line denotes values of overall deposition rate obtained by the modified patchwise heterogeneity model. All the other parameters are the same as in Figure 5.7. 135

List of Symbols

A	Hamaker constant [J]
Ad	dimensionless adhesion number
a_p	particle radius [m]
c	particle concentration [mol m^{-3}]
c_∞	bulk particle concentration [mol m^{-3}]
$\bar{c}$	scaled particle concentration (c/c_∞)
D_∞	particle diffusion coefficient in bulk medium [m^2s^{-1}]
$\underline{\underline{D}}$	particle diffusion coefficient tensor [m^2s^{-1}]
Da	dimensionless electrostatic double layer asymmetry parameter
Dl	dimensionless electrostatic double layer parameter
e	electronic charge [C]
f_i	universal hydrodynamic correction functions
$\vec{F}$	external force acting on a particle [N]
F_r	sum of the forces in r-direction [N]
F_z	sum of the forces in z-direction [N]
F_{Br}	Brownian force [N]
F_{edl}	electrostatic double layer force [N]
F_g	gravity force [N]
F_{Hyd}	hydrodynamic force, fluid drag [N]
F_{vdw}	van der Waals force [N]
h	dimensionless surface to surface separation distance (s/a_p)
$\vec{g}$	gravitational acceleration vector [ms^{-2}]
I	solution ionic strength [M]
$\vec{j}$	particle flux [mol $m^{-2}s^{-1}$]
$\bar{j}$	scaled particle flux ($\frac{ja_p}{D_\infty c_\infty}$)
k_b	Boltzmann constant [JK^{-1}]
L	vertical distance of the impinging jet from the collector surface [m]
m	mass of each particle [kg]
N_A	Avogadro number [mol^{-1}]
N_b	band number in radial direction

n_∞	number of ions in a solution [m^{-3}]
p	pitch of the charge heterogeneity [m]
p_f	fluid pressure [Pa]
$\bar{p}_f$	dimensionless fluid pressure ($\frac{p_f}{\rho_f U_\infty^2}$)
p_{atm}	pressure of the atmosphere [Pa]
Pe	Peclet number ($\frac{U_\infty a_p}{D_\infty}$)
Pe_s	stagnation flow Peclet number ($\frac{2\alpha\ a_p^3}{D_\infty}$)
r	radial distance [m]
$\bar{r}$	dimensionless radial distance (r/a_p)
R_c	collector radius [m]
Re	Reynolds number ($\frac{\rho_f U_\infty R_{jet}}{\mu_f}$)
R_{jet}	radius of the jet tip [m]
Sh	local Sherwood number
Sh_f	local Sherwood number over a fully favorable collector
Sh_{fav}	local Sherwood number over a favorable band on the collector surface
Sh_u	local Sherwood number over a unfavorable band on the collector surface
Sh_{ave}	averaged Sherwood number
Sh_{ave_f}	averaged Sherwood number over a fully favorable collector
s	surface to surface separation distance [m]
S_f	area of the favorably charged part on the collector surface [m^2]
S_{total}	total area of the collector surface [m^2]
t	time [s]
$\bar{t}$	dimensionless time
T	absolute temperature [K]
u_r	radial fluid velocity [ms^{-1}]
u_z	normal fluid velocity [ms^{-1}]
U_∞	average fluid velocity in jet [ms^{-1}]
v_r	radial component of particle velocity [ms^{-1}]
v_z	normal component of particle velocity [ms^{-1}]
w_p	width of positive band [μm]
w_n	width of negative band [μm]
$w_{accessible}$	width of the accessible part of favorable band [μm]
z	vertical (normal) distance [m] or valence of ions in symmetrical electrolyte
$\bar{z}$	dimensionless vertical distance (z/a_p)

Greek Alphabets

α_s	impinging jet flow coefficient [1/ms]
$\bar{\alpha}$	dimensionless impinging jet flow coefficient
δ_m	cut-off separation distance
ϵ	dielectric constant
ϵ_0	permittivity of vacuum [C/Vm]
η	collector deposition efficiency
η_f	deposition efficiency of a fully favorable collector
η_{patch}	deposition efficiency predicted by the patchwise heterogeneity model
η_u	deposition efficiency of a fully unfavorable collector
$\lambda_{patterned}$	nominal favorable area fraction of the collector
$\lambda_{effective}$	actual (real) favorable area fraction of the collector
Λ	wavelength of the oscillating particle trajectory [m]
κ	inverse Debye length [m^{-1}]
μ_f	viscosity of the fluid [$Nm^{-2}s$]
ψ_p	particle surface potential [V]
ψ_s	collector surface potential [V]
Ψ_p	scaled particle surface potential
Ψ_s	scaled collector surface potential
Ψ_{sp}	scaled surface potential of positive bands on the collector surface
Ψ_{sn}	scaled surface potential of negative bands on the collector surface
ρ_f	fluid density [kgm^{-3}]
ρ_p	particle density [kgm^{-3}]
υ	kinematic viscosity of the fluid [m^2s^{-1}]
Ω	computational domain

Abbreviations

AF_F	available fraction of favorable band on the collector surface
CD	convection-diffusion model
EDL	electrostatic double layer

Chapter 1

Introduction

1.1 Background and Overview

Particle transport from flowing suspensions onto solid substrates (known as collectors) followed by the attachment of these particles to the collector surface is defined as particle deposition. Particle deposition is of great importance in many natural and industrial processes [Hirtzel and Rajagopalan, 1985, Adamczyk, 1989] such as deep bed filtration [Rajagopalan and Tien, 1977, Wnek *et al.*, 1975], paper making, detergency and biological applications such as adhesion of bacteria and viruses to human organs [Bitton *et al.*, 1991]. Consequently, particle deposition is receiving attention from both an applied [Boluk and van de Ven, 1990, McCarthy, 1989] and a fundamental point of view [Adamczyk and van de Ven, 1981, Adamczyk, 1989]. Different flow regimes have been developed to study particle deposition under controlled mass transfer conditions such as the rotating disk system [Dabros and Adamczyk, 1979, Prieve and Lin, 1980], both the radial and slot impinging jet geometry [Adamczyk *et al.*, 1986], and the parallel plate flow system [Adamczyk and van de Ven, 1981].

The impinging jet system has been a popular tool for studying particle deposition in various engineering and applied science disciplines [Adamczyk *et al.*, 1986, Elimelech, 1995]. There are two types of impinging jet system, namely slot impinging jet system and radial impinging jet system. A schematic representation of the radial impinging jet system is shown in Figure 1.1. In the

radial impinging jet system, a fluid stream impinges vertically on a flat surface (collector) and flows away radially in all directions. The flow configuration in the impinging jet system can be categorized to two distinctive regions. In the vicinity of the stagnation point, the fluid velocity is almost normal to the collector surface whereas far from the stagnation point, the fluid velocity is almost parallel to the collector surface. This attributes a unique feature to the impinging jet system. Due to the nature of the fluid velocity, the thicknesses of the hydrodynamic and diffusion boundary layers are constant in the vicinity of the stagnation point. This means that in the vicinity of the stagnation point, there is a uniform probability for particle deposition on the collector surface while far from the stagnation point, the probability of particle deposition becomes dependent on the position over the collector surface and is not uniform anymore. As a result, the particle deposition in the impinging jet system manifests both uniform and nonuniform deposition behaviours close and far from the stagnation point. Regarding the experimental studies, in an impinging jet flow system, it is possible to observe the deposition of the particles directly by microscopes when a transparent collector is being used. Furthermore, the deposition of particles inside an impinging jet flow can be considered as an approximation for deposition in more complicated systems such as spherical or cylindrical collectors. Different theoretical and experimental studies have been conducted to investigate deposition of particles inside the impinging jet system [Dabros and van de Ven, 1983, Adamczyk *et al.*, 1986].

In context of theoretical studies, there are two approaches to the study of particle deposition [Masliyah, 1994, Adamczyk, 1989]. The first method is the Eulerian approach where the distribution of particles in space is evaluated from a continuum picture. The generalized convection-diffusion equation is solved for the colloidal particles subjected to appropriate boundary conditions. The second method is the Lagrangian approach. Here, the attention is focused on a single particle trajectory based on Newton's second law of motion. The particle trajectories are obtained by solving the trajectory equations for colloidal parti-

cles. This leads to determination of limiting trajectories, which can be employed to determine the particle deposition values. Since the trajectory analysis is deterministic, most of the literature studies employing the Lagrangian approach do not consider the Brownian motion of the particles due to the mathematical complexities involved. However, if the Brownian effect is included in trajectory analysis, both Eulerian and Lagrangian approaches should, in principle, yield similar result [Masliyah, 1994, van de Ven, 1989].

Most of the deposition related studies in literature have investigated particle deposition over homogeneous surfaces. However, solid surfaces in many engineering and natural systems exhibit both physical and chemical heterogeneities [Vaidyanathan and Tien, 1991, Kihira *et al.*, 1992, Song *et al.*, 1994, Shellenberger and Logan, 2002]. The presence of physical heterogeneity results in surface roughness which has been the subject of interest in studying the particle deposition [Shellenberger and Logan, 2002]. The chemical heterogeneity on the other hand, generally results in an uneven or heterogeneous surface charge distribution at various length scales [Richmond, 1974, Khachatourian and Wistrom, 1998, Vreeker *et al.*, 1992]. A schematic representation of a surface containing charge heterogeneity is shown in Figure 1.2. In this figure, the surface contains two types of surface charges, namely favorable and unfavorable with respect to particle deposition. Throughout this study, the negatively charged region acts as a unfavorable region and positively charged region acts as a favorable region with respect to deposition. Some of the sources of chemical heterogeneity include differences in constituent minerals, chemical imperfections, and surface bound impurities [Walz, 1998]. Numerous large scale studies on particle deposition and capture onto charge heterogeneous substrates, generally pertaining to porous media transport, have been conducted [Elimelech, 1995]. Most of the theoretical studies on this subject resort to a continuum type approach in describing the charge heterogeneity of the substrate. In other words, the existing modelling techniques do not exactly track the distribution of the charge heterogeneity on a substrate, instead focusing on a macroscopic definition of

heterogeneity based on surface area fractions of the collectors bearing different charges [Song *et al.*, 1994]. A common approach is to define two types of surface charge locations on a given collector (for instance, positive and negative), assigning the surface area fraction occupied by one type of charge, and using a two site averaging process generally referred to as the patchwise heterogeneity model [Song *et al.*, 1994]. Such an approach works remarkably well for granular porous media, where the large length and time scales of the transport process are amenable to macroscopic spatial averaging.

More recently, it has become increasingly clear that while patchwise heterogeneity models provide reasonably accurate description of macroscopic charge heterogeneity, it is not very accurate when the charge heterogeneous patches have a comparable length scale to the particle size [Elimelech *et al.*, 2003]. In most microfluidic and microscale transport processes, we may encounter surfaces where the charged patches have dimensions comparable to the suspended particles. In such cases, the coupled influence of particle-substrate colloidal interactions and the hydrodynamic forces imposed by the flow field are susceptible to considerable modifications due to the influence of chemical heterogeneity. This implies that the simple averaging methods such as patchwise heterogeneity model may not be adequate to predict the particle deposition in the presence of micro-scale charge heterogeneity. It is therefore of great importance from both theoretical and practical perspective, to fundamentally explore the effects of micro-scale charge heterogeneity on governing mechanisms of the particle deposition process.

1.2 Objectives and Scope

Naturally occurring deposition substrates generally contain surface charge heterogeneity that are randomly distributed, of arbitrary geometrical shapes, and having widely varying chemical properties. Consequently, it becomes extremely difficult to systematically study the influence of charge heterogeneity on the

particle deposition behavior on to such substrates. In this context, it might be pertinent to systematically create such heterogeneity by chemically patterning homogeneous model substrates. Studying particle deposition on to such a model substrate where the heterogeneity is artificially created can lead to considerable insight regarding how the deposition behavior is influenced by the presence of surface charge heterogeneity. If the distribution of the heterogeneous patches is known *a priori*, elucidation of their influence on particle deposition becomes more tractable.

In this thesis, we develop a theoretical model to investigate the effect of microscopic surface charge heterogeneity on particle trajectories and particle deposition inside the radial impinging jet system. The objectives of this thesis can be summarized as

1. In order to systematically investigate the role of charge heterogeneity on the particle deposition behavior, the charge heterogeneity on the collector surface is modelled as alternate stripes or bands of microscopic dimensions bearing positive and negative charge. In a radial impinging jet flow context, such stripes can be construed as concentric circular rings bearing different surface potentials.

2. The role of hydrodynamic interactions in the particle deposition process is investigated by first solving the velocity field in the whole radial impinging jet geometry. Due to the nature of the fluid velocity in this geometry, the collector in the impinging jet system acts as a uniform collector close to the stagnation point whereas far from the stagnation point, it acts as a non-uniform collector with respect to particle deposition. This enables us to investigate the role of surface charge heterogeneity in the scope of both uniform and non-uniform collectors.

3. A trajectory analysis based on Lagrangian approach has been developed to study the particle trajectory and particle deposition behaviour in the vicinity of a charge heterogeneous collector. The trajectory model takes

into account the effects of hydrodynamic interactions as well as external forces.

4. In order to support the results obtained by trajectory analysis and also achieve a better understanding about the particle deposition behaviour in presence of micro-scale charge heterogeneity, a convection-diffusion-migration model based on Eulerian approach has been developed. This model provides the particle concentration distribution and particle deposition rate in the vicinity of the micro-scale charge heterogeneity.

In general, this work is intended to conduct a systematic theoretical investigation in the role of micro-scale charge heterogeneity on the particle distribution and particle trajectory in the vicinity of a charge heterogenous collector in the radial impinging jet system. The study is geared toward prediction of the initial deposition rate on a clean collector. To our knowledge, this has been the first time that the role of charge heterogeneity on deposition process is studied systematically using the available theoretical methods such as Lagrangian and Eulerian approaches.

1.3 Organization of the Thesis

In this chapter, the overall objectives and scope of the study have been delineated. The general introduction and the motivation behind this research have been also laid out.

In Chapter 2, a numerical simulation based on finite element analysis is developed to calculate the fluid velocity in the entire impinging jet system.

The external forces that a charged particle is subjected to inside the impinging jet system in the vicinity of a heterogeneous substrate are explained in detail in Chapter 3. The corresponding expression for each of these forces are also provided in this chapter. Furthermore, a detailed description of modelling surface charge heterogeneity and definition of pertinent variables are given in Chapter 3 as well.

In Chapter 4, a trajectory analysis of a charged particle based on Lagrangian approach inside the impinging jet flow system in the vicinity of a charge heterogeneous collector is presented. The results of solution of velocity field obtained in Chapter 2 and the external forces described in Chapter 3 are put in use for calculating particle trajectories. The trajectory equations are then solved numerically. The limiting trajectory method has been incorporated to obtain the particle deposition rate over both homogeneous and charge heterogeneous collectors. The available model known as patchwise heterogeneity model predicting particle deposition over heterogeneous surfaces is described in detail in Chapter 4 as well. Finally, the particle deposition rate obtained by numerically solving the trajectory equations is compared with those predicted by the patchwise heterogeneity model.

In Chapter 5, the Eulerian approach is adopted to calculate particle deposition rate over heterogeneous collectors by solving the convection-diffusion-migration equation inside the impinging jet system. The convection-diffusion-migration equation is solved numerically using the finite element method. A detailed numerical simulation scheme is provided. The particle deposition rate obtained by numerically solving of convection-diffusion equation is then compared with those obtained by trajectory analysis, as well as, those predicted by the patchwise heterogeneity model.

Finally, Chapter 6 summarizes the contributions made by this study and conclusions obtained during this research. This chapter also provides some recommendations for future studies on the role of charge heterogeneity on particle deposition.

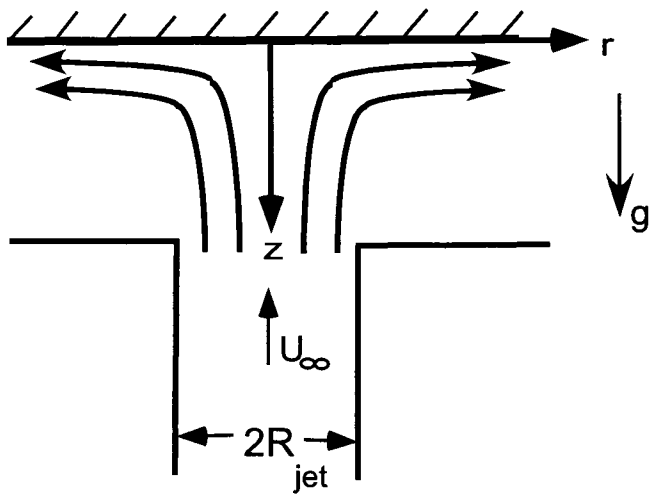

Figure 1.1: A schematic representation of a radial impinging jet system along with the fluid streamlines.

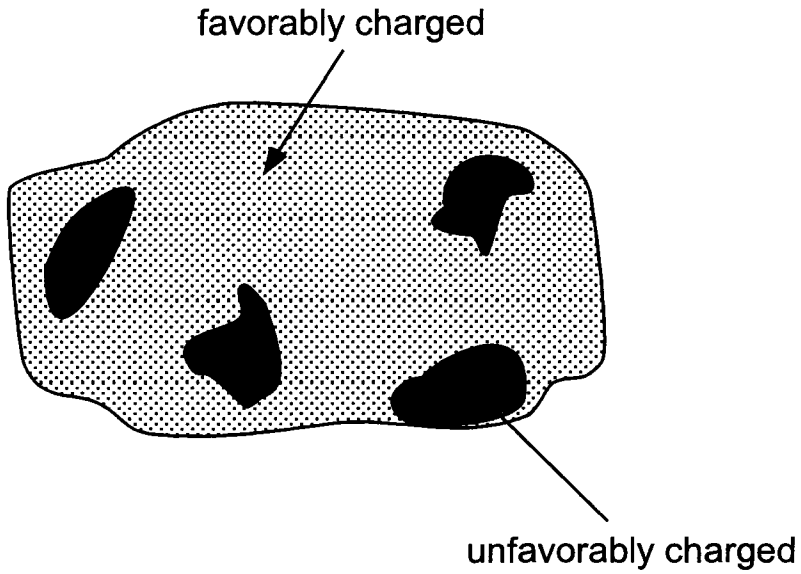

Figure 1.2: A schematic representation of the distribution of charge heterogeneity on a solid surface. The surface contains two types of surface charges, favorable and unfavorable.

Chapter 2

Fluid Flow Field in an Impinging Jet System

2.1 Introduction

The movement of the particles suspended in a fluid is affected by the fluid motion. The fluid exerts a drag force on the solid particles, which are convected along the flow direction. In obtaining particle deposition rates, knowledge of fluid velocity is required regardless whether Lagrangian or Eulerian approaches are employed for particle transport. In context of Lagrangian approach, the fluid velocity should be determined first to calculate the drag force exerted on the particles. In context of Eulerian approach, the fluid velocity should be determined first to calculate the convection term in the convection-diffusion-migration equation. Therefore, an understanding of the fluid flow field is essential to predict the particle motion induced by the fluid velocity. In this chapter, we calculate the fluid velocity in the entire flow field in the impinging jet geometry. The geometry of the radial impinging jet flow will be described first then the equations governing fluid velocity in such a geometry will be explained. These equations are then solved numerically using finite element analysis. The numerical methods and the computational domain will be described in detail as well. As it is well-documented in literature [Adamczyk *et al.*, 1986, Elimelech, 1995], the flow field inside impinging jet system near the stagnation point region follows

the stagnation flow patterns. For such flow patterns, there are some analytical expressions available that provide the fluid velocity inside stagnation flow region which are only valid in a small region close to the stagnation point. These analytical expressions are employed to examine the validity of the present numerical methods. Increasing the radial distance from the stagnation point, the fluid velocity changes from the stagnation point flow patterns to the parallel flow patterns in the vicinity of the collector surface. The expecting velocity streamlines in the radial impinging jet system are shown in Figure 2.1a.

2.2 Impinging Jet Flow Geometry and Governing Equations

A schematic representation of the radial impinging jet system is illustrated in Figure 2.1a. A colloidal suspension is introduced to the system through a circular jet of radius R_{jet} with an average velocity of U_∞. The fluid then impinges vertically on the collector surface (hatched line) and flows radially outward from the impinging jet flow domain. The separation distance between the collector surface and the impinging jet tip is denoted by L. The geometry of the system described here ensures the radial symmetry and allows use of axisymmetric cylindrical coordinate system. The origin of cylindrical coordinate system is located at the stagnation point.

In this study, a steady state, laminar flow of an incompressible Newtonian fluid is considered. Therefore, the flow fields are governed by continuity and momentum conservation equations ,which, in an axisymmetric cylindrical coordinate system, are written as

Continuity equation

$$\frac{1}{r}\frac{\partial(ru_r)}{\partial r} + \frac{\partial u_z}{\partial z} = 0 \tag{2.1}$$

Momentum conservation

$$u_r\frac{\partial u_r}{\partial r} + u_z\frac{\partial u_r}{\partial z} = -\frac{1}{\rho_f}\frac{\partial p_f}{\partial r} + \frac{\mu_f}{\rho_f}\left[\frac{\partial}{\partial r}\left[\frac{1}{r}\frac{\partial(ru_r)}{\partial r}\right] + \frac{\partial^2 u_r}{\partial z^2}\right] \tag{2.2a}$$

$$u_r\frac{\partial u_z}{\partial r}+u_z\frac{\partial u_z}{\partial z}=-\frac{1}{\rho_f}\frac{\partial p_f}{\partial z}+\frac{\mu_f}{\rho_f}\left[\frac{1}{r}\frac{\partial}{\partial r}\left[r\frac{\partial u_z}{\partial r}\right]+\frac{\partial^2 u_z}{\partial z^2}\right] \tag{2.2b}$$

where u_r and u_z are the fluid velocity components along the r and z directions, respectively. ρ_f and μ_f are the density and viscosity of the liquid, respectively. The above set of equations can be nondimensionalized as follows

$$\frac{1}{\bar{r}}\frac{\partial(\bar{r}\bar{u}_r)}{\partial\bar{r}}+\frac{\partial\bar{u}_z}{\partial\bar{z}}=0 \tag{2.3a}$$

$$\bar{u}_r\frac{\partial\bar{u}_r}{\partial\bar{r}}+\bar{u}_z\frac{\partial\bar{u}_r}{\partial\bar{z}}=-\frac{\partial\bar{p}_f}{\partial\bar{r}}+\frac{1}{Re}\frac{R_{jet}}{a_p}\left[\frac{\partial}{\partial\bar{r}}\left[\frac{1}{\bar{r}}\frac{\partial(\bar{r}\bar{u}_r)}{\partial\bar{r}}\right]+\frac{\partial^2\bar{u}_r}{\partial\bar{z}^2}\right] \tag{2.3b}$$

$$\bar{u}_r\frac{\partial\bar{u}_z}{\partial\bar{r}}+\bar{u}_z\frac{\partial\bar{u}_z}{\partial\bar{z}}=-\frac{\partial\bar{p}_f}{\partial\bar{z}}+\frac{1}{Re}\frac{R_{jet}}{a_p}\left[\frac{1}{\bar{r}}\frac{\partial}{\partial\bar{r}}\left[\bar{r}\frac{\partial\bar{u}_z}{\partial\bar{r}}\right]+\frac{\partial^2\bar{u}_z}{\partial\bar{z}^2}\right] \tag{2.3c}$$

where

$$\bar{u_r}=\frac{u_r}{U_\infty} \qquad \bar{r}=\frac{r}{a_p} \qquad \bar{p}_f=\frac{p_f}{\rho_f U_\infty^2}$$

$$\bar{u_z}=\frac{u_z}{U_\infty} \qquad \bar{z}=\frac{z}{a_p} \qquad Re=\frac{\rho_f R_{jet}U_\infty}{\mu_f}$$

It is worth noting here that in the present study, we used particle radius (a_p) to nondimesionalize the length variables in the Navier-Stokes equations while in literature, the nozzle radius (R_{jet}) has often been used to nondimesionalize the length variables in the Navier-Stokes equation for an impinging jet flow system. This is because in the present study, a_p has been also used to nondimesionalize the trajectory equation (Chapter 4) and the convection-diffusion-migration equation (Chapter 5).

In order to obtain the fluid velocity, the above non-linear, second order partial differential equations should be solved numerically. This requires that the computational domain and the appropriate boundary conditions be specified first.

2.3 Computational Domain and Boundary Conditions

Figure 2.1b illustrates the computational domain that has been considered for this study. In this figure, OA is the axis of symmetry and its length is equal to L. O is the stagnation point and the origin of the cylindrical coordinate system. AB represents the exit of the jet nozzle and is equal to the nozzle radius, R_{jet}. OD denotes the collector surface. BC is the exit plane along the jet wall and parallel to the exiting flow. DC is the outflow boundary. The dimensions of the computational domain, OABCD, used in the simulation are provided in Table 2.1.

The boundary conditions for the above set of partial differential equations in the specified domain are as follows; along all of the solid surfaces inside the computational domain including collector surface (OD) and the exit plane (BC), the no-slip boundary condition is applied. The boundary condition along the symmetry axis (OA) is defined such that it conforms to the radial symmetry of the system. As mentioned before, AB represents the jet nozzle which is assumed to be circular. Therefore, the velocity along this line has a parabolic, fully-developed profile expressed as Poiseuille's flow.

The boundary condition along the outflow boundary (DC) is difficult to define regardless of the numerical method employed since the velocity along this line remains unknown until the numerical solution has been achieved. Fortunately, similar studies in literature [Yang *et al.*, 1998] reveals that the boundary condition set at the outflow region has little influence on the solution of velocity field as long as this line is located far enough from the jet. In this study, considering the geometry of the system, we assume that the fluid velocity is normal to this exit plane. All the lengths are nondimensionalized with respect to particle size, a_p.

The above boundary conditions can be summarized as

$$\bar{u}_r = 0 \ , \ \frac{\partial \bar{u}_z}{\partial \bar{r}} = 0 \qquad\qquad \partial\Omega \in OA \qquad\qquad (2.4a)$$

$$\bar{u}_r = \bar{u}_z = 0 \qquad \partial\Omega \in OD, BC \tag{2.4b}$$

$$\bar{u}_r = 0 \ , \ \bar{u}_z = -2\left[1 - (\frac{a_p\bar{r}}{R_{jet}})^2\right] \qquad \partial\Omega \in AB \tag{2.4c}$$

$$\bar{u}_z = 0 \ , \ \bar{p} = \bar{p}_{atm} \qquad \partial\Omega \in DC \tag{2.4d}$$

where $\partial\Omega$ is the boundary of the computational domain.

2.4 Numerical Methods

The flow governing equations, Eq. (2.3), along with boundary conditions ,Eq. (2.4), can now be solved numerically. In literature, several approaches have been developed to solve the above set of partial differential equations [Polat, 1991, Deshpande and Vaishnav, 1982, Dabros and van de Ven, 1983]. In this study, a finite element analysis is employed to solve the governing Navier-Stokes equations. The numerical solution provides the fluid velocity in the entire flow field inside the radial impinging jet system.

2.4.1 Finite Element Analysis Using FEMLAB ®

The numerical solution of Navier-Stokes equation, Eq. (2.3), along with boundary conditions ,Eq. (2.4) is obtained using finite element analysis. The unknowns in the Navier-Stokes equations are $\bar{u_r}, \bar{u_z}$, and $\bar{p_f}$. The starting point for the finite element analysis is a mesh, a partition of the geometry into small units of a simple shape. In 2D, the method partitions the subdomains into mesh elements. Once the mesh is defined, the finite element method approximates the exact solution of each unknown, for instance $\bar{u}_r$, as a combination of piece-wise polynomial shape functions with a finite number of parameters, the so-called degrees of freedom, on each element. In this study, the quadratic shape functions φ_i with U_i degrees of freedom are used where $\varphi_i = 1$ at node i and $\varphi_i = 0$ at all other nodes. The solution of $\bar{u_r}$ for an element can be written in terms of shape functions and degrees of freedom as

$$\bar{u_r} = \sum_i U_i\varphi_i \tag{2.5}$$

where i is the number of nodes inside an element. The same method is employed for calculating $\bar{u_z}$ and $\bar{p_f}$.

Inserting this approximation into the weak form of the equation governing the fluid velocity inside the computational framework, generates a system of equations for the degrees of freedom. Solving this system of equations provides the solution for $\bar{u_r}, \bar{u_z}$, and $\bar{p_f}$ in the computational domain. More details regarding implementation of finite element approximation in solving partial differential equations is available in standard textbooks [Zienkiewicz, 1989].

Recently, several commercial finite element solvers of general nature have been available which can significantly simplify the implementations of such techniques by preserving the stringent accuracy of the results. In this context, the whole solution methodology in this study was conducted using the commercially available software FEMLAB® 3.1 (COMSOL, Inc., USA), which can be run either as a programmable toolbox on MATLAB (The MathWorks, Inc., USA), or as a simple graphical user interface (GUI) for solving the partial differential equations using the finite element method. The software can run the finite element analysis together with adaptive meshing and local error control using a variety of numerical solvers until a global convergence criterion is achieved. Once this convergence is obtained, the program is terminated automatically.

FEMLAB® provides a number of application modules that consist of predefined templates and user interfaces already set up with equations and variables for different areas of physics. Using the predefined momentum conservation model inside the Chemical Engineering Module of FEMLAB®, the governing Navier-Stokes equation, Eq. (2.3), can be modelled by simply defining the corresponding constants and coefficients of the Navier-Stokes equation for the specified application mode. The existing predefined boundary conditions in the momentum conservation application mode of FEMLAB® support all of the boundary conditions in Eq. (2.4). This allows the implementation of the boundary conditions without any further modifications. More details about implementing partial differential equation in FEMLAB® can be found

in FEMLAB® user's manual.

The next step in solving the partial differential equation using finite element analysis is the descretization of the computational domain.

2.4.2 Mesh Generation

The computational domain was discretized using triangular Lagrangian elements of second order (quadratic elements). Mesh distribution can be controlled by tuning different mesh parameters such as maximum element size, element growth rate, and mesh curvature factor. In a finite element analysis, a small mesh size is necessary for the regions of high velocity gradients, i.e. regions where large variation of velocity with respect to small distances occurs. Due to the presence of no slip boundary condition on the collector wall, the regions close to the collector surface has the highest velocity gradients. By adjusting the maximum element size on the collector surface (OD) and defining the appropriate element growth rate, a non-uniform mesh structure is generated with high mesh density close to the collector surface where the higher values of velocity gradients occur. The non-uniform mesh configuration employed in the computational domain, OABCD, is shown in Figure 2.2. As can be seen in Figure 2.2, the regions close to the collector surface with the radius around R_{jet} has the highest mesh density compared to the other regions in the computational domain. This is the region where the fluid velocity changes from the stagnation flow patterns to the parallel flow patterns and hence has the highest velocity gradients. The maximum element size on the collector surface in the area with radius around R_{jet} is 0.5 μm. The element growth rate is 1.2. The solution of fluid velocity presented in this study is obtained with 35,000 total elements in the computational domain. The governing equations are solved using a stationary non-linear solver employing damped Newton method with initial and minimum damping factors set to 1 and 10^{-4}. The relative tolerance is assumed to be 10^{-6}. Once the relative error is less than the relative tolerance the software stops iterating and the solution is complete. The maximum number of

iteration is set to 25.

The dependence of the numerically obtained values of velocity on number of elements is verified for different values of flow Reynolds number, Re, ranging from 50 to 200, which correspond to the average nozzle velocity, U_∞, from 0.05 m/s to 0.2 m/s. For each value of Re, the simulation is repeated with different element numbers ranging from 20,000 to 63,000. It has been observed that the numerically obtained fluid velocity is not affected by changing the mesh density for element numbers larger than 30,000 within the defined range of Reynolds number. This ensures the mesh independence of the numerical results. In Table 2.2, the dependence of the dimensionless fluid velocity, $\bar{u}$ ($\bar{u} = \sqrt{\bar{u}_r^2 + \bar{u}_z^2}$) , on the number of elements has been shown for Re of 100. The fluid velocity corresponds to a point in the computational domain with the distances of $(\bar{r}, \bar{z}) = (100, 10)$ from the stagnation point. It can be seen in Table 2.2 that the value of fluid velocity became constant for element number greater than 30,000.

2.4.3 Validation of Numerical Results

Analytical expressions for the velocity field inside impinging jet flow system are available under some limiting conditions, such as, in the vicinity of the stagnation point. These analytical expressions can be employed to validate the accuracy of the present numerical results for fluid velocity.

Near the stagnation point, analytical expressions for the radial and normal components of the fluid velocity, u_r and u_z, respectively, take the following forms [Dabros and van de Ven, 1983, Masliyah, 1994]

$$u_r = \alpha_s r z \tag{2.6a}$$

$$u_z = -\alpha_s z^2 \tag{2.6b}$$

where α_s is a function dependent on the Reynolds number and the geometry of the system given by

$$\alpha_s = \frac{\bar{\alpha}\ \nu Re}{R_{jet}^3} \tag{2.7}$$

The term $\bar{\alpha}$ is a function characterizing the intensity of stagnation flow and dependent on the Reynolds number and flow geometry. For the case of $L/R_{jet} = 2$ that is used in the present study, we have [Adamczyk *et al.*, 1986, Masliyah, 1994]

$$\bar{\alpha} = 3.71 \qquad Re \leqslant 5.0 \tag{2.8a}$$

$$\bar{\alpha} = 5.3\sqrt{Re} - 8.13 \qquad Re > 5.0 \tag{2.8b}$$

where the Reynolds number for the stagnation flow geometry is defined as

$$Re = \frac{U_\infty R_{jet}}{\nu} \tag{2.9}$$

where ν is the kinematic viscosity of the fluid.

Figure 2.3 depicts a comparison between the velocity fields obtained using the analytical expression, Eq. (2.6), and using the numerical solution of the Navier-Stokes equations, Eq. (2.3). This figure shows the variation of radial and normal components of the fluid velocity in the impinging jet flow region with radial position, r, at a fixed vertical distance from the collector surface, z. This figure was obtained for a Reynolds number of 100 ($U_\infty = 0.1 m/s$).

From Figure 2.3, it is evident that the analytical expressions for fluid velocity are in accordance with the numerical solutions of the Navier-Stokes equations in the vicinity of the stagnation point region ($r/R_{jet} < 0.15$). This comparison ensures the accuracy of the numerical results in the stagnation region.

In the regions further away from the stagnation point, the difference between the numerical solutions of Navier-Stokes equation, Eq. (2.3), and analytical expression for fluid velocity, Eq. (2.6), is significant. In the regions far from stagnation point, the present finite element based velocity profiles are in excellent agreement with the results of Yang et al. [Yang *et al.*, 1999], who employed a finite difference technique to calculate fluid velocity inside the impinging jet system.

The comparison between the velocity fields obtained using the analytical expression and using the numerical solution of the Navier-Stokes equations can be also employed to define the domain where the stagnation flow pattern prevails.

It was observed that the analytical expressions for flow velocity can be used to characterize the fluid velocity around stagnation point where $r/R_{jet} < 0.15$ and $z/R_{jet} < 0.1$. This is the domain within the impinging jet geometry that is referred to as stagnation point region from this point on in the present study.

2.5 Numerical Simulation Results

The fluid velocity inside the impinging jet geometry was obtained numerically by solving Navier-Stokes equations along with appropriate boundary conditions as was described in detail in Section 2.4. A good depiction of flow inside impinging jet geometry can be provided by a display of streamlines as shown in Figure 2.4. These results are obtained for Re=100 which corresponds to an average flow velocity of $U_\infty = 0.1$ m/s. The nozzle is at the upper left-hand corner with the main flow moving from left to right. It is worth noting here that according to Polat [Polat, 1991], the impinging jet flow will remain laminar up to the Reynolds number of 1500, which is well beyond the range of Reynolds number used in this study.

The radial and normal fluid velocity distributions over the impinging jet geometry are depicted in Figure 2.5 and Figure 2.6, respectively. Similar flow patterns were obtained numerically by Yang et al. and Dabros and van de Ven [Yang *et al.*, 1998, Dabros and van de Ven, 1983].

The corresponding radial and normal fluid velocity components, $\bar{u}_r$ and $\bar{u}_z$ are depicted in Figure 2.7 and Figure 2.8, respectively. These figures show the variation of velocity components with respect to r at three different vertical distances from the collector surface i.e., z=1, 10, 100 μm. It can be seen from these figures that by increasing the radial distance from the stagnation point, the radial component of fluid velocity increases whereas the normal component of fluid velocity decreases.

The relative variation of radial velocity to normal velocity with respect to r can be better seen in Figure 2.9. This figure shows the dependency of the ratio

of radial to normal fluid velocity, $\bar{u}_r/\bar{u}_z$, on radial distance from the stagnation point, r, for Re=100. According to this figure, for the regions with radius less than 150 μm ($r/R_{jet} < 0.15$) which represents the stagnation point region, the normal fluid velocity is greater than the radial fluid velocity, ($u_r/u_z < 1$). In contrast, in the regions further away from the stagnation point ($r/R_{jet} > 0.15$), the radial fluid velocity is greater than the normal fluid velocity, , ($u_r/u_z > 1$). This implies that the flow distribution in impinging jet geometry can be characterized by the dominant role of normal fluid velocity near the stagnation point ($r/R_{jet} > 0.15$) and a dominant role of tangential (radial) fluid velocity at radial distances further away from the stagnation point. Hence, studying particle motion and particle deposition over a collector in such a flow regime at different distances from the stagnation point will provide a better understanding of the role of hydrodynamic effects in defining the fate of the particles in the vicinity of the collector surface.

2.6 Summary

The fluid velocity in impinging jet flow system has been computed by solving the governing Navier-Stokes equations numerically using finite element analysis employing FEMLAB® software. In order to validate the numerical method, the numerically obtained values of fluid velocity were compared with those obtained by analytical expressions restricted to the stagnation point region. A good agreement between the analytically obtained velocity and numerically obtained velocity has been observed that ensures the accuracy of the numerical procedure. The solution of fluid velocity near and far from the stagnation point demonstrate two different flow patterns. In the vicinity of the stagnation point, the normal component of fluid velocity is dominant whereas far from the stagnation point, the radial component of fluid velocity plays the dominant role. Studying particle motion in these two different flow regimes provides a better insight into the role of hydrodynamic effect on particle motion. The fluid velocity field obtained

here will be incorporated in the trajectory analysis and the convection-diffusion-migration equation, which will be discussed in following chapters.

Table 2.1: Dimensions of the Radial Impinging Jet System Used in the Simulations

Property	**Value (mm)**
Vertical distance between the collector and the jet tip, L or OA	2
Jet radius, R_{jet} or AB	1
Exit plane along the jet wall, BC	3
Outflow plane, DC	2
Collector surface, OD	4

Table 2.2: Dependence of Numerically Obtained Fluid Velocity on the Number of Elements

Number of Elements	**Fluid Velocity,** $\bar{u} = \sqrt{\bar{u}_r^2 + \bar{u}_z^2})$
22,144	0.0273
28,977	0.0274
31,346	0.0385
35,698	0.0386
47,930	0.0386
63,824	0.0386

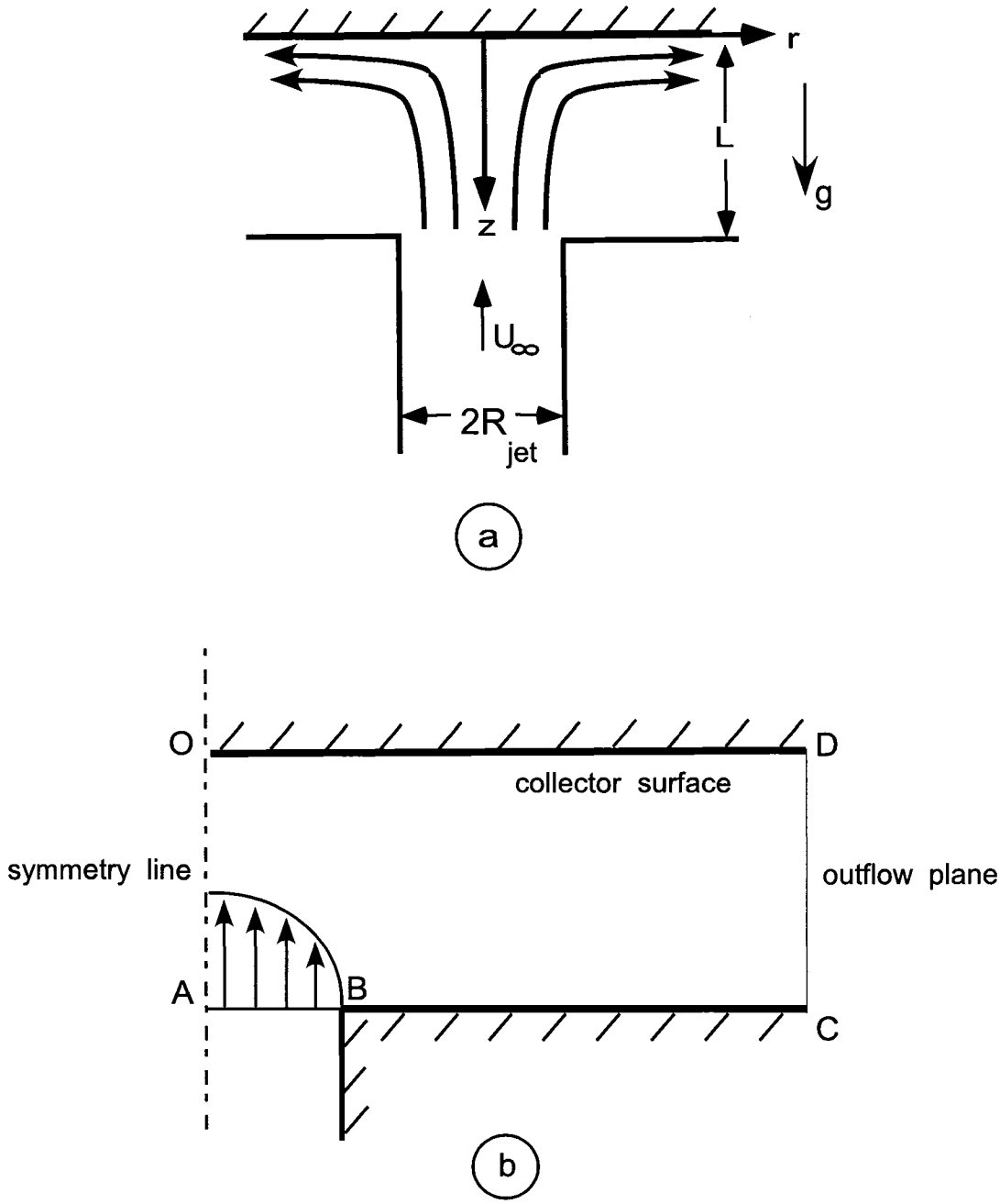

Figure 2.1: (a) A schematic representations of fluid streamlines and coordinate system of an impinging jet flow field. (b) Computation domain considered for numerically solving of Navier-Stokes equations, Eq. (2.3). In this figure, OA is the axis of symmetry and O is the origin of the cylindrical coordinate system. AB is the exit of the jet nozzle, OD is the collector surface, BC is the exit plane along the jet wall and DC is the outflow.

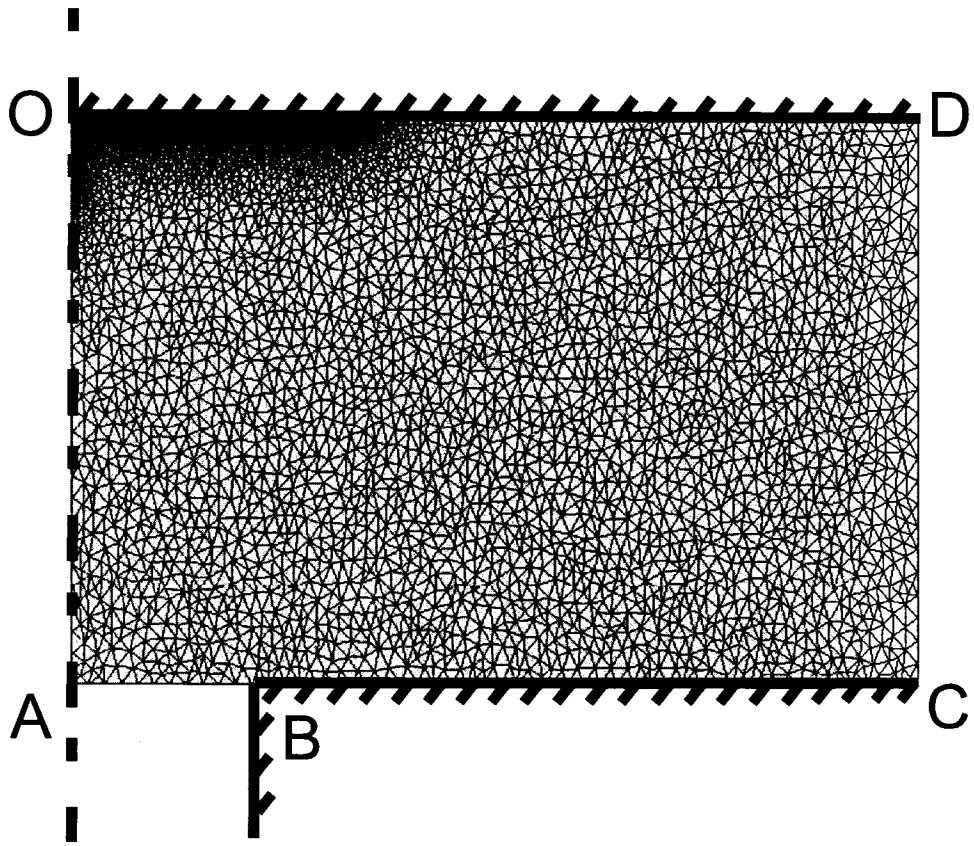

Figure 2.2: A schematic representation of the mesh configuration in the computational domain in the impinging jet geometry.

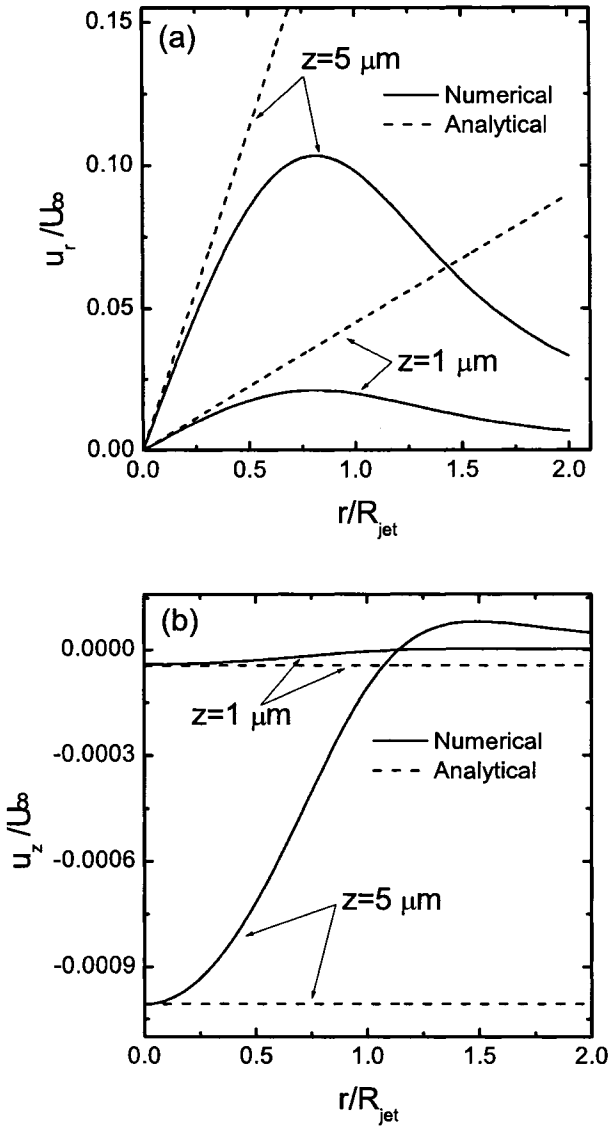

Figure 2.3: Variation of scaled (a) Radial and (b) Normal components of the fluid velocity with radial distance (r) at two different vertical distances from the substrate (i.e., z=1 μm and z=5 μm). The corresponding Reynolds number is 100. Solid lines denote the numerically calculated fluid velocity using Eq. (2.3). Dashed lines denote the analytically calculated fluid velocity using Eq. (2.6).

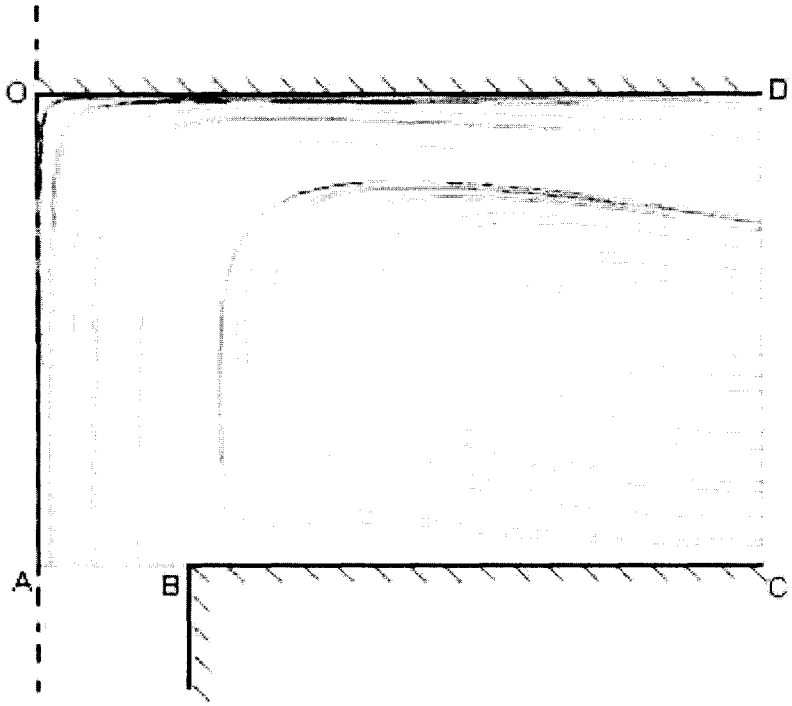

Figure 2.4: Velocity field streamlines inside the impinging jet flow system. These streamlines correspond to *Re* of 100. The nozzle is at the upper left-hand corner (AB), with the main flow moving from left to right. Hatched lines represent the collector surface (OD), nozzle wall and exit plane along the jet wall (BC).

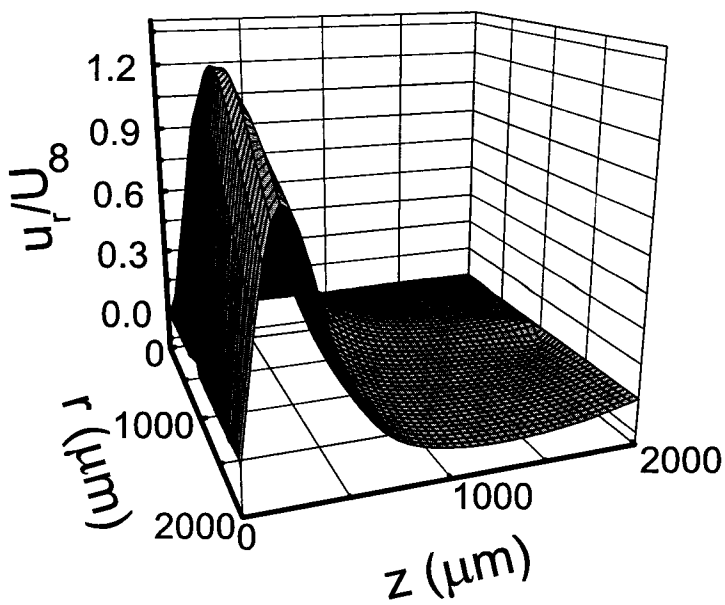

Figure 2.5: The radial fluid velocity distributions inside the impinging jet flow geometry. These results correspond to Re=100.

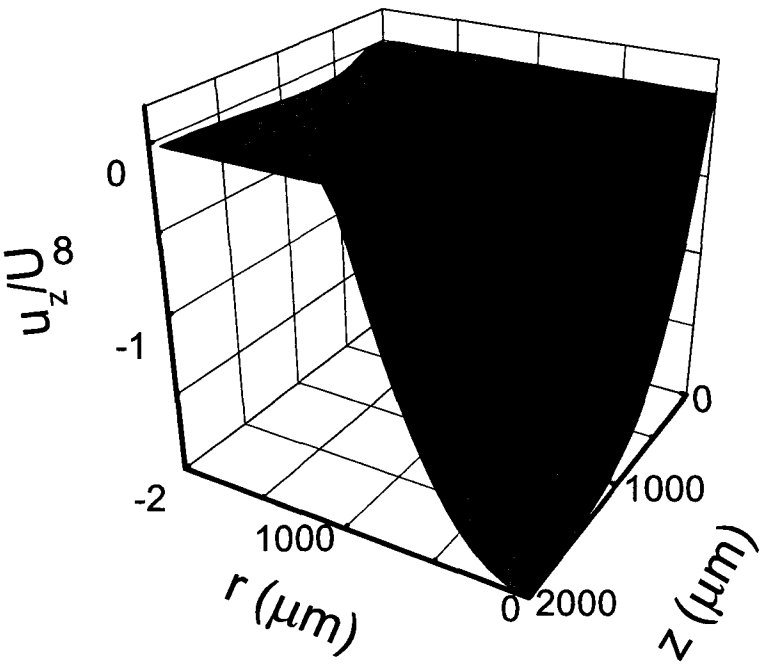

Figure 2.6: The normal fluid velocity distributions inside the impinging jet flow geometry. These results correspond to Re=100.

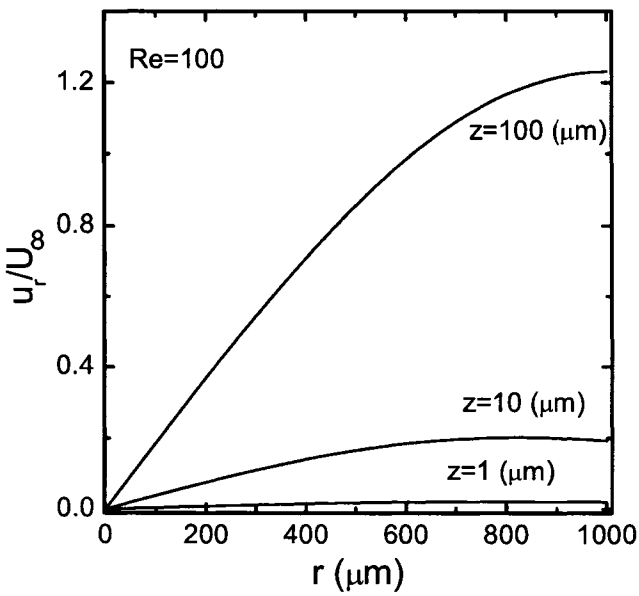

Figure 2.7: Variation of scaled radial component of the fluid velocity with radial distance (r) for three different vertical distances from the substrate (i.e., z=1 μm, z=10 μm and z=100 μm).

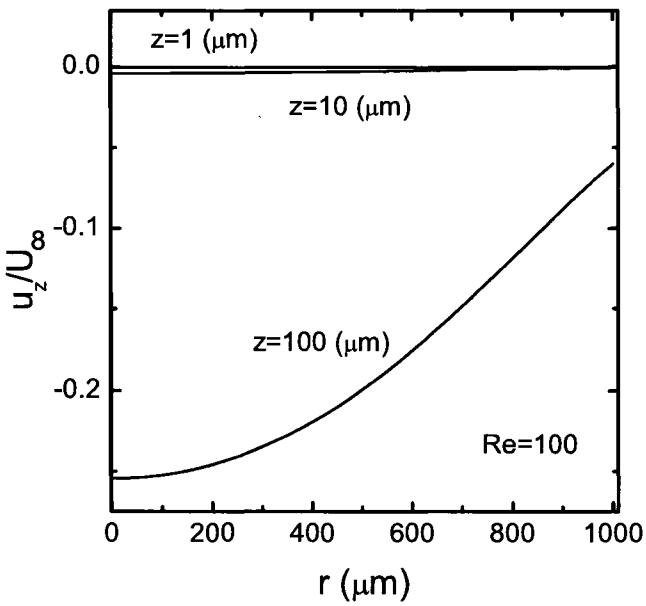

Figure 2.8: Variation of scaled normal component of the fluid velocity with radial distance (r) for three different vertical distances from the substrate (i.e., z=1 μm, z=10 μm and z=100 μm).

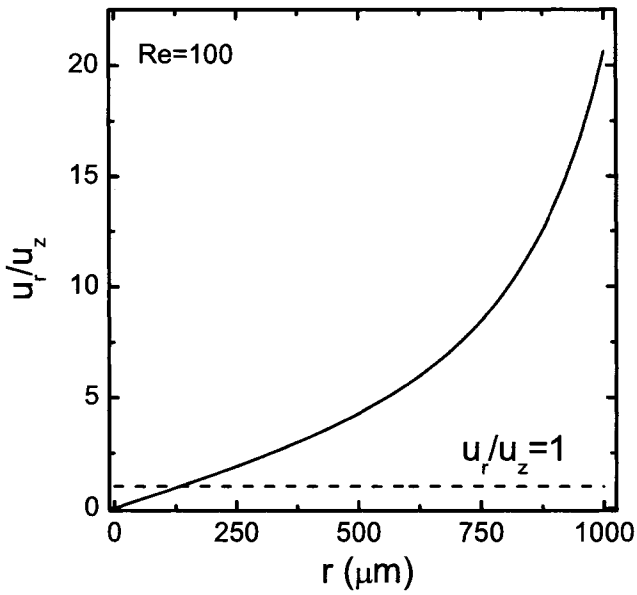

Figure 2.9: Dependence of the ratio of radial to normal fluid velocity, $\bar{u}_r/\bar{u}_z$, on radial distance, r, at z=100 μm. The corresponding Re=100.

Chapter 3

External Forces

3.1 Introduction

In this chapter, we will focus on defining the external forces that are exerted on particles during their motion inside the impinging jet system in the vicinity of the collector surface. These external forces can be divided into two categories; external body forces, and external surface forces. Generally, the external body forces acting on the particle may include gravitational force and electrical force. Due to the absence of any external electric field in the present study, gravitational force is considered as the only body force that the particles inside the impinging jet system are subjected to. The surface forces acting on the charged particles suspended in a fluid consist of hydrodynamic drag force and colloidal interactions between the particles themselves and the particle and the collector surface. In this study, it is assumed that the bulk particle concentration is sufficiently low such that particle-particle interactions can be neglected. Additionally, a description of the modelling of surface charge heterogeneity of the collector will be provided to facilitate the understanding of the colloidal interactions between the particles and the charge heterogeneous substrate. The operating and physicochemical properties of the modelled system which are required to calculate the external forces used in this work are listed in Table 3.1.

3.2 Gravity Force

For the particles suspended in a liquid in the absence of external electric field, the gravity and buoyancy forces can be considered as the only body forces acting on the particles. The net gravity and buoyancy force can be expressed as

$$\vec{F}_g = \frac{4}{3}\pi a_p^3 \Delta\rho \vec{g} \tag{3.1}$$

where $\Delta\rho$ is the difference between the particle and fluid densities. For solid particles that have greater densities than that of the liquid, $\Delta\rho$ is a positive number. Considering the geometry of the impinging jet system depicted in Figure 2.1a, it can be deduced that the net gravity force, Eq. (3.1), just has one component in normal, z, direction. For positive values of $\Delta\rho$, this normal component is also positive indicating that the net gravity force acts unfavorably to the attachment of the particles to the collector surface.

The gravity force can be nondimesionalized with respect to Brownian force ($F_{Br} = k_b T/a_p$) which results in

$$\bar{F}_g = \frac{F_g}{k_b T/a_p} = \frac{4\pi}{3}\frac{\Delta\rho g\ a_p^4}{k_b T} \tag{3.2}$$

where $\bar{F}_g$ is called gravity number. Here, k_b is the Boltzmann constant and T is the absolute temperature.

3.3 Hydrodynamic Drag Force

In general, a solid body moving through a viscous fluid will experience a frictional resistance or hydrodynamic drag force. The drag force on a moving body is dependent on a number of physical variables such as the size, the shape and the translational speed of the body. It is also dependent upon the properties of the fluid, such as its viscosity and density. For low Reynolds number flows, the drag force on a smooth spherical particle is given by Stokes equation as

$$\vec{F}_{Hyd} = 6\pi\mu_f a_p \vec{v} \tag{3.3}$$

where $\vec{v}$ is the hydrodynamic particle velocity induced by fluid motion. In the axisymmetric cylindrical coordinate system, the particle velocity vector has components v_r and v_z along the radial and axial directions, respectively. In the absence of a solid wall near the particle, the value of hydrodynamic particle velocity is considered to be equal to the fluid velocity. However, in the vicinity of a solid surface, the velocity of the particle induced by fluid motion is different from that of the fluid due to the effect of hydrodynamic interactions between the particle and the solid wall. In the impinging jet flow system, the fluid velocity has radial and normal components u_r and u_z, as defined in Chapter 2. Following Spielman and Fitzpatrick [Spielman and Fitzpatrick, 1973], the relationship between the fluid and particle velocities in such a flow system is given by

$$v_r = f_3(h)u_r \tag{3.4a}$$

$$v_z = f_1(h)f_2(h)u_z \tag{3.4b}$$

Here, h is the dimensionless surface to surface distance between the particle and the substrate, ($h = s/a_p$ where s is the separation distance between the particle and the substrate). $f_1(h)$ to $f_3(h)$ are the universal hydrodynamic correction functions that account for the deviation from the Stokes drag formula due to the presence of the collector wall. They have been extensively studied in low Reynolds number flow mechanisms [Brenner, 1961, Goren, 1970, Goren and Oneill, 1971, Goldman *et al.*, 1967*b*, Goldman *et al.*, 1967*a*]. The values of these functions were tabulated in literature. In order to incorporate their values directly into our simulations, it is advantageous to curve fit each of these functions so that they could be expressed as empirical functions. The results of this curve fitting are provided by Masliyah [Masliyah, 1994] as follows

$$f_1 = 1 - 0.399exp\ (-0.14869\ h) - 0.6010exp\ (-1.2015\ h^{0.92667}) \tag{3.5a}$$

$$f_2 = 1 - 1.362exp\ (-1.3596\ h) + 0.8764exp\ (-0.5250\ h^{0.56954}) \tag{3.5b}$$

$$f_3 = 1 - 0.3752exp\ (-3.906\ h) - 0.625exp\ (-3.105\ h^{0.150}) \tag{3.5c}$$

$$f_4 = 1 - 1.23122exp\ (-0.2734\ h) + 0.8189exp\ (-0.1750\ h^{1.2643}) \qquad (3.5d)$$

The variation of the universal hydrodynamic correction functions with respect to the dimensionless separation distance between the particle and the collector surface, h, is shown in Figure 3.2.

Incorporating the relation between the particle and fluid velocity in Eq. (3.3), the hydrodynamic drag force acting on the particle inside the impinging jet flow system can be formulated as

$$F_{Hyd,\ r} = (6\pi\mu_f a_p)u_r f_3(h) \qquad (3.6a)$$

$$F_{Hyd,\ z} = (6\pi\mu_f a_p)u_z f_1(h) f_2(h) \qquad (3.6b)$$

where $F_{Hyd,\ r}$ and $F_{Hyd,\ z}$ are the radial and normal components of the drag force acting on the particle due to the fluid velocity. The above set of equations can be nondimesionalized with respect to Brownian force i.e., k_bT/a_p which takes the following form

$$\bar{F}_{Hyd,\ r} = \frac{a_p}{D_\infty} u_r f_3(h) \qquad (3.7a)$$

$$\bar{F}_{Hyd,\ z} = \frac{a_p}{D_\infty} u_z f_1(h) f_2(h) \qquad (3.7b)$$

where D_∞ is the particle diffusion coefficient in bulk medium given by Stokes-Einstein equation ($D_\infty = 6\pi\mu_f a_p/k_bT$). The fluid velocity components u_r and u_z were obtained from the numerical solution of the Navier-Stokes and continuity equations as discussed in Chapter 2.

3.4 Colloidal Interactions

When the particles approach to the collector surface within a separation distance of around 0.1 μm, the particle motion is affected by colloidal interactions between the particle and collector surface. The Derjaguin-Landau-Verwey-Overbeek (DLVO) force, consisting of an attractive van der Waals interaction and an electrostatic double layer contribution, represents the total colloidal force exerted on a mobile particle by the substrate. These two types of colloidal forces

are widely recognized and well documented in the literature [Masliyah, 1994, Elimelech, 1995]. The particle-particle colloidal interaction is considered to be negligible by assuming a dilute particle suspension.

3.4.1 van der Waals Interactions

The dispersion attractive forces between molecules, known as van der Waals force, is present between macrobodies as well. These interactions play an important role in particle movement and attachment to the substrate. The origin of this attractive force between macroscopic bodies in small separation distances is the spontaneous electric and magnetic polarization occurring in molecules of both bodies. There are two well-known approaches in calculating the van der Waals interaction. One is Hamaker approach based on the assumption of pairwise additivity of all the intermolecular interactions. The second is the Lifshitz theory based on quantum electrodynamics, which provides a more rigorous expression for van der Waals interaction [Israelachvili, 1985].

In the present study, an expression for the non-retarded van der Waals force between a sphere and an infinite planar surface based on Hamaker's approach and Derjaguin's approximation is used [Suzuki *et al.*, 1969]

$$F_{vdw} = -\frac{A}{6a_p}\frac{1}{h^2} \tag{3.8}$$

where A is the Hamaker constant between the particle and collector surface in the liquid medium and h is the dimensionless surface to surface separation distance between the particle and the collector surface as is shown in Figure 3.1.

The van der Waals force between the particle and the collector surface acts along the normal direction to the collector surface. This means that van der Waals force is comprised of just one component in normal, z, direction. The expression for van der Waals interaction can be nondimensionalized with respect to Brownian force as

$$\bar{F}_{vdw} = \frac{F_{vdw}}{k_b T/a_p} = -Ad\frac{1}{h^2} \tag{3.9}$$

where $Ad = A/6k_bT$, is the adhesion number and indicates the strength of van der Waals interaction. In the present study, the Hamaker constant between the spherical particles and the collector surface inside the aqueous solution is considered to be a positive number. This means that van der Waals interaction between the particle and the collector surface in this case is attractive in nature and acts favorably in particle deposition process.

3.4.2 EDL Interactions in the Presence of Charge Heterogeneity

In addition to van der Waals interaction force, there is another type of colloidal interaction between the particle and the collector surface. It has been long known that interfaces in the aqueous environment acquire surface charge due to different reasons such as the ionization of surface group, different affinity of the surface towards some ions, and physical restriction of certain ions to one phase. Whatever the origin of the surface charge is, due to the electro-neutrality of the whole system, the surface charge should be exactly balanced by an equal and opposite charge in solution. This balancing charge is accounted for by an excess number of oppositely charged ions or *counter-ions* in the solution adjacent to the charged surface and a deficit of similarly charged ions or *co-ions*. The overall arrangement of the electrostatic charge on the surface together with the redistribution of the ions around the charged surface is referred to as electrostatic double layer (EDL) [Hunter, 1981]. One of the accepted model for EDL is Stern model. According to this model, due to electrostatic attraction, some immobile counter-ions are located adjacent to the surface and form the Stern layer. Outside the Stern layer, the mobile counter-ions are distributed such that the motion of these ions is balanced by both electrostatic attraction and the diffusion due to thermal effects. This layer is called diffuse layer. When two charged surfaces approach each other in an electrolyte solution, their diffuse double layers overlap, resulting in the electrostatic double layer (EDL) interaction. Assuming constant surface potential on the particles and the planar

substrate [Adamczyk, 1989] and a symmetric (z:z) electrolyte solution, the well-known Hogg, Healy, and Fuerstenau (HHF) expression [Hogg *et al.*, 1966] for the electrostatic double layer interaction force for the case of constant surface potential is used in the simulations which has the form of

$$F_{edl} = 4\pi\epsilon_0\epsilon(\kappa a_p)\left(\frac{k_bT}{ze}\right)^2 \Psi_p\Psi_s\left[\frac{exp(-\kappa a_p h)}{1-exp(\kappa a_p h)} - \frac{(\Psi_p-\Psi_s)^2}{2\Psi_p\Psi_s}\frac{exp(-2\kappa a_p h)}{1-exp(2\kappa a_p h)}\right] \tag{3.10}$$

Here, Ψ_p and Ψ_s are the scaled surface potentials ($\Psi = ze\psi/k_bT$) of the particle and the substrate, respectively, and κ is the inverse Debye length, given by [Hunter, 1981]

$$\kappa = \sqrt{\frac{2n_\infty z^2e^2}{\epsilon_0\epsilon k_bT}} \tag{3.11}$$

where n_∞ is the bulk ionic number concentration of the electrolyte, ϵ is the solvent dielectric constant, ϵ_0 is the dielectric permittivity of vacuum, k_b is Boltzmann constant and T is the absolute temperature. The above equation can be nondimensionalized with respect to Brownian force as

$$\bar{F}_{edl} = \frac{F_{edl}}{k_bT/a_p} = Dl(\kappa a_p)\left[\frac{exp(-\kappa a_p h)}{1-exp(\kappa a_p h)} - Da\frac{exp(-2\kappa a_p h)}{1-exp(2\kappa a_p h)}\right] \tag{3.12}$$

where Dl is the electrostatic double layer parameter indicating the strength of electrostatic double layer interaction defined as

$$Dl = \frac{4\pi\epsilon_0\epsilon a_p k_bT\Psi_p\Psi_s}{z^2e^2} \tag{3.13}$$

and Da is the double layer asymmetry parameter accounting for the portion of double layer force arising due to the difference between the particle and collector surface potentials.

$$Da = \frac{(\Psi_p-\Psi_s)^2}{2\Psi_p\Psi_s} \tag{3.14}$$

According to the above definition, for $\Psi_p = \Psi_s$, Da is equal to zero.

The Hogg, Healy, and Fuerstenau (HHF) expression, Eq. (3.12), provides the electrostatic double layer interaction between a spherical particle with surface potential of Ψ_p and an infinite planar surface with surface potential of Ψ_s.

The direction of this force is normal to the substrate surface which by considering the geometry of the impinging jet system implies that the EDL force is comprised of just one component in vertical (normal) direction. This equation can be assumed to estimate accurately the electrostatic double layer interaction between a particle and a homogeneous collector. For the case of heterogeneous collector, the electrostatic double layer interaction between the particle and the collector depends on how the surface charge heterogeneity is modelled on the collector surface. Therefore, a full description of modelling charge heterogeneity on the collector surface in the present study is required first.

The collector surface charge heterogeneity is modelled as alternate stripes or bands of microscopic dimensions bearing positive and negative charges as is shown in Figure 3.3. In a radial impinging jet flow context, such stripes can be construed as concentric circular rings bearing different surface potentials. Each negative and positive band has a specific width which is defined as w_n and w_p, respectively. Since the particles are assumed to be negatively charged throughout this study, the negatively charged band acts as a unfavorable region and positively charged band acts as a favorable region with respect to deposition. The total width of a pair of consecutive negative and positive band is defined as pitch, p.

The ratio of positive band width (w_p) to the total width of a positive and a negative band (p) specifies the fraction of the collector surface area that is covered with favorable charge. This is called favorable area fraction of the collector and is shown by $\lambda_{patterned} = s_f/s_{total}$ where s_f represents the area of the collector that is favorably charged and s_{total} represent the total area of the collector surface. $\lambda_{patterned}$ is approximately equal to w_p/p far away from the stagnation point and we can relate p to w_p as

$$\lambda_{patterned} = \frac{w_p}{p} \tag{3.15}$$

In order to specify each unfavorable and favorable band along the radial direction on the collector surface, a number defined as band number, N_b, is assigned to each pair of consecutive favorable and unfavorable bands on the

collector surface such that for the first pair of unfavorable and favorable band $N_b = 1$, for the second pair of unfavorable and favorable band $N_b = 2$ and so forth (Figure 3.3b). It is worth noting here that in this study, for a heterogeneous collector consisting of alternate negative and positive band, the first circular (innermost) band at the stagnation point is always negatively charged and therefore is unfavorable with respect to deposition.

The EDL force acting on a particle over a heterogeneous collector consisting of alternate negative and positive bands is modelled assuming that when the particle center passes over a positive band, the electrostatic interaction is solely that between the negatively charged particle and an infinite planar surface bearing a positive surface potential. Similarly, as long as the particle is directly facing a negative band on the surface, the electrostatic interaction is calculated assuming the entire collector surface to have a negative surface potential. This assumption is clearly a gross simplification of the actual electrostatic double layer interaction between a charge heterogeneous substrate and the particle. However, as long as the individual band width is larger than the particle size, the particle is sufficiently close to the substrate, and the electrostatic double layer interactions are sufficiently screened (large κa_p), use of the above approximation is expected to provide reasonably accurate estimates of the electrostatic double layer interactions and the particle trajectories. This implies that the expression for EDL force, Eq. (3.12), will provide a periodically attractive and repulsive force profile as the particle traverses the substrate radially. The nature of this periodic behaviour is dictated by the shape of Ψ_s imposed inside the expression for EDL interaction, Eq. (3.12).

The variation of Ψ_s with r for a heterogeneous collector consisting of negative and positive band was initially considered to have a periodic behavior of stepwise nature which is

$$\Psi_s = \Psi_{s_n} \qquad (N_b - 1)p < r \leqslant (N_b - 1)p + w_n \tag{3.16a}$$

$$\Psi_s = \Psi_{s_p} \qquad (N_b - 1)p + w_n < r < N_b p \tag{3.16b}$$

where Ψ_{s_n} and Ψ_{s_p} are collector surface potentials corresponding to negative and positive bands, respectively. This equation implies that the collector surface potential changes instantaneously from Ψ_{s_n} to Ψ_{s_p} at the boundary between the unfavorable and favorable band as is shown in Figure 3.4a. This figure shows the variation of collector surface potential, Ψ_s, represented by a step function such as Eq. (3.16), for a collector consisting of alternate negative and positive bands with surface potentials of $\Psi_{s_n} = -1$ and $\Psi_{s_p} = +1$, respectively. The width of negative and positive bands are equal and assumed to be $w_n = w_p = 10\ \mu m$. The resulting EDL force between a particle with such a collector is depicted in Figure 3.4b. These results were obtained for a negatively charged particle with scaled surface potential of -1 using Eq. (3.12) at the distance of h around 0.001. In this figure, r represents the radial distance of the particle center from the stagnation point.

It can be seen from Figure 3.4a that using the stepwise function for simulating the collector surface potential behaviour seems a rough estimation of the real function for the variation of surface potential along the heterogeneous collector. In reality, at the boundary between the negative and positive bands, the surface potential changes smoothly from its value over the negative band, Ψ_{s_n}, to its value over the positive band, Ψ_{s_p} while taking the value of zero at the boundary between the differently charged bands. Therefore, in order to capture this behaviour, a smoothing function of sigmoidal nature is incorporated in Eq. (3.16) to smooth the changes of Ψ_s in the vicinity of the boundaries between the differently charged bands. The parameters of this smoothing function are defined such that it ensures the value of zero for Ψ_s at the boundary of a negative and positive stripe. The results of incorporating this smoothing function are shown in Figure 3.5a. This figure shows the variation of Ψ_s with r, obtained by incorporating the smoothing function inside Eq. (3.16). All the parameters are the same as those of Figure 3.4. The resulting EDL force between a particle and a collector with such a surface potential is depicted in Figure 3.5b. Using the smoothing functions for Ψ_s provides a better estimation of the EDL force

between a particle and a heterogeneous collector consisting of alternate negative and positive bands compared to the stepwise variation of Ψ_s. However, the particle trajectories and particle deposition behaviour over the heterogeneous collector obtained using these two different approximations for EDL force are not significantly different.

3.5 Summary

In this chapter, all of the external forces that affect the motion of a spherical charged particle inside the impinging jet system in the vicinity of a collector surface were studied. It was deduced that in the radial direction, the tangential component of hydrodynamic drag is the only external force acting on the particle whereas in normal direction, gravity, van der Waals, electrostatic double layer, and vertical component of hydrodynamic drag were simultaneously exerted on the particle. The total forces acting on the particle in radial and normal directions can be given as

$$\bar{F}_r = \bar{F}_{Hyd,\,r} = \frac{a_p}{D_\infty} u_r f_3(h) \tag{3.17a}$$

$$\begin{aligned} \bar{F}_z &= \bar{F}_g + \bar{F}_{Hyd,\,z} + \bar{F}_{vdw} + \bar{F}_{edl} \\ &= \left[\frac{4\pi}{3}\frac{\Delta\rho g\, a_p^4}{k_b T}\right] + \left[\frac{a_p}{D_\infty} u_z f_1(h) f_2(h)\right] + \left[-Ad\frac{1}{h^2}\right] + \\ &\quad \left[Dl(\kappa a_p)\left[\frac{exp\,(-\kappa a_p h)}{1 - exp\,(\kappa a_p h)} - Da\frac{exp\,(-2\kappa a_p h)}{1 - exp\,(2\kappa a_p h)}\right]\right] \end{aligned} \tag{3.17b}$$

where the expressions for the righthand side of the above equations were provided earlier in this chapter.

The modelling of charge heterogeneity and the calculation of colloidal forces between the particles and a heterogeneous substrate were discussed in detail as well. The expressions for the external forces defined in this chapter will be utilized in trajectory analysis and convection-diffusion-migration model in the following chapters.

Table 3.1: Physical and Chemical Properties of the System Used in Simulations

Property	**Value**
Particle radius, a_p	0.1-2 μm
Particle density, ρ_p	2300 kg/m^3
Fluid density, ρ_f	1000 kg/m^3
Fluid viscosity, μ_f	1.0×10^{-3} N.s/m^2
Fluid inlet velocity, U_∞	0.05-0.2 m/s
Gravitational acceleration, g	9.81 m/s^2
Reynolds number, Re	50-200
Temperature, T	298 K
Boltzmann constant, k_b	1.38×10^{-23} J/K
Electronic charge, e	1.6×10^{-19} C
Permittivity of vacuum, ϵ_0	8.85×10^{-12} C/Vm
Dielectric constant, ϵ	78.54
Number of ions in the solution, n_∞	1×10^{-3}
Scaled particle surface potential, Ψ_p	-1, -2
Scaled collector surface potential, Ψ_s	-1, -2, +1, +2
Solution ionic strength, I	10^{-3}, $10^{-3.5}$ M
Hamaker constant, A	10^{-20} J
Pitch, p	4-20 μm
valence of ion, z	1

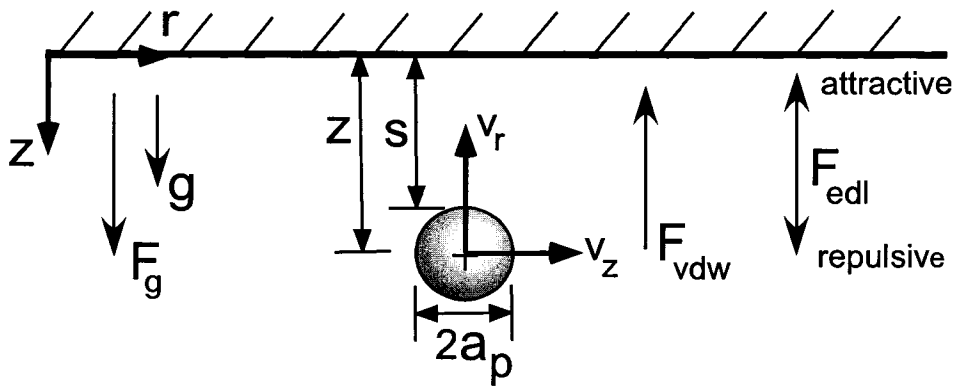

Figure 3.1: A schematic representation of the position of a colloidal particle with respect to the collector surface. a_p is the particle radius, z is the normal distance of the particle center from the collector surface, s is the normal surface to surface distance between the particle and the collector surface and h is the dimensionless separation distance between the particle and the collector surface ($h = s/a_p$).

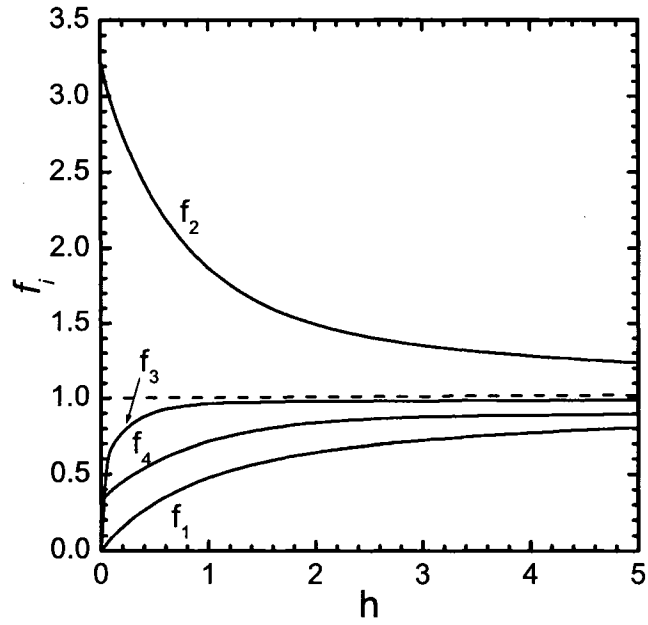

Figure 3.2: Variation of universal hydrodynamic correction functions with respect to dimensionless separation distance between a particle and the collector surface.

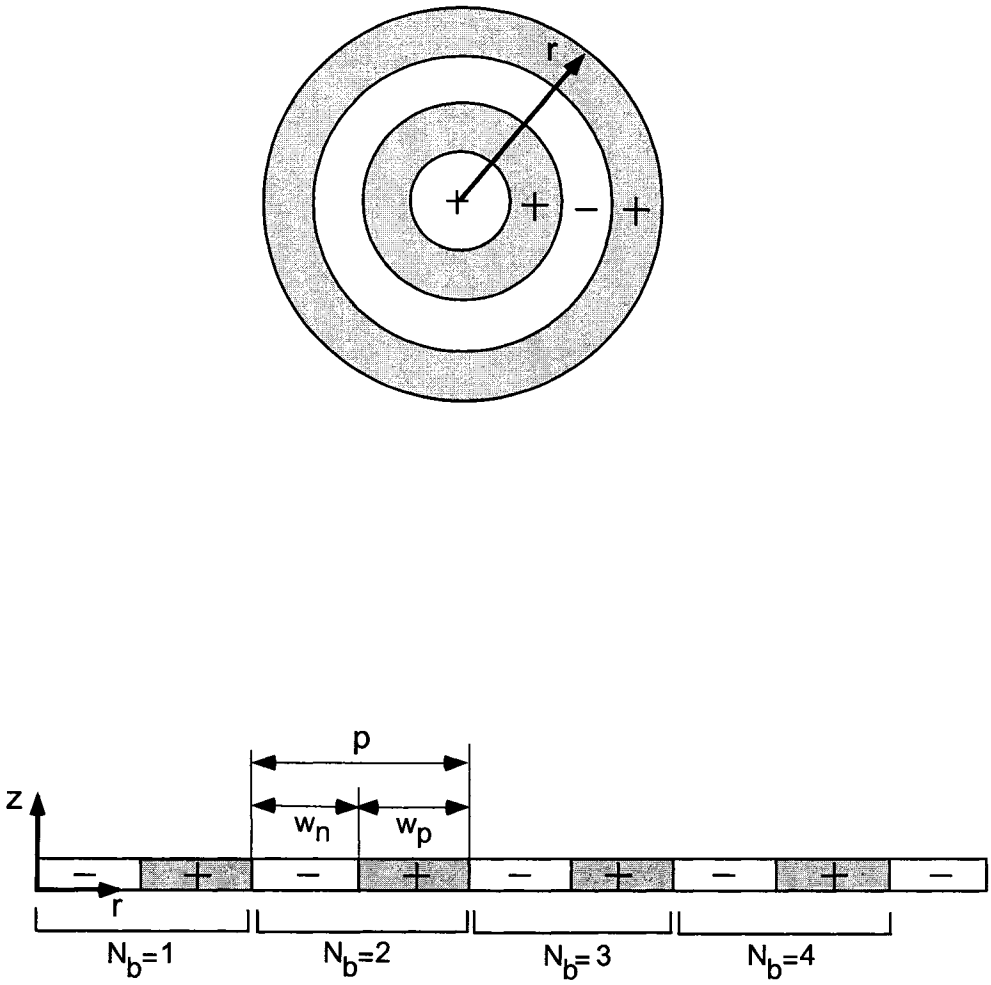

Figure 3.3: A schematic representation of the modelled surface charge heterogeneity. A collector surface consists of concentric circular bands with alternate negative and positive surface potentials with width of w_n and w_p, respectively. The total width of a negative and a positive band is pitch, p. N_b is a number assigned to each pair of negative and positive band along the radial direction on the collector surface.

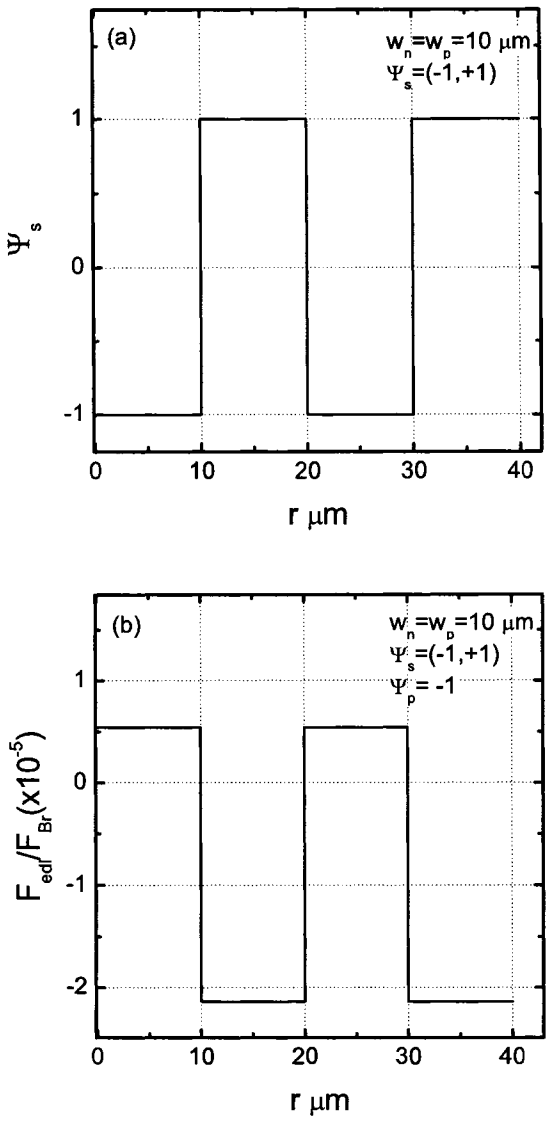

Figure 3.4: (a) Illustration of a step function employed to represent the variation of scaled collector surface potential with r for a heterogeneous collector with $\Psi_s = (-1, +1)$. (b) The resulting values of scaled F_{edl} between a negatively charged particle with $\Psi_p = -1$ and a heterogeneous collector with surface potential as shown in part (a). The values of $\bar{F}_{edl}$ were obtained using Eq. (3.12) for h=0.001, $a_p = 1$ μm.

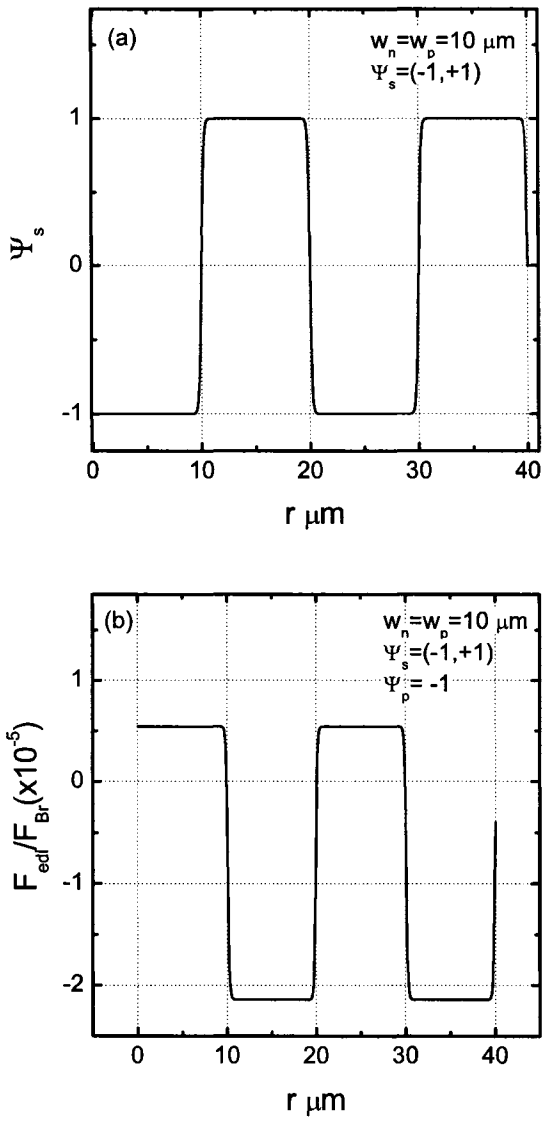

Figure 3.5: (a) Illustration of a smoothing sigmoidal function employed to represent the variation of scaled collector surface potential with r for a heterogeneous collector with $\Psi_s = (-1, +1)$. (b) The resulting values of scaled F_{edl} between a negatively charged particle with $\Psi_p = -1$, and a heterogeneous collector with surface potential as shown in part (a). The values of $\bar{F}_{edl}$ were obtained using Eq. (3.12) for h=0.001, $a_p = 1$ μm.

Chapter 4

Lagrangian Approach: Trajectory Analysis

4.1 Introduction

In this chapter, we use particle trajectory analysis to investigate the effect of microscopic surface charge heterogeneity on particle trajectories and particle deposition in form of collector deposition efficiency. The charge heterogeneity is modelled as alternate circular stripes or bands of microscopic dimensions bearing positive and negative charge as was described in Section 3.4.2. The flow distribution which is obtained using finite element analysis of the governing Navier-Stokes equations in Chapter 2, is incorporated in the trajectory equations. The particle trajectory analysis takes into consideration the hydrodynamic interactions, gravity, van der Waals and electrostatic double layer interactions. Solution of the trajectory equations provides particle trajectories over homogeneous as well as heterogeneous collectors with different surface potentials. From the limiting trajectories, the particle deposition rate, in form of collector deposition efficiency for both homogeneous and heterogeneous collectors can be obtained.

The available model that evaluates the particle deposition rate over heterogeneous collector is called patchwise heterogeneity model. A description of this model will also be provided in this chapter. Finally, the numerical re-

sults obtained for collector deposition efficiency using trajectory analysis will be compared with the values of collector deposition efficiency evaluated using the patchwise heterogeneity model.

4.2 Trajectory Model

In this section, we will develop a trajectory model to study the effect of charge heterogeneity of the collector on particle trajectory and particle deposition. The charge heterogeneity is modelled as alternate concentric circular bands with negative and positive potentials. A schematic representation of the expected trajectory of a negatively charged colloidal particle on such a charge heterogeneous substrate is depicted in Figure 4.1. When the colloidal particle migrates close to the planar substrate, it experiences attractive and repulsive colloidal forces as it traverses the positive and negative bands on the surface, respectively. This gives rise to an oscillatory motion of the particle, as depicted in Figure 4.1. It is our goal to show how such an oscillatory motion modifies the particle deposition efficiencies on charge heterogeneous surfaces.

The trajectory analysis is derived by applying Newton's second law of motion to a suspended particle in the fluid, given by

$$m\frac{d\vec{v}}{dt} = \sum_i \vec{F}_i \tag{4.1}$$

where m is the particle mass and $\vec{v}$ (v_r, v_z) is the particle velocity vector. The right hand side of Eq. (4.1) represents the sum of all the forces, $\vec{F}_i$, acting on the particle. In the present study, we consider gravity, fluid drag, van der Waals, and electrostatic double layer forces as the pertinent forces. These forces and their corresponding expressions were provided in Chapter 3.

Trajectory analysis is often used for the case when Brownian motion is negligible. The Brownian effects can be included in the trajectory analysis, the resulting mathematical analysis is complicated [Adamczyk, 1989, Elimelech, 1995, Masliyah, 1994]. Hence, the present analysis cannot be used for sub-micrometer

particles where Brownian motion contributes significantly to the particle trajectory. The radial and transverse hydrodynamic particle velocity components, (v_r, v_z) are related to the corresponding fluid velocity components u_r and u_z by Eq. (3.4), i.e., $v_r = f_3(h)u_r, v_z = f_1(h)f_2(h)u_z$.

A balance of forces acting in the radial and normal directions yields,
In r direction

$$6\pi\mu_f a_p \frac{dr}{dt} = f_3 F_r \tag{4.2}$$

where dr/dt represents the rate of radial displacement (v_r) of the particle. Here F_r is the sum of radial forces acting on the particle, which, as stated in Chapter 3, is only due to the radial component of the fluid drag

$$F_r = F_{Hyd,\ r} = 6\pi\mu_f a_p u_r \tag{4.3}$$

In z direction

$$6\pi\mu_f a_p \frac{ds}{dt} = f_1 F_z \tag{4.4}$$

where s is the surface to surface separation distance between the particle and the substrate which is shown in Figure 3.1.

$$s = z - a_p \tag{4.5}$$

and F_z is the sum of normal forces acting on the particle, which is comprised of the following terms

$$F_z = F_g + F_{Hyd,\ z} + F_{vdw} + F_{edl} \tag{4.6}$$

where different terms in right hand side of Eq. (4.6) represent gravity, normal component of hydrodynamic drag, van der Waals and electrostatic double layer force exerted on the particles in the impinging jet system.

Equations. (4.2) and (4.4) can be nondimensionalized by using the following scaled variables

$$h = \frac{s}{a_p} \qquad \bar{r} = \frac{r}{a_p} \qquad \bar{t} = \frac{tU_\infty}{L} \tag{4.7}$$

Introducing these variables inside the trajectory equations, Eqs. (4.2) and (4.4) take the following dimensionless forms

$$\frac{d\bar{r}}{d\bar{t}} = \frac{L}{a_p}\frac{1}{Pe} f_3 \bar{F}_r \tag{4.8a}$$

$$\frac{dh}{d\bar{t}} = \frac{L}{a_p}\frac{1}{Pe} f_1 \bar{F}_z \tag{4.8b}$$

where Pe is a dimensionless number representing the ratio of convective force to diffusive force and is defined as $Pe = U_\infty a_p / D_\infty$. $\bar{F}_r$ and $\bar{F}_z$ are total dimensionless radial and normal forces that exerted on the particles inside the impinging jet flow geometry and can be defined as

$$\bar{F}_r = \bar{F}_{Hyd,\ r} \tag{4.9a}$$

$$\bar{F}_z = \bar{F}_g + \bar{F}_{Hyd,\ z} + \bar{F}_{vdw} + \bar{F}_{edl} \tag{4.9b}$$

The expressions for right hand side of Eqs. (4.9)a and b have been provided in Chapter 3, Eq. (3.17). It is worth noting here that, since the term $f_1(h)$ is already incorporated inside the trajectory equations, Eq. (4.8)b, the expression for $\bar{F}_{Hyd,\ z}$ that was given by Eq. (3.7)b will be changed to $\bar{F}_{Hyd,\ z} = (a_p / D_\infty) f_2 u_z$.

Eq. (4.8) is the governing trajectory equation for the particle motion inside the impinging jet flow geometry under the defined external forces.

4.2.1 Numerical Simulation

Equations. (4.8) are coupled non-linear ordinary differential equations which can be solved numerically from a specified initial state. In this study, the solution methodology was developed using a standard ODE solver (ode45) from Matlab® (version 6.1, MathWorks Inc., USA), which is based on the optimized form of the Runge-Kutta method.

The numerically obtained velocity field (Chapter 2) was incorporated in the trajectory analysis using an interpolation scheme. Typically, the fluid velocity field obtained from the finite element solution of the Navier-Stokes equations

was represented as gridded data over the computational domain. Interpolation of the gridded data at each location of the particle provided the local velocity components. In order to capture the oscillatory movement of the particles near the charge heterogeneous substrate, and to obtain the trajectory accurately, non-dimensional time steps ($\bar{t}$) equal to 0.001 was used. The trajectory plots typically consist of approximately 100,000 points. The computation of each trajectory takes approximately 3 minutes on a personal computer.

The operating and physicochemical properties of the modelled system used in this work are listed in Table 3.1.

4.2.2 Collector Deposition Efficiency

In context of Lagrangian approach (trajectory analysis), the particle deposition is presented in form of collector deposition efficiency, η. Since the trajectory analysis is fully deterministic, it is fairly straightforward to obtain the deposition efficiency for a chemically uniform collector using the limiting trajectory [Elimelech, 1995, Masliyah, 1994]. Determination of the limiting trajectory directly leads to evaluation of the collector deposition efficiency by noting that the efficiency is the ratio of the flux of particles within the limiting trajectory to the total particle flux entering the flow volume over the projected area of the collector [Rajagopalan and Tien, 1976, Yao *et al.*, 1971].

Let us consider an arbitrary point on the collector surface with the radial distance of R_c from the stagnation point as is depicted in Figure 4.2. For completely favorable deposition, one can determine the limiting trajectory by initializing the integration of Eq. (4.8) at the surface of the collector corresponding to R_c, and following the trajectory upstream to the location where it emerges from the nozzle. Let us denote the radial position of this emergent limiting trajectory as $r_{0,\ lim}$. This implies that all of the particles located at the tip of the nozzle within a circle of radius $r_{0,\ lim}$ will deposit on the collector within a circular region of radius R_c. In practice, the numerical integration is initiated at a small separation distance from the collector surface. The sepa-

ration distance, δ_m, is usually taken as an arbitrary cut-off separation distance located typically around 1-5 nm from the collector surface [Yang *et al.*, 1998, Elimelech, 1995]. Use of this finite value for the separation distance eliminates the problems due to the divergence of van der Waals forces at contact. We can now use the results of the above limiting trajectory analysis to define a single collector efficiency. The projected area of the collector surface is a circular cross-section of radius R_c. Assuming the velocity at the nozzle to be U_∞ and the particle concentration to be c_∞, we can define the collector efficiency as

$$\eta = \frac{(\pi r_{0,\,lim}^2) U_\infty c_\infty}{(\pi R_c^2) U_\infty c_\infty} = \frac{r_{0,\,lim}^2}{R_c^2} \tag{4.10}$$

where η is the collector deposition efficiency, corresponding to a collector with radius of R_c, obtained using the limiting trajectory analysis. This definition applies to a homogeneous collector. The collector deposition efficiency for a homogeneous, fully favorable collector is denoted as η_f.

For the substrate consisting of alternate positively and negatively charged bands, since no particle deposits on the unfavorable bands, the limiting trajectory of the particle can be obtained by selecting R_c such that it is located inside the favorable band. Following this, initiating the backward integration of Eq. (4.8) from the collector surface and following the trajectory to the jet nozzle will provide us with $r_{0,\,lim}$. Once $r_{0,\,lim}$ is found, the collector deposition efficiency corresponding to R_c can be obtained using Eq. (4.10).

4.3 Numerical Results for Particle Trajectories

In this section, we first present results from the particle trajectory analysis near the charge heterogeneous substrate in an impinging jet flow system in order to observe the effect of charge heterogeneity on the particle trajectories. The effect of different parameters such as particle and collector surface potential, width of positive and negative stripes of the collector, and ionic strength of the solution on the particle trajectory will be presented.

The trajectory of a charged particle in an impinging jet flow region near a charged flat surface evolves through the interplay of hydrodynamic and colloidal forces. Particle motion in the vicinity of the collector surface can be divided into two elementary steps [Adamczyk, 1989]. These include; (i) particle transport over macroscopic distances in the bulk of the suspension due to hydrodynamic drag and gravity forces and (ii) particle transport in the immediate vicinity of the interface (distance range of the order 10 - 100 nm) dominated by colloidal forces generated between the particle and the collector surface. The flow distribution in impinging jet cell can be characterized by the dominant role of normal velocity near the stagnation point ($r/R_{jet} < 0.15$) and a dominant role of tangential (radial) velocity at radial distances further away from the stagnation point. Hence, studying particle trajectory and collector efficiency at different distances from the stagnation point will provide a better understanding of the role of hydrodynamic effects, and the extent that they can affect the particle trajectory and collector efficiency.

Typical parameters influencing the trajectories are the particle radius, particle and fluid density, fluid viscosity, flow average velocity, inlet flow Reynolds number, the particle and substrate scaled surface potential, and the dimensions (width and pitch) of the charge heterogeneous stripes on the substrate. It is also worth noting here that, in this study, we consider that all of the particles are negatively charged. This makes a positively charged surface favorable and a negatively charged surface unfavorable for particles with respect to deposition.

4.3.1 Effect of Collector Surface Potential

The effect of substrate surface potential on particle trajectory is illustrated in Figure 4.3. This figure depicts different particle trajectories over different collectors with various surface potentials. This set of results is based on the conditions specified in Table 3.1. The scaled particle surface potential, ($\Psi_p = ze\psi_p/k_bT$), is assumed to be -1. The Reynolds number and solution ionic strength are assumed to be 100 (U_∞=0.1 m/s) and 10^{-3} M, respectively. In Figure 4.3a, the

initial position of the particle was assumed to be such that the particle deposits near the stagnation point whereas in Figure 4.3b, the initial position of the particle was selected such that the particle deposits far from stagnation point.

Let us first consider the particle trajectories over a completely unfavorable surface corresponding to uniform surface potentials of -1 and -2 as shown by the dashed lines in Figure 4.3. Initially, the particles are convected toward the collector by the hydrodynamic and gravity forces. However, at a certain vertical distance from a collector surface (approximately $s = 0.1\ \mu m$), the repulsive effects of electrostatic double layer play a dominant role in preventing the particle from approaching closer to the surface. The repulsion is greater for the substrate with $\Psi_s = -2$, and hence, the particle trajectory over this substrate is further away from the collector surface than the particle trajectory over a collector with surface potential of $\Psi_s = -1$. In sharp contrast to the unfavorable deposition cases, where the particles do not stick to the collector, the particle trajectories terminate on the collector surface under favorable deposition conditions (dotted lines in Figure 4.3). For favorable deposition, the collector surface potential was set to $\Psi_s = +1$.

Figure 4.3 shows the strikingly different trajectories obtained over a heterogeneous collector consisting of alternate bands with positive and negative surface potentials. Two particle trajectories over such a heterogeneous surface have been shown in Figure 4.3, indicated by the legends Ψ_s=(-1,+1) and Ψ_s=(-2,+1). Here, the first parenthesis designates a surface consisting of alternate bands with scaled surface potentials of, -1 and +1, while the second parenthesis designates a surface consisting of alternate bands with surface potentials of -2 and +1. In both cases, the width of negative and positive bands, which are represented by w_n and w_p respectively, is 2 μm ($w_n = w_p = 2\ \mu m$).

Comparing the particle trajectory over a heterogeneous charged surface with the particle trajectories over a homogeneous charged surface provides considerable insight regarding the influence of surface charge heterogeneity on particle deposition. When the substrate consists of alternate positive and negative

bands, the colloidal forces start to play a dominant role in defining the particle trajectory from a vertical distance of about 0.1 μm. When the center of the particle moves over the favorable regions, the attractive force brings the particle closer to the surface. Following this, as the radial component of velocity carries the center of the particle over the unfavorable (repulsive) part of the substrate, the particle moves further away from the substrate. As a result of these alternate repulsive and attractive forces, the particle trajectory becomes oscillatory. The amplitude of the oscillation becomes larger as the particle approaches closer to the surface.

A comparison between particle trajectories depicted in Figures 4.3a and b reveals the role of hydrodynamic effects on the particle trajectories. For the case of $\Psi_s = (-1, +1)$, near stagnation point (Figure 4.3a), the particle deposits after fewer oscillations and the deposition point is very close to the deposition point for the case of completely favorable substrate. In contrast, at locations far from the stagnation point (Figure 4.3b), the particle deposits on the substrate after a number of oscillations. This is due to the fact that the normal component of the velocity that pushes the particle toward the collector surface, dominates in the stagnation point region, while the radial component of fluid velocity dominates far from the stagnation point.

The coupled influence of the hydrodynamic and electrostatic interactions manifests differently on the particle trajectories when the surface potentials of the alternate bands have different magnitudes, such as $\Psi_s = (-2, +1)$, in Figures 4.3a and b. Noting that in this case, the unfavorable (repulsive) interaction is stronger than the favorable interaction, one would expect the deposition to occur significantly downstream compared to the case when the surface potentials on the unfavorable and favorable stripes are $\Psi_s = (-1, +1)$. In the stagnation region, the deposition of the particle occurs in the vicinity of each other for the two cases (Figure 4.3a). In sharp contrast, the deposition of the particle does not at all take place at larger radial distances in the case $\Psi_s = (-2, +1)$ as shown in Figure 4.3b. Therefore, with the same charge heterogeneity pattern

on the substrate, the particle deposition can manifest itself quite differently depending on the nature of the velocity field. On the basis of the results shown in Figure 4.3, it can be deduced that the coupled effects of collector surface charge heterogeneity and hydrodynamic forces result in an oscillatory motion of the particle over a micropatterned substrate consisting of both favorable and unfavorable stripes.

4.3.2 Effect of Band Width at Constant Favorable Area Fraction

The influence of band width on particle trajectory was studied in a scenario in which the pitch of the heterogeneity (p) was varied while keeping the favorable area fraction of the collector ($\lambda_{patterned}$) constant at 50%. Figure 4.4 shows the dependence of oscillating particle trajectory on the width of favorable and unfavorable bands for constant $\lambda_{patterned}$. This figure is obtained with the conditions stated in Table 3.1, for regions far from the stagnation point. The Reynolds number and solution ionic strength are assumed to be 100 ((U_∞=0.1 m/s) and 10^{-3} M, respectively. The particle surface potential,Ψ_p, is -2 and the collector surface potential,Ψ_s, is $(-2, +2)$. The particle trajectory has been obtained for two different pitches of $p = 4$ μm and $p = 10$ μm. Figure 4.4b illustrates the zoomed in trajectories inside the dashed box in Figure 4.4a.

It can be seen from Figure 4.4b that the wavelength of the oscillating trajectory, Λ, is equal to the pitch (p).

Another feature of the heterogeneous deposition observed from Figure 4.4 is that although the ratio of favorable surface area to the total collector surface area ($\lambda_{patterned} = 50\%$) is the same for both cases of $p = 4$ μm and $p = 10$ μm, the particle deposits slightly earlier on the collector with wider stripes (i.e. $p = 10$ μm). The reason for this behavior can be explained by taking a closer look at Eq. (3.12). The first term in Eq. (3.12), Dl, gives the force due to the strength of surface potentials while the second term, Da, arises due to asymmetry of the potentials Ψ_p and Ψ_s. Notably, the second term vanishes

when the surface potentials of the particle and the collector are identical (both sign and magnitude are same). Let us consider a scenario where a negatively charged particle with $\Psi_p = -2$, is moving over a substrate consisting of alternate negative and positive bands that have surface potentials given by $\Psi_s = (-2, +2)$. For the favorable case, when the center of the negative particle is located over a positive band, the second term in Eq. (3.12) will have a large finite value. On the other hand, for the unfavorable case, when the center of the particle is located over the negative band, the second term in Eq. (3.12) will vanish. In both cases, the first term of Eq. (3.12) will be identical. Consequently, the attractive interaction will have a larger magnitude than the repulsive interaction in the above scenario. Thus, for a negatively charged particle, an increase in the width of the positive band can potentially affect the particle trajectory more markedly than an increase in the width of the negative band.

4.3.3 Effect of Solution Ionic Strength

The ionic strength of a solution affects the Debye length of the EDL interaction, thereby influencing the range of the colloidal forces acting on the depositing particles. Figure 4.5 depicts the extent to which the particle trajectory is affected by changes in ionic strength of the solution. The results depicted in Figure 4.5 were obtained by computing the particle trajectories for two ionic strengths of 10^{-3}M and $10^{-3.5}$M. The Reynolds number is assumed to be 100 ((U_∞=0.1 m/s). All the other conditions are as stated in Table 3.1.

Two cases have been shown in this figure, one corresponds to favorable deposition when the collector surface potential, Ψ_s, is +1 over the entire collector surface (dashed lines), and the other is when $\Psi_s = (-1, +1)$ (solid lines). The positive and negative band widths are equal and assumed to be 2 μm. First we compare the two favorable cases (dashed lines) with different ionic strengths. It can be seen that at lower ionic strength ($I = 10^{-3.5}$M), the particle will deposit on a homogeneously favorable surface earlier since it experiences a greater electrostatic double layer attraction. A comparison between the two particle

trajectories with different solution ionic strengths for the case when the heterogeneous substrate consists of positive and negative bands with surface potential of $+1$ and -1 (solid lines) indicates that the particle in the solution with lower ionic strength will experience oscillation with larger amplitudes and deposit earlier.

As observed in Figure 4.5, the oscillations in the particle trajectory with greater Debye length (lower ionic strength) starts at larger normal distances from the substrate and the amplitude of these oscillations are more pronounced. It is also noted that for the case of the lower ionic strength, I=$10^{-3.5}$ M, the distance between the locations at which the particle touches the completely favorable surface and the heterogeneous micropatterened surface is considerably larger compared to the corresponding distance for I=10^{-3} M. This implies that the effect of surface charge heterogeneity on particle trajectory becomes more significant as one decreases the solution ionic strength.

4.4 Particle Distribution Over heterogeneous Substrate

In order to obtain an insight into the behaviour of particle deposition on the micropatterned charged heterogeneous substrate, we first study how the distribution of deposited particles vary with increasing radial distances on the collector surface as one moves away from the stagnation point. From a cursory glance at the geometry, one might infer that the favorable bands will be uniformly accessible for particle deposition. This, however, is not the case, since radially moving away from the stagnation point, the deposition process progressively becomes non-uniform, and the leading regions of the favorable stripes on the collector become inaccessible for particle deposition. The available (accessible) regions of the favorable stripes progressively diminish as the radial distance from the stagnation region increases.

To assess what fraction of the favorable surface (the favorable stripes) re-

mains accessible for particle deposition as one moves away radially from the stagnation point, we conducted some simulations as described below. Each favorable stripe was discretized into N segments (generally N=20). Starting from the end of each such segment of a favorable stripe, which we will refer to as the landing point, we solved the trajectory equations backward (with negative time steps, $\Delta\bar{t}$) to determine the initial release location of the particle. The initial release position was deemed feasible if it originated from within the impinging jet nozzle, implying that a particle starting out from within the nozzle can deposit on the landing point. Termination of the trajectory at any other point in the computational domain constituted an infeasible trajectory, implying that the particle could not deposit at the chosen landing point (in other words, the landing point being investigated is inaccessible). The trajectory computation was repeated for each location of the landing point on a given favorable stripe. This procedure is depicted in Figure 4.6. The dashed line in this figure represents the infeasible trajectory while the accepted particle trajectory is shown by solid line and originates at the impinging jet nozzle.

For each favorable stripe, the calculation procedure delineated above provides the location of the first accessible landing point on the stripe. As one moves radially outward from the stagnation point, the first landing point accessible to particle deposition on a favorable stripe is found to move toward the trailing edge of the stripe (the ending part of the given stripe). In other words, the fraction of the favorable stripe surface that is accessible to particle deposition gradually diminishes as one moves radially outward from the stagnation point.

To facilitate further analysis, we define a quantity, the accessible fraction of favorable (AF_F) surface, as

$$AF_F = \frac{w_{accessible}}{w_p} \tag{4.11}$$

where $w_{accessible}$ is the width of the favorable stripe accessible to particle deposition, and w_p is the overall width of the favorable stripe (Figure 4.6). The width $w_{accessible}$ can be determined from the trajectory analysis outlined above by sim-

ply finding the distance between the first landing point accessible for particle deposition and the trailing edge of the stripe. The region of each favorable stripe rendered inaccessible for particle deposition is then given by $(w_p - w_{accessible})$, and is located at the leading edge of each favorable band.

4.4.1 Effect of Collector Favorable Area Fraction

Figure 4.7 depicts the variation of the accessible fraction of a favorable band (AF_F) as a function of the distance of that band from the stagnation point. In this figure, the horizontal axis represents the band number in radial direction, N_b. In obtaining the results, it was also assumed that the pitch is $p = 20\ \mu m$ which indicates that the end of first favorable band ($N_b = 1$) on the collector is located at the radial distance of 20 μm from the stagnation point, the end of the second favorable band ($N_b = 2$) is located at the radial distance of 40 μm from the stagnation point, and so forth. For a fixed pitch, by changing the ratio of the width of positive and negative stripes (w_p and w_n), one can get different values of collector favorable area fraction, $\lambda_{patterned}$. The Reynolds number and the particle surface potential were assumed to be 100 and $\Psi_p = -2$ respectively. The collector consisted of favorable and unfavorable bands with surface potential of $\Psi_s = (-2, +2)$. The ionic strength of the solution was $10^{-3.5}$M. Other parameters were same as those stated in Table 3.1.

In order to obtain these results, we computed the AF_F for each favorable band on the collector surface corresponding to a given $\lambda_{patterned}$. In this study, we assume that the central band (at r=0) on the collector surface is unfavorable.

It is evident from Figure 4.7 that the accessible fraction of favorable band (AF_F) decreases with increasing distance from the stagnation point. This can be explained by considering the ratio of normal to tangential components of fluid velocity. In the vicinity of stagnation point, since the normal component is larger than the tangential component, almost the entire length of the favorable band is accessible for particle deposition (the band acts as a uniform collector). In contrast, at larger distances from the stagnation point, since the tangential

component is dominant compared to the normal component, a significant part of the favorable band is not accessible for particle deposition. For instance, in the case of $w_n = w_p = 10\ \mu m$ (open circles in Figure 4.7), although $\lambda_{patterned}$ is 50%, which implies that geometrically half of the collector surface is covered by favorable stripes, the AF_F decreases with increasing distance from the stagnation point. For instance, on the 20^{th} band (the radial distance of the end of this band from the stagnation point is 400 μm), AF_F is about 0.4. Thus the overall surface becomes progressively unfavorable as one moves radially away from the stagnation point.

Figure 4.7 also indicates that the AF_F depends on the ratio of the width of favorable and unfavorable bands (i.e. the ratio of w_p to w_n). We note that keeping the pitch fixed, altering the ratio of w_p to w_n results in different values of $\lambda_{patterned}$. It can be observed from Figure 4.7 that the AF_F increases by increasing the width of favorable band with respect to unfavorable band. For a constant pitch, when the ratio of w_p to w_n is less than unity ($\lambda_{patterned} < 50\%$), the accessible fraction of favorable band decreases sharply with the distance from the stagnation point. For instance, when $w_p = 5\ \mu m$ and $w_n = 15\ \mu m$ (open squares), AF_F approaches zero for band number $N_b = 10$ which is located in the vicinity of the stagnation point (the radial distance of the end of this band from the stagnation point is 200 μm). In contrast, when the ratio of w_p to w_n is larger than unity ($\lambda_{patterned} > 50\%$), the accessible fraction of favorable band decreases smoothly with respect to the distance from the stagnation point and appears to attain a limiting value. For instance, for the case of $w_p = 15\ \mu m$ and $w_n = 5\ \mu m$ ($\lambda_{patterned} = 75\%$) (upright triangle), AF_F becomes almost constant for all of the stripes beyond the third stripe.

The results presented above imply that when less than 50% of the substrate is favorable, we can render the collector completely unfavorable for particle deposition by increasing the ratio of tangential to normal components of fluid velocity while other parameters remain unchanged.

4.4.2 Effect of Band Width at Constant Favorable Area Fraction

Figure 4.8 depicts the effects of the width of unfavorable and favorable band on AF_F when the ratio of these widths (w_p to w_n) is maintained constant. This set of results is obtained based on the same conditions used for Figure 4.7, the only exception being that in this figure, instead of pitch, the ratio of w_p to w_n is kept constant.

Figure 4.8 shows the variation of AF_F with the favorable band number for three different values of pitch, $p = 10\ \mu m$, $p = 20\ \mu m$, and $p = 200\ \mu m$. It is evident that for a given favorable band, the value of AF_F is the same for three different values of pitch, which indicates that the pitch does not have a significant effect on AF_F.

4.4.3 Effect of Fluid Velocity

The effect of fluid velocity on accessible fraction of favorable band has also been studied and the results are shown in Figure 4.9. This figure depicts the variation of AF_F as one proceeds radially outward from the stagnation point over consecutive favorable bands for three different fluid velocities. The widths of the favorable and unfavorable stripes are equal and assumed to be 5 μm in these calculations. All the other parameters are the same as Figure 4.7. It can be seen from this figure that although the value of AF_F for each favorable band increases slightly by decreasing the fluid velocity, overall the fluid velocity does not have a significant effect on AF_F. This implies that the effect of hydrodynamic interactions on the value of AF_F manifests itself as the ratio of normal to tangential fluid velocity, and not their absolute magnitudes. The results in Figure 4.9 suggest that an increase in the magnitude of fluid velocity which means both tangential and normal component of fluid velocity increase equally, does not affect the value of AF_F. However, changing the ratio of tangential to normal component of fluid velocity (for instance by getting further away from the stagnation point) can affect the value of AF_F significantly as was shown in

Figure 4.7.

The foregoing discussion highlights the role of coupled effects of hydrodynamics and colloidal forces in controlling the particle deposition and distribution of deposited particles on the collector surface. Due to the tangential component of fluid velocity, a region near the leading edge of each favorable band becomes inaccessible for particle deposition. In fact, for small ratios of w_p to w_n ($\lambda_{patterned} < 50\%$), in the regions far from the stagnation point where the tangential velocity component is dominant, the inaccessible region can extend to the entire width of the favorable band. This renders the favorable band unfavorable with respect to deposition. These observations provide considerable insight regarding the distribution of the deposited particles on the micropatterned collector. Since no particle deposits on unfavorable bands and the accessible area for particle deposition on favorable bands decreases at larger radial distances from the stagnation point, it can be deduced that for a collector consisting of alternate positive and negative stripes, the number of deposited particles will decrease with increasing distance from the stagnation point.

4.5 Particle Deposition in Context of Trajectory Analysis

In this section, the patchwise heterogeneity model [Song *et al.*, 1994], which has been extensively used to predict particle deposition rate in the presence of charge heterogeneity will be described first. Following this, particle deposition rate in form of collector deposition efficiency will be calculated over both homogeneous and heterogeneous collectors using trajectory analysis. The numerically obtained results of particle deposition rate over heterogeneous collectors will then be compared to those calculated by analytical expressions based on the patchwise heterogeneity model.

4.5.1 Available Model Predicting Particle Deposition Rate: Patchwise Heterogeneity Model

The method that has been used in literature to evaluate the particle deposition rate over charge heterogeneous substrates is called two-site patchwise heterogeneity model [Song *et al.*, 1994]. In this method, surfaces with charge heterogeneity have been modelled as a patchwork mosaic with individual patches treated as isolated homogeneous regions having uniform surface charge [Elimelech *et al.*, 2003]. These patches are considered large enough compared to particle size, whereby the interactions between patch boundaries have negligible effects on particle deposition behaviour. According to patchwise heterogeneity model, the overall particle deposition rate over a charge heterogeneous surface is the linear combination of deposition rates over various surface patches. The predicted overall particle deposition rate over heterogeneous substrates using the patchwise heterogeneity model is [Song *et al.*, 1994]

$$\eta_{patch} = \sum_{i=1}^{n} \lambda_i \, \eta_i \tag{4.12}$$

where η_i is the particle deposition rate onto patches of type i, and λ_i is the surface fraction of patches of type i.

When only one type of favorable and one type of unfavorable patch exists on the substrate, the above equation simplifies to

$$\eta_{patch} = \lambda_{patterned} \, \eta_f + (1 - \lambda_{patterned}) \, \eta_u \tag{4.13}$$

where η_{patch} is the overall deposition efficiency, and η_f and η_u are the deposition efficiencies for completely favorable and completely unfavorable regions, respectively. Here, $\lambda_{patterned}$ is the surface area fraction of the collector that is favorable. A common way of calculating η_{patch} using Eq. (4.13) is to first assume that the substrate is a homogeneous surface bearing the surface potential corresponding to the favorable case. The particle deposition over such a surface (η_f) can be obtained by various theoretical or experimental methods. In the next step, it is assumed that the same substrate is a homogeneous surface bearing the surface potential corresponding to the unfavorable case. The particle

deposition over such a surface (η_u) can be obtained as well. Evaluating η_f and η_u leads to the overall particle deposition rate by using Eq. (4.13).

In this study, considering all of the operating and physicochemical properties of the modelled system, the particle deposition rate over the unfavorable substrate is zero, as was shown in Figure 4.3 for the unfavorable collectors, i.e., $\Psi_s = -2$ and $\Psi_p = -2$ depicted by dashed lines. As a result, Eq. (4.13) can be written in a simplified form as

$$\eta_{patch} = \lambda_{patterned}\, \eta_f \tag{4.14}$$

This equation indicates a linear relation between overall particle deposition over a heterogeneous collector and particle deposition over a homogeneous fully favorable collector. According to the patchwise heterogeneity model, the ratio of particle deposition over a heterogeneous substrate to the particle deposition over a homogeneous fully favorable substrate (η_{patch}/η_f) is directly proportioned to the fraction of the substrate surface that is covered with favorable charge ($\lambda_{patterned}$). This means that for a collector with favorable area fraction of $\lambda_{patterned} = 50\%$, the overall particle deposition rate, η_{patch} is half of the overall particle deposition over a homogeneous fully favorable collector.

The patchwise heterogeneity model provides a remarkably accurate prediction of the particle deposition over surfaces with macroscopic charge heterogeneity [Koopal and Dukhin, 1993, Song *et al.*, 1994, Tien, 1989]. However, it has been observed that when the size of the heterogeneous bands becomes comparable to the size of the approaching particles, the patchwise heterogeneity model breaks down [Elimelech *et al.*, 2003]. According to Eq. (4.12), the failure of the patchwise heterogeneity model in predicting the deposition efficiency for micro-scale charge heterogeneity can either stem from using the erroneous values of $\lambda_{patterned}$, or it can stem from the fact that the assumption of linear relationship between (η_{patch}/η_f) and $\lambda_{patterned}$ is not valid for micro-scale charge heterogeneity. This means that in the presence of micro-scale charge heterogeneity, the concept of finding particle deposition by using a simple averaging

process as depicted in Eq. (4.12) may result in erroneous results for particle deposition.

In order to find out which of the two stated assumptions (the linear relation between η_{patch}/η_f or the erroneous values of $\lambda_{patterned}$) is the reason behind the failure of patchwise heterogeneity model, we first modify the patchwise heterogeneity model expression by replacing the nominal value of collector favorable area fraction $\lambda_{patterned}$ by its actual value inside the patchwise heterogeneity model equation, Eq. (4.17). Furthermore, using the trajectory analysis, we can obtain the particle deposition over collectors with different favorable area fractions. Comparing these results with those predicted by original and modified patchwise heterogeneity model, one can clarify the reason behind the failure of patchwise heterogeneity model. If the numerical values of particle deposition (obtained by trajectory analysis) are in good agreement with those predicted by modified patchwise heterogeneity model (which accounts for actual values of collector favorable area fraction), it can be deduced that the concept of linear relation between η_{patch}/η_f and $\lambda_{patterned}$ is valid and the failure of original patchwise heterogeneity model in predicting particle deposition is due to the fact that $\lambda_{patterned}$ is not the true representative of actual favorable fraction of the collector and one has to consider the existence of inaccessible part of favorable stripes as well. However, if the numerical values of particle deposition deviate from those predicted by both original and modified patchwise heterogeneity model, it can be deduced that the concept of linear relation between η_{patch}/η_f and $\lambda_{patterned}$ is not valid for the case of particle deposition over micro-scale charge heterogeneous substrate. This implies that the simple averaging procedures such as the one proposed by patchwise heterogeneity model are not comprehensive enough to capture the behaviour of particle deposition in the presence of micro-size charge heterogeneity.

The foregoing results in Section 4.4, particularly Figure 4.7 suggests that due to the presence of the inaccessible part at the leading edge of each favorable band, the actual favorable area fraction of the collector is less than its nominal

(geometrical) favorable area fraction ($\lambda_{patterned}$). To account for the effects of both nominal collector favorable area fraction ($\lambda_{patterned}$) and the inaccessible part of the favorable regions, we modify the patchwise heterogeneity expression by replacing $\lambda_{effective}$ by the actual favorable area fraction of the collector defined as

$$\lambda_{effective} = \overline{AF_F} \times \lambda_{patterned} \tag{4.15}$$

where $\lambda_{effective}$ is the actual favorable area fraction of the collector, and $\overline{AF_F}$ is the average accessible fraction of favorable band, defined as

$$\overline{AF_F} = \frac{\int_0^{R_c} AF_F(r)\, dr}{R_c} \tag{4.16}$$

where $\overline{AF_F}$ is the average accessible fraction of favorable bands up to the distance R_c from the stagnation point. Utilizing Eq. (4.15), the patchwise heterogeneity model expression for deposition efficiency, Eq. (4.14), can be modified as:

$$\eta_{patch} = (\overline{AF_F} \times \lambda_{patterned})\ \eta_f \tag{4.17}$$

It is evident from the above expression that in calculating the overall particle deposition over the heterogeneous substrates, Eq. (4.17) accounts for both the nominal favorable area fraction of the collector ($\lambda_{patterned}$) and accessible fraction of each favorable band (AF_F). From Eq. (4.17), it can be deduced that when $\overline{AF_F}$ takes the value of unity, the modified patchwise heterogeneity model expression, Eq. (4.17) becomes identical to original patchwise heterogeneity model equation, Eq. (4.14).

The variation of the scaled overall deposition efficiency (η_{patch}/η_f) obtained using the modified patchwise heterogeneity model (symbol-solid lines), Eq. (4.17), with respect to $\lambda_{patterned}$ is shown in Figure 4.10 for the values of pitch comparable to the particle size. The results are shown corresponding to two different distances from the stagnation point, $R_c = 60\ \mu m$ and $R_c = 800\ \mu m$. All the other parameters are the same as in Figure 4.7. In Figure 4.10, the dashed diagonal line represents the η_{patch}/η_f predicted by the original patchwise heterogeneity model, Eq. (4.14), whereas the line-symbol combination denote the

values of η_{patch}/η_f obtained using the modified patchwise heterogeneity model expression, Eq. (4.17), for $R_c = 60\ \mu m$ (squares) and $R_c = 800\ \mu m$ (circles). In order to obtain these results, we calculated $\overline{AF_F}$ corresponding to each value of $\lambda_{patterned}$ using the radial variations of AF_F shown in Figure 4.7 and numerically integrating Eq. (4.16).

Figure 4.10 indicates that in the vicinity of the stagnation point ($R_c = 60\ \mu m$), since the normal component of velocity is dominant, the value of $\overline{AF_F}$ is close to unity, which renders the value of η_{patch}/η_f to be nearly identical to the prediction of the original patchwise heterogeneity model over the entire range of $\lambda_{patterned}$. In contrast, in the regions far from the stagnation point ($R_c = 800\ \mu$m), due to the dominant role of tangential velocity, η_{patch}/η_f deviates from the results predicted by the patchwise heterogeneity model. The deviation is more pronounced for smaller values of $\lambda_{patterned}$.

To summarize, the coupled influence of the collector surface charge heterogeneity and the hydrodynamic forces on the particle distribution over the collector surface in impinging jet flow manifests differently at different radial distances from the stagnation point. Due to the dominant role of the normal velocity in the vicinity of the stagnation point, the nominal collector favorable area fraction ($\lambda_{patterned}$) is identical to the actual collector favorable area fraction ($\lambda_{effective}$). This implies that the values of particle deposition over micropatterend substrates predicted by modified and original patchwise heterogeneity model are identical in this region as well. In contrast, far from stagnation point, owing to the greater influence of tangential velocity, the nominal collector favorable area fraction ($\lambda_{patterned}$) is greater than the actual collector favorable area fraction ($\lambda_{effective}$). This implies that for a specified value of $\lambda_{patterned}$, the extent of particle deposition over micropatterend substrates predicted by the modified patchwise heterogeneity model is smaller than that predicted by the original patchwise heterogeneity model far from the stagnation point.

In the next section, the numerically obtained collector deposition efficiencies over collectors with different favorable area fractions will be compared to

those predicted by both the original and the modified patchwise heterogeneity models to clarify the reason behind the failure of the patchwise heterogeneity model in predicting particle deposition in the presence of micro-scale charge heterogeneity.

4.5.2 Numerical Results for Collector Deposition Efficiency

To this point, we have developed a trajectory model that can be used to obtain particle trajectories over both homogeneous and heterogeneous substrates. Incorporating this model and evaluating the limiting trajectory corresponding each point on the substrate surface, one can calculate the extent of particle deposition corresponding each point on the collector surface in form of collector deposition efficiency (η) by employing Eq. (4.10).

In order to determine the extent to which the particle deposition behaviour is affected by charge heterogeneity, we first obtain particle deposition rate in form of collector deposition efficiency (η) for a homogeneous favorable collector. We denote this deposition efficiency as η_f. Following this, using the methodology discussed in Section 4.2.2, we obtain the collector efficiency for the case when the heterogeneous substrate consists of alternate favorable and unfavorable bands. Comparing these two sets of results highlights the effect of surface charge heterogeneity on the collector deposition efficiency.

Figure 4.11 shows the collector efficiency corresponding to different scaled radial positions, R_c/R_{jet}, on the collector surface. In this figure, the solid line denotes the collector efficiency for a homogeneous favorable collector, η_f, while the other lines represent the collector efficiencies for heterogeneous substrates for different values of favorable area fraction of the collector ($\lambda_{patterned}$). These results are obtained based on the same conditions as in Figure 4.7. For the case of homogeneous favorable collector, it can be seen that in the vicinity of the stagnation point ($R_c/R_{jet} < 0.15$), uniform deposition conditions prevail, whereas further away from stagnation point, the deposition efficiency decreases

and the collector is not uniform [Adamczyk *et al.*, 2001]. For the case of heterogeneous collector, we defined R_c as the distance of the end of each favorable band from the stagnation point. For instance, since we assumed the central band is always unfavorable, and the pitch is $p = 20\ \mu m$, the R_c corresponding to the first favorable band is 20 μm. Similarly, R_c corresponds to the second favorable band is 40 μm.

It can be seen from Figure 4.11 that the collector efficiency on the heterogeneous micropatterend substrate decreases by decreasing the favorable area fraction ($\lambda_{patterned}$). It is also evident that the presence of charge heterogeneity on the collector surface makes the collector more non-uniform at larger distances from stagnation point. For all values of $\lambda_{patterned}$, the deposition efficiency decreases by increasing the distance from the stagnation point. For small values of $\lambda_{patterned}$ (i.e. $\lambda_{patterned} < 50\%$), the deposition efficiency drops sharply with respect to distance from stagnation point. For larger values of $\lambda_{patterned}$ (i.e. $\lambda_{patterned} > 50\%$), on the other hand, the deposition efficiency drops more smoothly with respect to radial distance from stagnation point. This behavoiur is similar to what we observed earlier in Figure 4.7. Comparing these two figures indicates that by decreasing the favorable area fraction of the collector, $\lambda_{patterned}$, both collector efficiency and accessible fraction of the favorable band decrease sharply with increasing radial distance from stagnation point, while for larger values of $\lambda_{patterned}$ (i.e. $\lambda_{patterned} > 50\%$), both collector efficiency and accessible fraction of the favorable band decrease more slowly.

Figure 4.12 depicts the variation of scaled collector deposition efficiency (η/η_f) with respect to $\lambda_{patterned}$ for a heterogeneous collector with radius of $R_c = 300\ \mu m$. The square-legend line represents the particle deposition rate obtained numerically using the trajectory analysis. The triangle-legend line represents the particle deposition rate predicted by the original patchwise heterogeneity model, Eq. (4.14) whereas the circle-legend line represents the particle deposition rate predicted by the modified patchwise heterogeneity model, Eq. (4.17). These results correspond to the flow Reynolds number of 180

($U_\infty = 0.18\ m/s$), solution ionic strength of 10^{-3}M, and particle surface potential, Ψ_p, of -2. The collector scaled surface potential, Ψ_s, is (-2,+2). The pitch is constant and equal to 10 μm. The numerically obtained particle deposition efficiencies (square-legend line) are calculated by first finding the limiting trajectory corresponding to $R_c = 300\ \mu m$, using the procedure described in Section 4.2.2, for different values of $\lambda_{patterned}$, i.e., from $\lambda_{patterned} = 0$ to $\lambda_{patterned} = 100\%$. Finding the limiting trajectory provides the value of $r_{0,\ lim}$ which can be incorporated in Eq. (4.10) to calculate the particle deposition rate in form of collector deposition efficiency, η. Typically, for this pitch ($p = 10\ \mu m$), $\lambda_{patterned} = 10\%$ will correspond to $w_n = 9\ \mu m$ and $w_p = 1\ \mu m$, while $\lambda_{patterned} = 100\%$ will correspond to $w_n = 0\ \mu m$ and $w_p = 10\ \mu m$. The latter case represents the completely favorable collector (η=η_f). The collector deposition efficiencies predicted by the original patchwise heterogeneity model (triangle-legend line) were obtained employing Eq. (4.14) whereas the collector deposition efficiencies predicted by the modified patchwise heterogeneity model (circle-legend line) were obtained employing Eq. (4.17).

It can be seen from Figure 4.12 that the numerically obtained values of collector deposition efficiency deviate significantly from those predicted by both the original and modified patchwise heterogeneity models. This deviation is more pronounced for larger values of $\lambda_{patterned}$. According to our numerical simulations (square-legend line in Figure 4.12), the collector deposition efficiency over a heterogeneous collector, η, increases by increasing the collector favorable area fraction, $\lambda_{patterned}$. However, the interesting feature of Figure 4.12 is that this increase is not uniform as was predicted by the patchwise heterogeneity model. When $\lambda_{patterned}$ is less than 40%, increasing the value of $\lambda_{patterned}$ slightly by increasing the width of positive band (keeping the pitch unchanged) will increase the particle deposition significantly, whereas when half of the surface is covered with favorable bands, $\lambda_{patterned} > 50\%$, increasing the width of favorable band will not cause a considerable increase in deposition efficiency. Consequently, a surface with $\lambda_{patterned} = 50\%$ has an almost comparable deposition efficiency as

a fully favorable surface with $\lambda_{patterned} = 100\%$ ($\eta \simeq \eta_f$). This means that when a surface is initially unfavorably charged, the presence of charge heterogeneity in form of a small fraction of favorable charged regions leads to an enormous increase in the particle deposition rate. This has been extensively reported in literature [Adamczyk *et al.*, 2003, Song *et al.*, 1994]. On the other hand, if the surface is initially favorably charged, the presence of heterogeneity in form of unfavorably charged regions will not change the particle deposition rate significantly.

As can be clearly seen in Figure 4.12, the numerically obtained values of collector deposition efficiency deviate significantly from those predicted by both the original and modified patchwise heterogeneity models. This means that modifying the original patchwise heterogeneity equation by merely replacing $\lambda_{patterned}$ by $\lambda_{effective}$ does not improve the predictions of the patchwise heterogeneity model for particle deposition efficiency. Figure 4.12 shows that the variation of scaled collector deposition efficiency η/η_f with respect to $\lambda_{patterned}$ does not follow a linear relationship in contrast to what is suggested by the patchwise heterogeneity model. This implies that the failure of the patchwise heterogeneity model in predicting the particle deposition in the presence of micro-scale heterogeneity originates from the fact that the assumption of a simple linear relationship between particle deposition (η) and collector favorable area fraction ($\lambda_{patterned}$) is not valid for the case of micro-scale heterogeneity when the size of charge heterogeneity is comparable to particle size.

The numerical simulation results for particle deposition over the heterogeneous substrate in Figure 4.12 illustrate that although there is a part at the leading edge of the favorable stripes all over the collector surface that is inaccessible for particle deposition and acts as unfavorable region, the overall particle deposition rate over the heterogeneous substrate is larger than that predicted by both the original and the modified patchwise heterogeneity models. For instance, in case of a substrate with nominal favorable area fraction of 50%, although more than 50% of the collector surface can be assumed unfavor-

able (due to the presence of inaccessible part at the leading edge of favorable stripes) the particle deposition rate over such a surface inside the impinging jet system is very close to the particle deposition rate over a fully favorable surface. This indicates that although the particle deposition rate is zero over unfavorable regions, the particle deposition rate over the accessible part of favorable bands is large enough so that the overall particle deposition rate over the entire surface of heterogeneous substrate approaches a value comparable to the particle deposition rate over a fully favorable surface. This behaviour can be attributed to the coupled effects of hydrodynamic and colloidal interactions inside the impinging jet system in the vicinity of the heterogeneous substrate which will be discussed in more detail in next chapter.

4.6 Summary

A trajectory model has been developed to investigate the effect of surface charge heterogeneity on particle deposition rate and particle trajectory in the vicinity of the heterogeneous substrate inside the impinging jet flow geometry. The surface charge heterogeneity was modelled as concentric circular bands with different negative and positive surface potentials. This model takes into account the effects of external forces acting on the particles that were discussed in Chapter 3. The trajectory equations were solved numerically. The simulations performed in this study reveal that the trajectory of a charged particle near a micropatterned charged collector consisting of alternate positive and negative bands becomes oscillatory due to the alternating attractive and repulsive particle-substrate colloidal forces. The wavelength and amplitude of this oscillating trajectory can be controlled by changing the width of the favorable and the unfavorable bands, the particle and substrate surface potentials, and solution ionic strength. The particle trajectories in the vicinity of the heterogeneous substrate indicate that it is possible to render a partly favorable collector to behave as a completely unfavorable collector by simply increasing the ratio of the tangential to the normal

fluid velocity over the substrate.

It was also observed that due to the interplay of hydrodynamic and colloidal interactions, there exists a part at the beginning of favorable stripes that is inaccessible for particle deposition and acts as unfavorable region, implying that the actual favorable area fraction of the collector is less than its nominal value.

Furthermore, the patchwise heterogeneity model normally used to predict the particle deposition rate over heterogeneous surfaces was shown to be inadequate for micropatterned charge heterogeneous substrates. This model provides a linear relationship between the particle deposition rate over a heterogeneous collector and the particle deposition over a fully favorable collector where the coefficient of this linear equation is the collector favorable area fraction, $\lambda_{patterned}$. It has been increasingly stated in literature that patchwise heterogeneity model fails to predict the particle deposition rate in case of micro-size heterogeneity when the size of heterogeneity is comparable to the particle size. By taking into account the actual collector favorable area fraction, the expression for the patchwise heterogeneity model has been modified.

Finally, using the trajectory analysis, the particle deposition rate over heterogeneous collectors consisting of alternate unfavorable and favorable bands was calculated for different values of collector favorable area fraction. The numerical results for particle deposition rate depict a significant deviation from those predicted by both the modified and the original patchwise heterogeneity models. The deviation of numerically obtained values of particle deposition rate from those predicted by both the modified and the original patchwise heterogeneity models indicates that the failure of the patchwise heterogeneity model does not stem from the erroneous values of collector favorable area fraction since modifying these values did not improve the patchwise heterogeneity model predictions for particle deposition. Consequently, it was clarified that the failure of the patchwise heterogeneity model originates from the concept of linear relationship between the particle deposition rate over heterogeneous collector and

the particle deposition rate over fully favorable collector based on averaging process which is not comprehensive enough to capture all the physics behind the particle motion in the vicinity of heterogeneous substrate.

According to the numerical simulation results, when half of the collector surface is covered with favorable charge, the particle deposition rate is almost identical to the particle deposition rate over a fully favorable surface. It was observed that similar to what has been reported in literature, the particle deposition rate increases significantly by an slight increase in the collector favorable fraction when the surface is initially unfavorable. These results were attributed to the coupled effects of hydrodynamic and colloidal interactions between the particles and heterogeneous collector. A more detailed discussion will be provided in next section by conducting simulations based on Eulerian methods to determine particle deposition behaviour in the presence of micro-scale charge heterogeneity.

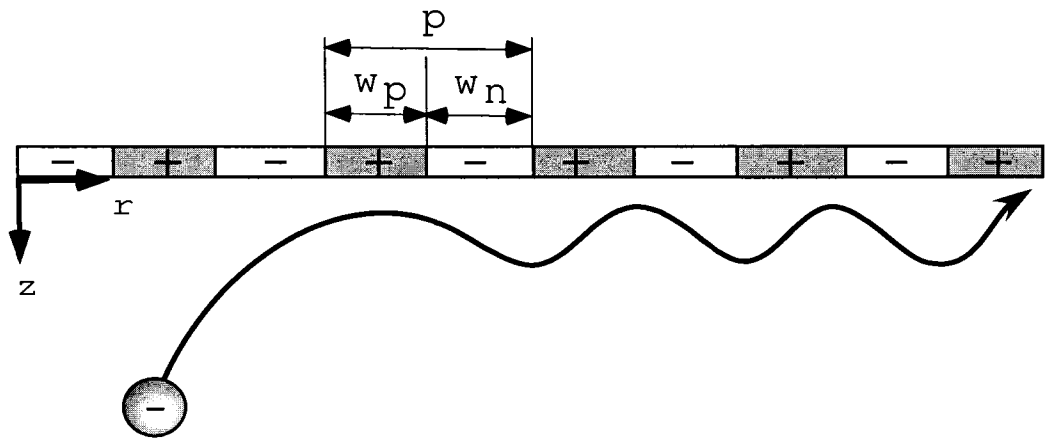

Figure 4.1: A schematic illustration of the trajectory of a negatively charged particle over a micropatterned substrate consisting of alternate negative and positive bands. Plain stripes represent negatively charged regions and shaded stripes represent positively charged regions.

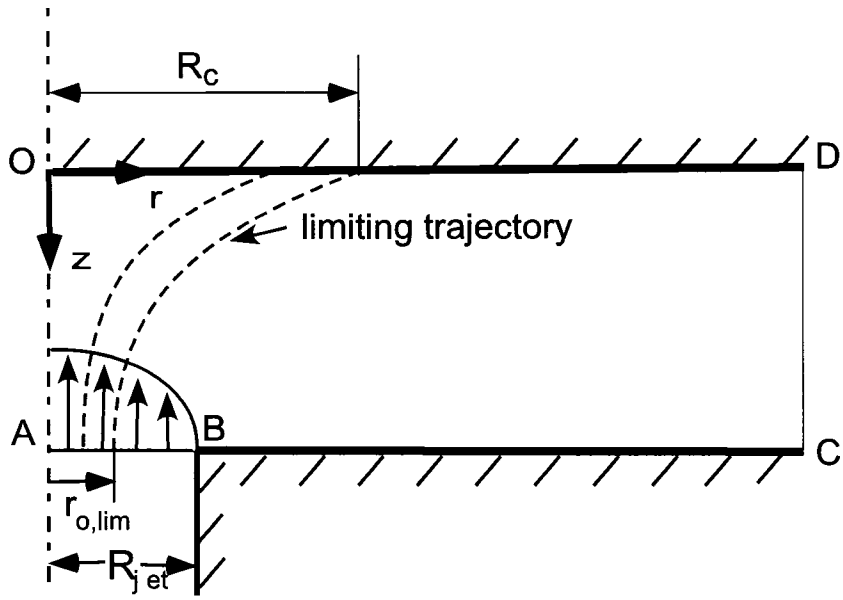

Figure 4.2: A schematic representation of limiting trajectory. Dashed lines represent two particle trajectories. The limiting trajectory corresponding to the distance R_c from the stagnation point on the collector starts from the jet tip at the radial distance of $r_{0,\,lim}$. All the other trajectories start at the jet tip with the radial position less than $r_{0,\,lim}$ will terminate on the collector inside the circle with radius R_c.

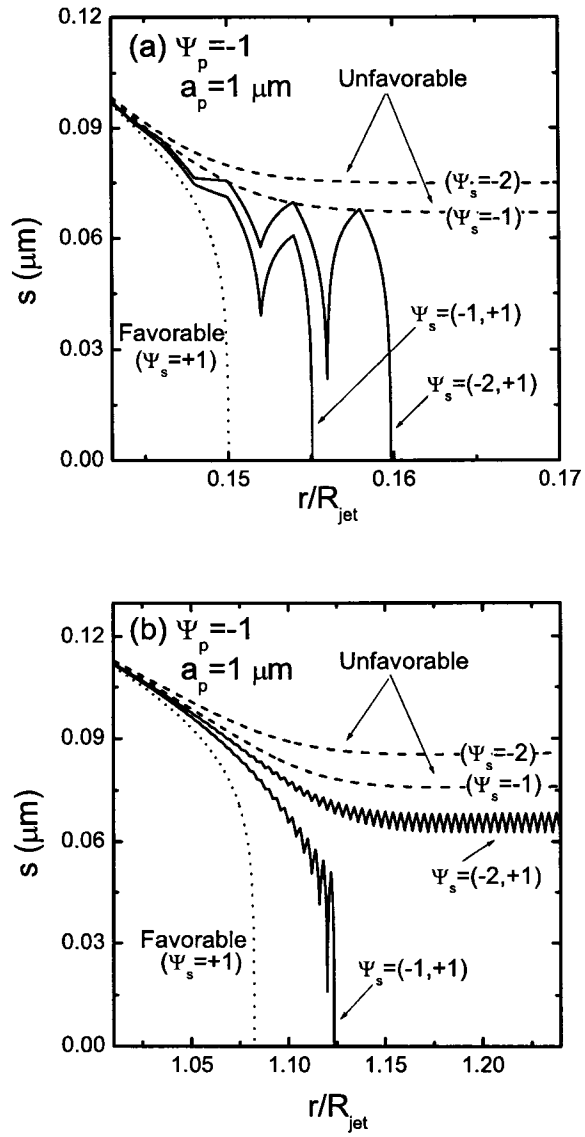

Figure 4.3: Illustration of particle trajectories obtained by numerically solving of Eq. (4.8) for different values of collector surface potentials. Dashed lines represent the particle trajectories over an unfavorable surface. Dotted lines denote particle trajectories over a favorable surface. Solid lines represent the particle trajectories over a heterogeneous charged surface with $w_n = w_p = 2\ \mu m$. The simulations were obtained for two different regions (a) Near Stagnation point and (b) Far from stagnation point.

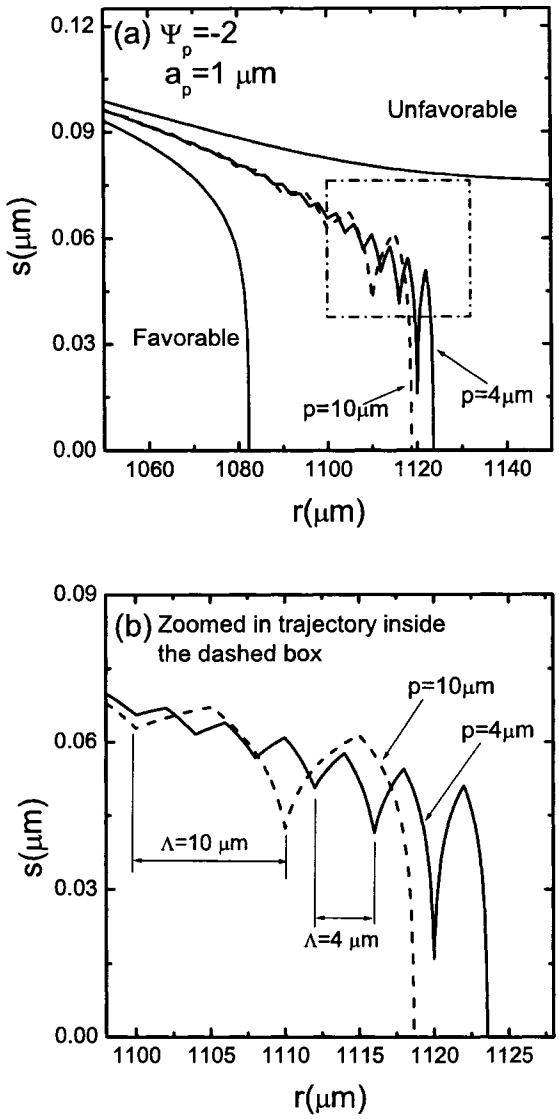

Figure 4.4: (a) Illustration of particle trajectories over a heterogeneous charged surface consists of alternate negative and positive bands with scaled surface potentials of -2 and +2, respectively. (b) Zoomed in trajectories inside the dashed box in Figure 4.4a. Λ represents the wavelength of the oscillating particle trajectory.

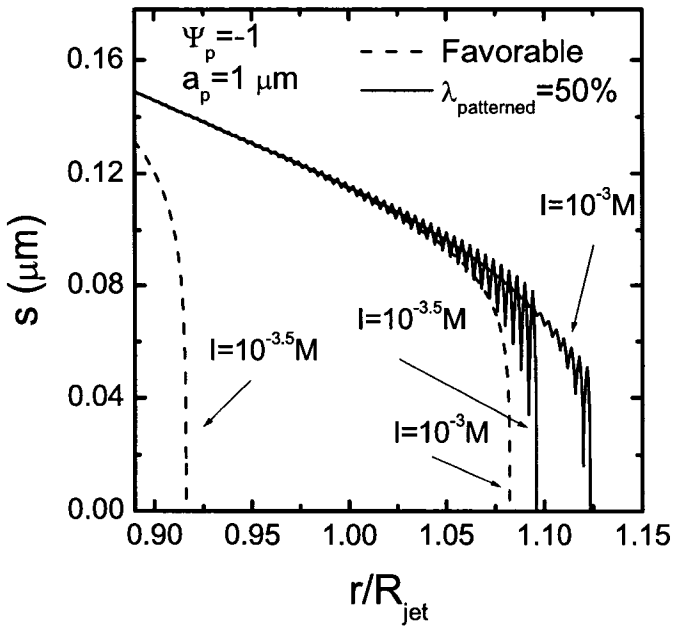

Figure 4.5: Illustration of particle trajectories in impinging jet flow field over a charged substrate for two different values of solution ionic strength i.e. 10^{-3}M and $10^{-3.5}$M. Dashed lines denote the particle trajectories over a homogeneous, fully favorable substrate $\Psi_s = +1$. Solid lines denote particle trajectories over a micropatterned substrate consisting of alternate negative and positive bands, $w_n = w_p = 2\ \mu m$, and $\Psi_s = (-1, +1)$.

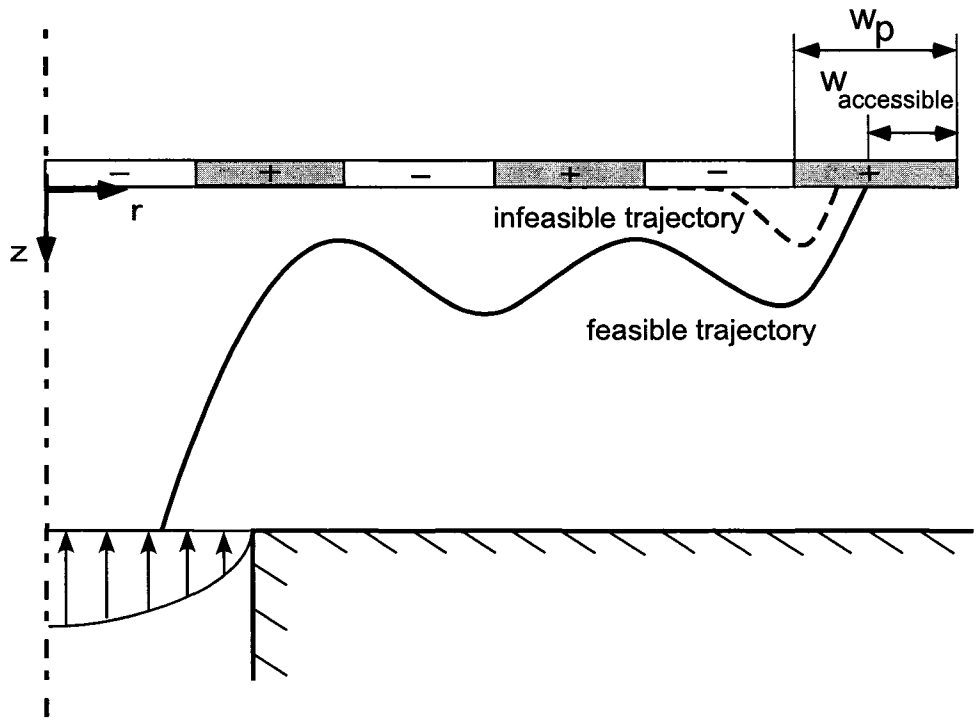

Figure 4.6: A schematic depiction of procedure used to evaluate the inaccessible part at the beginning of favorable stripes. Each favorable stripe was discretized into N segments. Starting from the end of each such segment, the trajectory equations were solved backward to determine the initial release location of the particle. The initial release position was deemed feasible if it originated from within the impinging jet nozzle (solid line). Termination of the trajectory at any other point in the computational domain constituted an infeasible trajectory (dashed line).

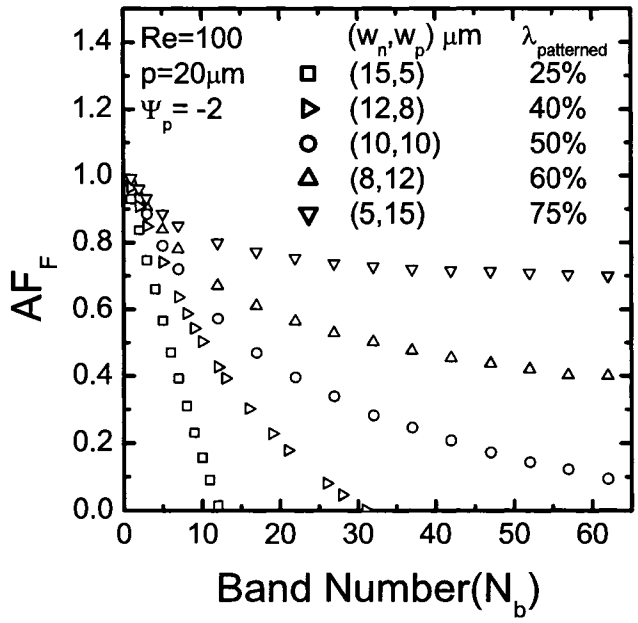

Figure 4.7: Accessible fraction of a favorable band (AF_F) presented for all of the favorable bands on the collector surface. The horizontal axis represents the band number along the radial direction on the collector surface. The results correspond to different values of positive and negative band width while the pitch is maintained constant and equal to 20 μm. $\Psi_s = (-2, +2)$, $a_p = 1$ μm, $I = 10^{-3.5}$M.

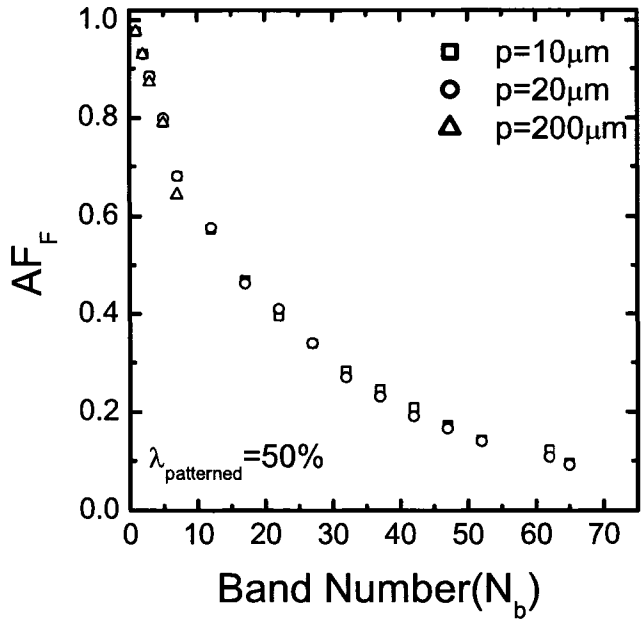

Figure 4.8: Accessible fraction of a favorable band (AF_F) presented for all of the favorable bands on the collector surface for three different values of pitch. The horizontal axis denotes the band number along the radial direction on the collector surface. The favorable area fraction of the collector is maintained constant and equal to 50%. All the other parameters are the same as in Figure 4.7

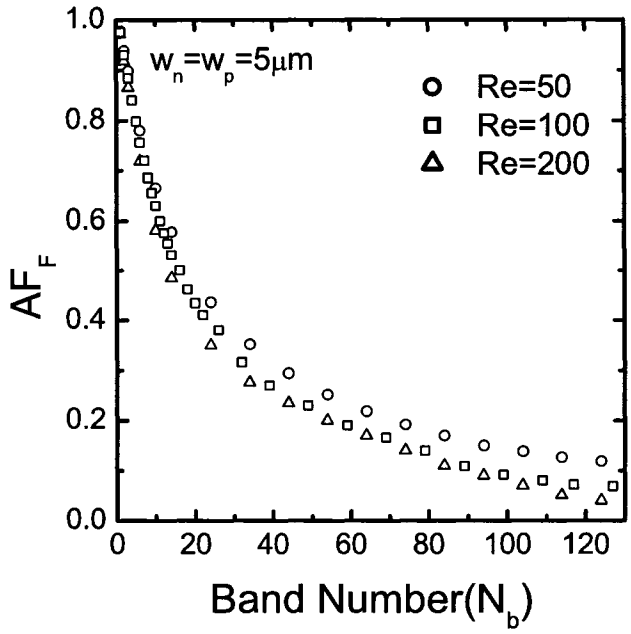

Figure 4.9: Accessible fraction of a favorable band (AF_F) presented for all of the favorable bands on the collector surface for different values of fluid velocity corresponding to Re=50, 100 and 200. The collector surface consists of alternate favorable and unfavorable bands with the width of 5 μm. The favorable are fraction of the collector is 50%. All the other parameters are the same as in Figure 4.7

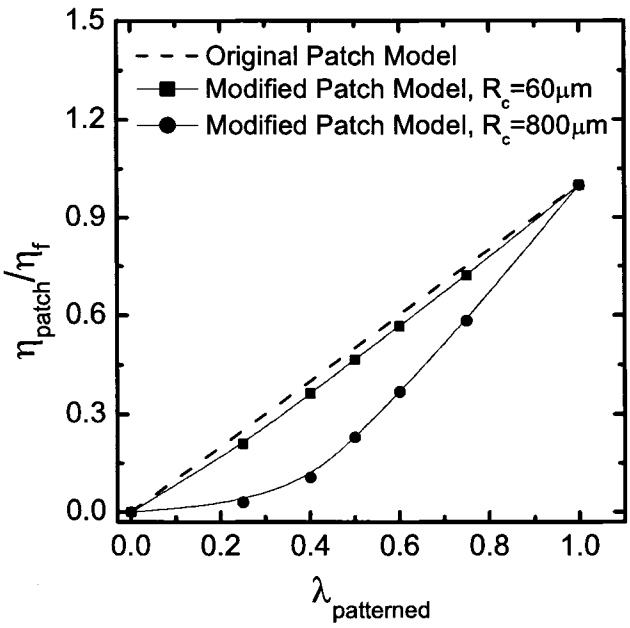

Figure 4.10: The dependence of reduced deposition efficiency (η/η_f) on favorable area fraction of the collector ($\lambda_{patterned}$). Dashed line denoted the effective deposition efficiency obtained using the original patchwise heterogeneity model, Eq. (4.14). Symbol-lines represent the effective deposition efficiency obtained using the modified patchwise heterogeneity model, Eq. (4.17) for two different distances from the stagnation point, $R_c = 60\ \mu m$ (square-legend line) and $R_c = 800\ \mu m$ (circle-legend line). All parameters are the same as in Figure 4.7.

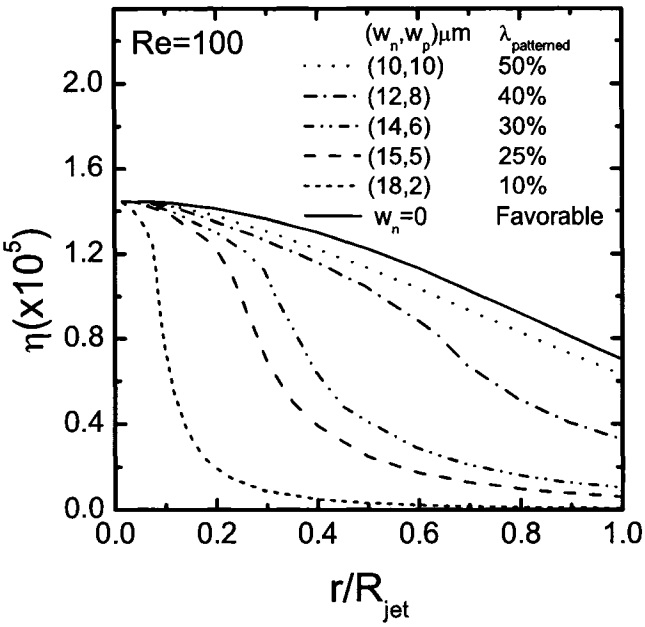

Figure 4.11: The dependence of the collector deposition efficiency (η) on the radial distance from the stagnation point. R_c represents the distance of the end of each favorable band from the stagnation point. Solid line denotes the deposition efficiency for a homogeneous fully favorable collector (η_f), while other lines denote the collector deposition efficiency for a heterogeneous micropatterned collector. All the other parameters are the same as in Figure 4.7.

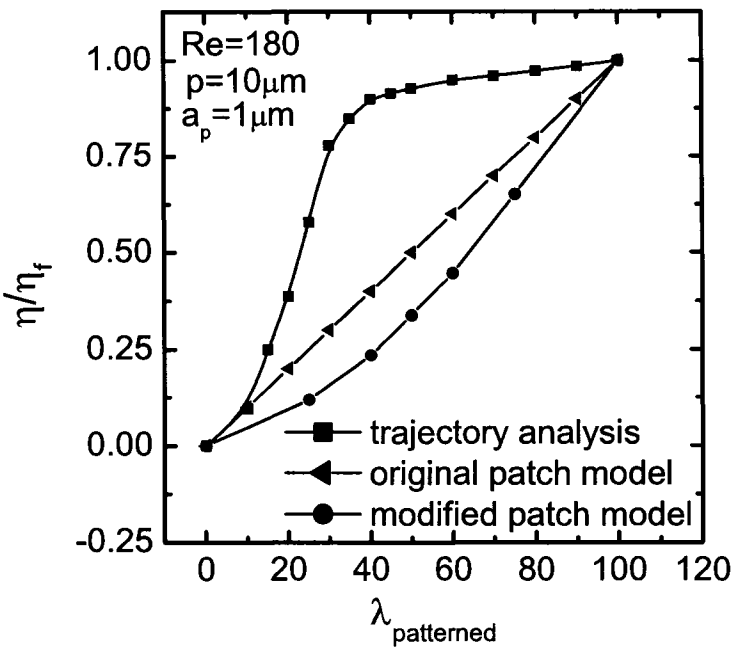

Figure 4.12: The dependence of the scaled collector deposition efficiency (η/η_f) on the collector favorable area fraction. The collector radius, R_c, is assumed to be 300 μm. Triangle-legend line denotes the deposition efficiency for a heterogeneous collector predicted by the original patchwise heterogeneity model while circle-legend line denotes the deposition efficiency for a heterogeneous collector predicted by the modified patchwise heterogeneity model. Square-legend line denotes the deposition efficiency for a heterogeneous collector calculated using trajectory model.

Chapter 5

Eulerian Approach: Particle Transport Equation

5.1 Introduction

In this chapter, we will focus on particle transport modelling from the impinging jet flow onto the solid substrate, using the Eulerian approach. In this model, the effects of convection, diffusion, and migration due to the external forces such as gravity, van der Waals and electrostatic double layer interactions will be included. Using finite element analysis, the convection-diffusion-migration equation with appropriate boundary conditions will be solved numerically for the case of homogeneous and heterogeneous collectors. Utilizing the numerical results for particle concentration, the normal particle flux at the collector surface will be calculated in form of Sherwood number, which represents the dimensionless rate of particle deposition on the collector surface. In order to validate the finite element analysis, the numerical results will be compared with available results in literature for homogeneous collectors. Furthermore, a parametric study are conducted to elucidate the effects of charge heterogeneity on particle deposition on collectors with different favorable area fractions. Finally, the particle deposition rate over heterogeneous collectors obtained by solving the convection-diffusion-migration equation will be compared with that predicted by the patchwise heterogeneity model.

5.2 Convection-Diffusion-Migration Equation

The transfer of particles from a flowing suspension toward a collector surface in an impinging jet system is governed by the general mass conservation equation which has the following form [van de Ven, 1989, Masliyah, 1994]

$$\frac{\partial c}{\partial t} + \vec{\nabla} \cdot \vec{j} = Q \tag{5.1}$$

where c is the particle concentration, $\vec{j}$ is the particle flux and Q is the source term. In this study, it was assumed that the process reaches steady-state condition after a short time, so the time dependent term is set to zero. Furthermore, since there is no mass source or sink in the system (e.g., aggregation of particles) Q takes the value of zero . As a result, the mass conservation equation, Eq. (5.1), simplifies to

$$\vec{\nabla} \cdot \vec{j} = 0 \tag{5.2}$$

The particle flux, $\vec{j}$, is obtained by considering contributions from fluid convection, diffusion, and migration due to the external forces exerted on the particle. Considering all of the above contributions, the particle flux can be defined as [van de Ven, 1989, Masliyah, 1994]

$$\vec{j} = \vec{v}c - \underline{\underline{D}} \cdot \vec{\nabla} c + \frac{c}{k_b T} \underline{\underline{D}} \cdot \vec{F} \tag{5.3}$$

where $\vec{v}$ is the particle velocity, $\underline{\underline{D}}$ is the diffusion coefficient tensor, k_b is the Boltzmann constant, T is the absolute temperature and $\vec{F}$ is the total force exerted on the particle. In order to solve the convection-diffusion-migration equation, Eq. (5.2), particle velocity, diffusion tensor, and the total external forces should be defined.

The fluid velocity field inside the impinging jet system was obtained in chapter 2 from a solution of Navier-Stokes and continuity equations. In the vicinity of the collector surface, the velocity of the particle induced by fluid motion is different from that of the fluid due to the effect of hydrodynamic interactions. Following Spielman and Fitzpatrick [Spielman and Fitzpatrick, 1973], the rela-

tionship between the fluid and particle velocities is given by

$$v_r = u_r f_3(h) \tag{5.4a}$$

$$v_z = u_z f_1(h) f_2(h) \tag{5.4b}$$

where $f_1(h)$ to $f_3(h)$ are the universal hydrodynamic correction functions and h is the dimensionless surface to surface distance between the particle and the substrate.

The expressions for total external forces acting on the particle were provided in Chapter 3. In the next subsection, we define the particle diffusion tensor. It is worth noting here that due to the geometry of the impinging jet flow system used in this study, the mass transfer equation can be solved based on an axisymmetric two-dimensional cylindrical coordinate system which is identical to the one used for solving the fluid flow equations in Chapter 2.

5.2.1 Particle Diffusion Coefficient

It can be seen from Eq.(5.3) that we employed the diffusion coefficient tensor instead of simple scalar diffusion coefficient given by the Stokes-Einstein equation, i.e., $D_\infty = k_b T / 6\pi\mu_f a_p$. The reason for introducing this tensor is as follows; near the collector surface, the particle diffusion coefficient is affected by hydrodynamic interactions and becomes dependent on the position of the particle relative to the collector surface [van de Ven, 1989, Honig *et al.*, 1971]. Assuming a dilute suspension of spherical, non-interacting particles, the particle diffusion coefficient can be formulated as

$$\underline{\underline{D}} = D_\infty \begin{bmatrix} d\,\| & 0 \\ 0 & d\,\perp \end{bmatrix} \tag{5.5}$$

where D_∞ is the particle diffusion coefficient in the bulk solution given by the Stokes-Einstein equation. $d\,\|$ and $d\,\perp$ are the correction factors due to the finite gap between the particle and the collector surface. Considering the geometry of the system, we can define $D_\infty d\,\|$ and $D_\infty d\,\perp$ as being D_{rr} and D_{zz} which

can be formulated by incorporating the effects of hydrodynamic interactions as follows

$$\underline{\underline{D}} = \begin{bmatrix} D_{rr} & 0 \\ 0 & D_{zz} \end{bmatrix} = D_\infty \begin{bmatrix} f_4(h) & 0 \\ 0 & f_1(h) \end{bmatrix} \tag{5.6}$$

where f_1 and f_4 are the universal hydrodynamic correction functions [Goldman *et al.*, 1967*b*], and h is the dimensionless surface to surface distance between the particle and the substrate (s/a_p). The expressions for the universal hydrodynamic correction functions were taken from Masliyah (1994).

5.3 Particle Transport Equation

In the absence of the source term in the mass conservation equation and by assuming the steady-state process, the transport of the particles inside the impinging jet system can be formulated using Eq. (5.2), where the particle flux given by Eq. (5.3) can be written explicitly in an axisymmetric two dimensional cylindrical coordinate system as

$$j_r = v_r c - (D_{rr}\frac{\partial c}{\partial r} + D_{rz}\frac{\partial c}{\partial z}) + \frac{c}{k_b T}(D_{rr}F_r + D_{rz}F_z) \tag{5.7a}$$

$$j_z = v_z c - (D_{zr}\frac{\partial c}{\partial r} + D_{zz}\frac{\partial c}{\partial z}) + \frac{c}{k_b T}(D_{zr}F_r + D_{zz}F_z) \tag{5.7b}$$

where j_r and j_z are the particle flux in radial and normal directions. F_r and F_z are the total external forces acting on the particle in radial and normal directions, respectively. The above equations can be further modified by using the equation for particle velocity, Eq. (5.4), and the expression for particle diffusion coefficient, Eq. (5.6).

$$j_r = u_r f_3 c - D_\infty f_4 \frac{\partial c}{\partial r} + \frac{c}{k_b T} D_\infty f_4 F_r \tag{5.8a}$$

$$j_z = u_z f_1 f_2 c - D_\infty f_1 \frac{\partial c}{\partial z} + \frac{c}{k_b T} D_\infty f_1 F_z \tag{5.8b}$$

As described earlier in Chapter 3, in this study we consider gravity, van der Waals, and electrostatic double layer interaction the forces exerted on the particle in an impinging jet system. As a result, F_r and F_z can be defined as

$$F_r = 0 \tag{5.9a}$$

$$F_z = F_g + F_{vdw} + F_{edl} \tag{5.9b}$$

It is worth noting here that the only radial force exerted on the particle is due to the hydrodynamic drag force. However, since we already take this force into account as convection term in the expression for particle flux, Eq. (5.3), there are no other radial forces exerted on the particle implying that F_r takes the value of zero in Eq.(5.9).

The particle transport equation can be nondimensionalized by multiplying Eqs. (5.2) and (5.8) with $a_p/D_\infty c_\infty$, which results in

$$\vec{\nabla}.\vec{\bar{j}} = \frac{1}{\bar{r}}\frac{\partial}{\partial \bar{r}}(\bar{r}\bar{j}_r) + \frac{\partial \bar{j}_z}{\partial \bar{z}} = 0 \tag{5.10a}$$

$$\bar{j}_r = \bar{u}_r f_3 Pe\ \bar{c} - f_4 \frac{\partial \bar{c}}{\partial \bar{r}} \tag{5.10b}$$

$$\bar{j}_z = \bar{u}_z f_1 f_2 Pe\ \bar{c} - f_1 \frac{\partial \bar{c}}{\partial \bar{z}} + f_1 \bar{F}_z \bar{c} \tag{5.10c}$$

where

$$\bar{u_r} = \frac{u_r}{U_\infty} \qquad \bar{r} = \frac{r}{a_p} \qquad \bar{F_z} = \frac{F_z a_p}{k_b T} \qquad \bar{c} = \frac{c}{c_\infty}$$

$$\bar{u_z} = \frac{u_z}{U_\infty} \qquad \bar{z} = \frac{z}{a_p} \qquad \bar{j} = \frac{j a_p}{D_\infty c_\infty} \qquad Pe = \frac{U_\infty a_p}{D_\infty}$$

Eq. (5.10) is the nondimesionalized convection-diffusion-migration equation that governs the particle transport inside the impinging jet system or any other axisymmetric configuration in the presence of external forces. Eq. (5.10) is a second order, parabolic differential equation that can be solved numerically. The boundary conditions related to the convection-diffusion equation are described in the next section.

5.4 Computational Domain and Boundary Conditions

In order to solve the convection-diffusion equation, Eq. (5.10), in the impinging jet flow system, the appropriate boundary conditions should be defined first. The computational geometry is depicted in Figure 5.1. As described earlier in Chapter 2, a colloidal suspension containing particles impinges vertically on the collector surface (OG, hatched line). The simulation is based on the axisymmetric cylindrical coordinate system where the center of the coordinate system is located at the stagnation point, O. The computational domain used in numerical simulation is depicted by the rectangular region in dashed lines in Figure 5.1a. Figure 5.1b shows this domain in more details. Here, O is the stagnation point and represents the center of cylindrical coordinate system. OG represents the collector surface. The radius of the collector is assumed to be 1 mm and equal to the radius of the impinging jet nozzle. All the lengths are nondimensionalized with respect to the particle radius, a_p.

It is extensively stated in the literature [Prieve and Ruckenst.E, 1974, Spielman and Fitzpatrick, 1973, Adamczyk, 1989, Elimelech, 1995, Masliyah, 1994], that the particle deposition over a surface occurs when the center of the particle reaches a certain distance, $z = a_p + \delta_m$, from the substrate (where z is the normal distance between the particle center and collector surface). The separation distance, δ_m, is usually taken as an arbitrary cut-off separation distance located typically around 1-5 nm from the collector surface. Use of this finite value for the separation distance eliminates the problems due to the divergence of van der Waals forces at contact. In our computational domain, we define a line, HJ, at the distance of $z = a_p + \delta_m$ from the collector surface. This line, forming one of the computational boundaries, represents the location where the particle deposition can occur. The boundary condition along this line is the well-known "perfect sink" boundary condition. This condition implies that when the center of the particle reaches this line, the particle will be irreversibly captured by the

collector surface. The captured particle is no longer part of the dispersed phase implying that the particle concentration is zero along HJ.

The other computational boundary depicted in Figure 5.1b is EH. This line is located along the z axis and represents the symmetry line. It was assumed that the value of radial particle flux is zero which means that the particle flux vector consists of just normal component along this line. The length of EH is assumed to be 50 μm.

EF is parallel to the collector surface and located at the distance from the collector where the assumption of bulk concentration is valid. This assumption implies that at large distances from the collector surface, the particle concentration is equal to the particle concentration in bulk phase. As suggested in literature [Adamczyk, 1989], for micron-sized particles, the diffusion boundary layer thickness is of order of 1 to 10 μm. This means that the distance of 50 μm from the collector surface is sufficiently large for the assumption of bulk concentration to be valid along EF.

FJ is parallel to z axis and represents the outlet part of the computational domain. It is assumed that in the vicinity of the collector surface, the particle concentration gradient in radial direction is significantly smaller than the particle concentration gradient in normal direction [Adamczyk *et al.*, 1986, Masliyah, 1994]. This allows one to neglect the variation of particle concentration with respect to r compared to the variation of particle concentration with respect to z along FG. Consequently, since the diffusion term in the convection-diffusion equation is directly proportional to the concentration gradient, the dominant mechanisms of particle transport across FG are convection and migration. This means that any mass flux due to diffusion across this boundary is approximately zero. This condition is useful for convection dominated mass balances where the outlet concentration is unknown.

Overall, inside the computational domain of EFJH, we can summarize the above boundary conditions that the convection-diffusion equation, Eq. (5.10),

is subjected to as

$$\bar{c} = 0 \qquad \partial\Omega \in HJ \tag{5.11a}$$

$$\vec{n} \cdot \vec{\bar{j}} = 0 \qquad \partial\Omega \in EH \tag{5.11b}$$

$$\bar{c} = 1 \qquad \partial\Omega \in EF \tag{5.11c}$$

$$\vec{n} \cdot \nabla\bar{c} = 0 \qquad \partial\Omega \in FJ \tag{5.11d}$$

where $\vec{n}$ represents the unit vector, normal to the surface.

5.5 Particle Deposition Rate

Transport equations such as Eq. (5.10) provide the particle concentration distribution everywhere inside the domain of interest. The particle concentration distribution can be employed to obtain the particle deposition rate on the collector surface. The particle deposition rate in context of Eulerian approach be represented by the Sherwood number, which is defined as

$$Sh = \frac{a_p}{D_\infty c_\infty}(j_\perp)_{z=a_p+\delta_m} = (\bar{j_z})_{z=a_p+\delta_m} \tag{5.12}$$

here, $(\bar{j_z})$ is the dimensionless normal particle flux on the collector surface, evaluated at $z = a_p + \delta_m$, where δ_m is an arbitrary cut-off distance typically located around 1-5 nm from the collector surface. Once the convection-diffusion equation is solved, $(\bar{j_z})$ on the collector surface can be calculated using Eq. (5.8). The Sherwood number given by Eq. (5.12) is the local Sherwood number at a given radial position on the collector surface. The average Sherwood number over the whole collector surface can be expressed as

$$Sh_{ave} = \frac{1}{S}\int_S Sh\, dS \tag{5.13}$$

where S is the collector surface area. Considering the geometry of the impinging jet system, the above equation can be further simplified in cylindrical coordinate system as

$$Sh_{ave} = \frac{1}{\pi(r_2^2 - r_1^2)}\int_{r_1}^{r_2} Sh(r)(2\pi r)\, dr = \frac{2}{(r_2^2 - r_1^2)}\int_{r_1}^{r_2} rSh(r)\, dr \tag{5.14}$$

where Sh_{ave} represents the overall particle deposition over the collector with the surface area of $\pi(r_2^2 - r_1^2)$. Here, r_1 and r_2 are the radia of the circular segment on the collector surface.

5.6 Numerical Method

5.6.1 Numerical Simulation Using FEMLAB®

The numerical solution of convection-diffusion equation, Eq. (5.10) along with boundary conditions, Eq. (5.11) is obtained using finite element analysis. The solution methodology in this study was implemented using the commercially available software FEMLAB® 3.1 (COMSOL, Inc., USA). FEMLAB® provides a number of application modes or modules that consist of predefined templates and user interfaces already set up with equations and variables for different areas of physics such as electromagnetics, structural mechanics, chemical engineering, and so forth. The chemical engineering module is a package optimized for the analysis of transport phenomena. The predefined convection-diffusion equation in chemical engineering module of FEMLAB® has the following format

$$\frac{\partial c}{\partial t} + \vec{\nabla} \cdot (\vec{v}c - \underline{\underline{D}} \cdot \vec{\nabla}c) = Q \tag{5.15}$$

As can be seen from Eq. (5.15), in modelling the particle transport, the convection and diffusion application mode of FEMLAB® considers only the effects of convection and diffusion whereas in our model, due to the presence of external forces acting on the particle, the migration term also contributes significantly in particle transport phenomena. In order to use the predefined mass transfer expression of FEMLAB® for our study, we rewrite the equation for particle flux, Eq. (5.3), such that the convection and migration term are lumped together yielding

$$\vec{j} = (\vec{v} + \frac{1}{k_b T}\underline{\underline{D}} \cdot \vec{F})c - \underline{\underline{D}} \cdot \vec{\nabla}c \tag{5.16}$$

Here, the first parenthesis represents the coupled effects of convection and migration due to the hydrodynamic effects and external forces. The second term inside the parenthesis also has the dimension of velocity, which allows one to consider the entire term in parenthesis as the total particle velocity that has contributions from the hydrodynamic effects, v, and external forces, $\frac{1}{k_bT}\underline{\underline{D}} \cdot \vec{F}$. In this manner, we change the convection-diffusion-migration equation to the convection-diffusion form by preserving the effects of migration inside the convection term, which allows us to use the predefined expressions of FEMLAB® for solving the particle transport equation.

In modelling mass balances in the convection and diffusion application mode of the Chemical Engineering Module of FEMLAB®, there are two mass balance formulations available; a conservative and non-conservative formulation. The conservative or general formulation is given by Eq. (5.15). The non-conservative formulation removes the convective term from the divergence operator by taking into account the continuity equation, (i.e., $\nabla \cdot (\rho v) = 0$). Although this format imparts greater stability to the system, is not applicable in our model since the convection term consists of both the hydrodynamic velocity and the velocity induced by external forces. Consequently, in our model we select the general or conservative equation form.

The available boundary conditions in the convection-diffusion application mode of FEMLAB® support all of the boundary conditions in Eq. (5.11) which allows the implementation of the exact boundary conditions without any modifications.

5.6.2 Mesh Generation

So far, the equations governing the particle transport phenomena along with the appropriate boundary conditions inside the computational geometry have been defined. The appropriate application mode for solving this equation is selected from those available in FEMLAB software. The next step in solving the convection-diffusion equation using finite element analysis is mesh generation.

The computational domain is descretized using quadrilateral mesh. Lagrangian elements of second order are employed that accelerate the numerical convergence. The scope of using triangular mesh with same type of mesh distribution has also been explored. It was observed that a higher accuracy can be obtained by employing the quadrilateral mesh rather than triangular mesh. Quadrilateral elements divided the domain to a series of smaller rectangular regions where rows and columns of elements can be generated. By manually choosing the number of subdivisions on the boundaries of computational domain, one can have an absolute control over the mesh density every where inside the computational domain. By taking advantage of this flexibility, the mesh density is increased in the vicinity of the collector surface to account for high concentration gradients in these regions.

In a finite element analysis, a small mesh size is necessary for the regions of high concentration gradients, i.e. regions where large variation of concentration with respect to small distances occurs. Since colloidal interactions are short range forces, in the vicinity of the collector surface a significant particle concentration gradient has been observed [Ruckenstein and Prieve, 1973, Spielman and Fitzpatrick, 1973]. This gradient is even larger for the case of particles over unfavorable collectors since a large number of particles accumulates in a narrow region at the secondary minimum, forming a sharp concentration peak there. This behaviour necessitates the use of significantly small elements with length scales even smaller than Debye length close to the surface [Song *et al.*, 1994]. Having the same element size far from collector surface will be redundant because the concentration gradient is small in those regions and is less affected by the choice of element size.

In order to obtain the necessary number of elements that is required to solve the convection-diffusion equation for the case of homogeneous, fully favorable collector, several simulations with different numbers of elements were conducted. It was observed that increasing the element number above 20,000 does not affect the particle concentration in the computational domain. However, in case

of homogeneous unfavorable collector, using this number of elements results in negative concentration value in the vicinity of the collector which is obviously erroneous. It turns out that in order to minimize the value of this negative concentration and obtain a smooth solution, the number of element should be increased significantly. This high value of mesh density increases the computational load.

For the case of heterogeneous collectors consisting of alternate favorable and unfavorable bands, the sufficient number of elements is even higher than the unfavorable collector. For a heterogeneous collector, the electrostatic double layer force changes its sign over the consecutive bands. This will cause large variations of concentration with respect to r near the edges of each band. This means that for heterogeneous collectors, in addition to small element size near the collector surface, the high mesh density is also required for the regions where the surface potential changes its sign. This increases the computational loads significantly. In order to overcome this problem, the following procedure in solution methodology was adopted.

5.6.3 Numerical procedure: Multi-Geometry Method

The convection-diffusion equation, Eq. (5.10), along with the appropriate boundary conditions, Eq. (5.11), inside the computational domain depicted in Figure 5.1b has been solved using finite element analysis and FEMLAB® software according to the procedure explained in Section 5.6.1. The computational domain is descretized into 20,000 elements with increasing mesh density near the collector surface. Once the particle concentration is computed inside the domain EFJH, we define another computational domain within EFJH represented by HJKL in Figure 5.1b. In Figure 5.1b, KL is a line parallel to the collector surface inside the domain EFJH with the distance of $z = 3\ \mu m$ from the collector surface. Solving the convection-diffusion equation inside EFJH provides the particle concentration along the line KL. Now the same convection-diffusion equation can be solved inside the smaller domain HJKL, where the boundary

condition along the line KL is defined as a Dirichlet condition using the results for particle concentration computed for EFJH, while all the other boundary conditions are the same as those defined in Eq. (5.11). Shrinking the computational domain from EFJH to HJKL allows redefining the resolution of the geometry near the collector surface.

In choosing the second computational domain, we have to optimize the distance of KL from the collector surface. Since the element size near the collector in the first domain, EFJH is not sufficiently small, the numerical solution of particle concentration in this region has some error and provides negative values for particle concentration, which is erroneous. As a result, KL should be far enough from the collector (i.e., where the concentration gradient is still small) that the concentration along this line is not affected by the choice of element size close to the collector surface. On the other hand, since the whole purpose of creating the second computational domain is to reduce the computational load by decreasing the size of the computational geometry, the distance of KL from the collector surface should be reasonably small. To find this optimized distance, the simulation was carried out for different values of element number ranging from 20,000 to 30,000 inside the domain EFJH. For each simulation, the particle concentration is recorded along four different lines with distances of 0.5, 1, 2, 3 and 4 μm from the collector surface. It was observed that the line with the distance of 3 μm from the collector is the closest line to the collector that the particle concentration along this line is not affected by the choice of element number. The particle concentration along other lines, with distances of 0.5, 1, and 2 μm from the collector surface, is sensitive to the element number inside the larger computational domain.

The process of solving the same set of equations inside two different geometries employed in our simulation can be categorized as a part of the general "Multi-grid Methods" in numerical simulations. The multi-geometry environment of FEMLAB® allows us to create two geometries. Once the convection-diffusion equation is solved inside the larger geometry (EFJH), using the "ex-

trusion coupling variables", we can transfer the obtained concentration, $\bar{c}$, along the line KL to the smaller geometry (KLJH) as the Dirichlet boundary condition for its upper boundary. Using this method, we could minimize memory consumption and accelerate the solution time significantly. Further details about using extrusion coupling variables can be found in FEMLAB® user's guide.

In solving the convection-diffusion equation using finite element analysis, for both geometries, the non-linear stationary solver was selected. Initial solution of the assembled matrix equation is achieved using Gauss elimination. The relative tolerance and maximum number of iteration are set to 10^{-6} and 25, respectively. The relative tolerance gives the criterion for convergence. Once the relative error is less than the relative tolerance, the software stops iterating and the solution is complete.

5.7 Validation of Numerical Results

In order to investigate the accuracy of finite element calculations, the numerical results are compared with those available in literature. In this section we make use of three available studies in literature to validate our numerical results.

5.7.1 Diffusion Dominant Deposition (Levich Equation)

Available studies in literature mainly deal with the problem of convection-diffusion equation inside the stagnation point region where the analytical expression for fluid velocity, Eq. (2.6), is valid. Incorporating these expressions in the convection-diffusion-migration equation, one can simplify Eq. (5.10) to

$$\vec{\nabla}.\vec{\bar{j}} = \frac{1}{\bar{r}}\frac{\partial}{\partial \bar{r}}(\bar{r}\bar{j}_r) + \frac{\partial \bar{j}_z}{\partial \bar{z}} = 0 \tag{5.17a}$$

$$\bar{j}_r = \frac{1}{2} f_3 Pe_s\ \bar{r}\bar{z}\bar{c} - f_4 \frac{\partial \bar{c}}{\partial \bar{r}} \tag{5.17b}$$

$$\bar{j}_z = -\frac{1}{2} f_1 f_2 Pe_s\ \bar{z}^2\bar{c} - f_1 \frac{\partial \bar{c}}{\partial \bar{z}} + f_1 \bar{F}_z \bar{c} \tag{5.17c}$$

where Pe_s = is the stagnation flow Peclet number defined as

$$Pe_s = \frac{2\alpha_s a_p^3}{D_\infty} \tag{5.18}$$

where α_s is defined in Eq. (2.7).

Under certain assumptions, there are few limiting analytical solutions for convection-diffusion-migration equation, Eq. (5.17), in the stagnation point region. These solutions can be used as criteria to examine the validity of the numerical results. One of these limiting cases where the analytical solution for convection-diffusion equation is available for stagnation point region, was given by Levich [Levich, 1962]. Several assumptions were made to obtain the analytical solutions, which are; (a) the energy barrier (unfavorable deposition) is absent. (b) neither hydrodynamic interactions nor colloidal surface interactions are involved, i.e., $f_1(h) = f_2(h) = f_3(h) = 1$ and $\bar{F}_{vdw} = \bar{F}_{edl} = 0$ which in practice may correspond to the situation where the hydrodynamic resistance interactions are counterbalanced by attractive colloidal interactions. (c) all the radial derivatives in Eq. (5.17) are several orders of magnitude smaller than the normal derivatives inside the stagnation point region and therefore, are negligible. Considering all of the assumptions and assuming the stagnation point flow equations are valid, the convection-diffusion equation inside the stagnation point region, Eq. (5.17), can be simplified to

$$\frac{d^2\bar{c}}{d\bar{z}^2} + \frac{1}{2}\bar{z}^2 Pe_s \frac{d\bar{c}}{d\bar{z}} = 0 \tag{5.19}$$

which is a second order ordinary differential equation. The boundary conditions for this equation are

$$\bar{c} = 0 \qquad \bar{z} = 1 + \bar{\delta}_m \tag{5.20a}$$

$$\bar{c} = 1 \qquad \bar{z} \to \infty \tag{5.20b}$$

Integrating Eq. (5.19) twice and making use of the boundary conditions, Eq. (5.20), one can obtain an analytical expression for particle concentration from which the Sherwood number can be calculated according to Eq. (5.12).

For diffusion controlled deposition i.e., $Pe_s << 1$, the analytical expression for Sherwood number takes the form of [Levich, 1962]

$$Sh = 0.616 Pe_s^{1/3} \tag{5.21}$$

It follows that in diffusion dominated regime and in the absence of energy barriers and force fields, the dimensionless particle deposition rate is governed by the Levich formula given by Eq. (5.21).

The numerical model is first tested by computing Sh in the stagnation point region in absence of energy barriers where all the other parameters are as stated in Table 3.1. The dependence of the Sherwood number, Sh, on stagnation Peclet number, Pe_s, Eq. (5.21) is depicted in Figure 5.2. In this figure, symbols represent the Sh obtained using the numerical solution of convection-diffusion-migration equation. For each value of Pe_s, the convection-diffusion-migration equation, Eq. (5.17) along with the boundary conditions Eq. (5.20) was solved using finite element analysis and methodology described in Section 5.6.1. Once the particle concentration profile was obtained, the local Sherwood number was calculated using Eq. (5.12). The average particle deposition rate, represented by Sh_{ave} inside stagnation region can be calculated by setting the limits of integration in Eq. (5.13), r_1 and r_2, such that they represent the regions inside the stagnation point area. As mentioned in Chapter 2, in this study, we assume that the stagnation point region is located in the domain represented radially by $0 < r < 100\ \mu m$. Using the values of $r_1 = 0$ and $r_2 = 100\ \mu m$, the overall particle deposition in stagnation point region can be obtained in the form of Sh_{ave}.

The solid line in Figure 5.2 represents the Sherwood number obtained using Levich equation, Eq. (5.21). As shown in this figure, in the diffusion dominated regime, $Pe_s \ll 1$, there is an excellent agreement between the Sh_{ave} obtained using numerical method (symbols) and Sh_{ave} predicted by Levich equation (solid line) implying the finite element method used in the present study accurately calculates the particle deposition rate. At larger values of $Pe_s > 1$, the Sh_{ave} obtained using the numerical method deviates from that predicted by Levich.

5.7.2 Unfavorable Deposition

Calculating rate of particle deposition by numerically solving the convection-diffusion equation is particularly difficult when repulsive colloidal interactions are involved [Song *et al.*, 1994]. In the presence of repulsive interaction, the particles accumulate in a narrow region located at a finite distance from the collector surface, around the secondary minimum and form a sharp concentration peak that changes the nature of convection-diffusion equation into stiff equations with turning points. Solving this type of equation smoothly requires special precautions in mesh generation. Thus, if the finite element analysis employed in this study manages to produce reasonable results for particle deposition over unfavorable collectors, it implies the validity of the present numerical method.

Dabros and van de Ven [Dabros and van de Ven, 1983] presented numerous results for particle deposition under different conditions. One of these results is for numerically calculated particle deposition rate over an unfavorable collector. In the second test for the finite element solution, we compare our numerical results with those reported by Dabros and van de Ven for the case of unfavorable deposition. The comparison is presented in Figure 5.3.

Figure 5.3 shows the variation of particle deposition rate, presented as Sh_{ave} with respect to flow Reynolds number, Re for different values of Dl inside the stagnation point region. Solid lines in this graph show the Sh_{ave} reported by Dabros and van de Ven. Dashed lines represent the Sh_{ave} obtained by finite element analysis. For each value of double layer parameter, Dl, numerical calculation was performed for different values of Re. Once the particle concentration profile was obtained, the overall Sh_{ave} for the stagnation point region was obtained using the procedure described in Section 5.7.1. All the parameters are exactly the same as those used in the calculations of Dabros and van de Ven [Dabros and van de Ven, 1983]. Figure 5.3 depicts an excellent agreement between Sh_{ave} obtained using finite element analysis and those reported by Dabros and van de Ven which implies the validity of the present numerical model.

5.7.3 Variation of Particle Deposition with Particle Size

In computing the particle deposition rate, one of the advantages of using Eulerian approach (convection-diffusion equation) over Lagrangian approach (trajectory analysis) is that, Eulerian approach applies to all particle sizes whereas Lagrangian approach can be used for non-Brownian particles due to the mathematical complexities of incorporating diffusion effects in trajectory analysis [Adamczyk, 1989, Elimelech, 1995]. Taking advantage of this property of Eulerian approach, we calculate particle deposition rate as Sh_{ave} for different values of particle radius, a_p, ranging from 0.01 to 2 μm.

In Figure 5.4, the vertical axis represents particle deposition efficiency, η. It is worth noting here that Sh_{ave} and η both represent particle deposition rate. Sh_{ave} is normally used to represent particle deposition rate in Eulerian approach while η is normally used to represent particle deposition rate in Lagrangian approach. Using the definitions of Sh_{ave}, Eq. (5.13), and η, Eq. (4.10), one can relate Sh_{ave} and η as [Masliyah, 1994]

$$Sh_{ave} = \eta \; Pe \tag{5.22}$$

where $Pe = \frac{U_\infty a_p}{D_\infty}$.

The solid line with circular symbols in Figure 5.4 denotes the η obtained by finite element analysis. These results are obtained by solving the convection-diffusion equation numerically for different particle radii. Once the particle concentration profile is obtained, one can calculate Sh_{ave} using Eq. (5.13). Following this, by making use of Eq. (5.22), the η corresponding to each Sh_{ave} was calculated. Figure 5.4 depicts the variation of particle deposition efficiency, η, with particle radius, a_p, for a homogeneous, fully favorable collector with scaled surface potential $\Psi_s = +1$. The particle scaled surface potential is assumed to be -1. The flow Reynolds number and solution ionic strength are 100 and 10^{-3}, respectively. All the other parameters are stated in Table 3.1.

The numerically calculated values of particle deposition efficiency, η, in Figure 5.4 shows the same qualitative behaviour with respect to particle size as

reported in literature [Rajagopalan and Kim, 1981, Tufenkji *et al.*, 2004, Nelson and Ginn, 2005]. Moreover, using Levich equation, Eq. (5.21), and the relation between Sh_{ave} and η, Eq. (5.22), we calculate the particle deposition rate, η, predicted by Levich equation for different values of particle radius. The results have been shown in Figure 5.4 as a dashed line. It can be seen that for smaller particle size, which corresponds to smaller values of Pe, the numerically calculated η is in excellent agreement with the η predicted by Levich equation.

Overall, it was observed that the numerical technique used to obtain the solution of convection-diffusion equation provides accurate results for particle concentration distribution and particle deposition rate. Hence, it can be employed to predict the particle deposition rate over different collectors with different surface potentials.

5.8 Numerical Results for Particle Deposition: Homogeneous Collectors

Although the goal of this study is to investigate the role of charge heterogeneity on particle deposition, we first present some results concerning particle deposition over homogeneous collectors. This will give us an insight regarding the physics governing the development of the particle concentration profile and the particle deposition behaviour over different collectors in the presence of external forces.

Particle deposition over homogeneously charged collectors in the impinging jet system has received enormous attention in literature. The effects of different parameters such as solution ionic strength, particle size, fluid velocity, *etc.*, on particle deposition have been extensively studied [Adamczyk, 1989, van de Ven, 1989, Masliyah, 1994]. In order to study to what extent the charge heterogeneity affects the deposition rate, we need to first calculate particle deposition rates over homogeneous collectors. Moreover, solving the convection-diffusion equation for the case of particle transport over homogeneous collectors enables

us to observe the particle concentration profile (particle distribution) in the vicinity of the collector surface. Figure 5.5 depicts the variation of dimensionless particle concentration with the vertical distance from the collector surface, z, at the stagnation point. The particle radius is 1 μm and the flow Reynolds number is 100. The solution ionic strength is 10^{-3}M. All the other parameters are stated in Table 3.1. This set of results is obtained by solving the convection-diffusion equation, Eq. (5.10) along with the boundary conditions, Eq. (5.11) using the finite element analysis and procedure explained in Section 5.6.

The solid line in Figure 5.5 depicts the concentration profile with respect to z for a homogeneous, fully favorable collector where the particle and collector scaled surface potentials are assumed to be -1 and +1 respectively. The dashed line represents the particle concentration profile with respect to z for a homogeneous, fully unfavorable collector where the particle and collector scaled surface potentials are both equal to -1. A comparison between these two profiles reveals that far from the collector surface, the particle concentration approaches the bulk concentration for both favorable and unfavorable collectors. However, from a certain vertical distance from the collector surface, $s \approx 100\ nm$, particles start to experience colloidal forces and the concentration profile over favorable and unfavorable collectors show different behaviours.

In the case of favorable collector, due to the hydrodynamic retardation effects (wall effects) which slow down particle velocity toward the collector, particle concentration increases initially as the particle-collector vertical distance is reduced. By further decreasing the particle-collector vertical distance, due to attractive electrostatic double layer force, the particle velocity toward the collector surface increases. This decreases the particle concentration. Due to the attractive double layer force, particles get closer to the collector and eventually deposit on the collector surface. Since deposited particles are no longer part of dispersed phase, the particle concentration takes the value of zero at the cut-off distance from the collector surface (perfect sink boundary condition). In the case of unfavorable collector, particles accumulate at the distance of secondary

minimum from the collector surface (i.e., $s = 72\ nm$ for the present case), forming a sharp peak in the concentration profile. At closer separation, due to the repulsive electrostatic double layer force, the particle concentration reaches the value of zero. This implies that no particle can get closer than the distance of secondary minimum to the collector surface and the particle deposition rate on such a collector is zero.

Figure 5.6 shows variation of particle deposition rate in form of local Sherwood number, *Sh*, with respect to radial distance from the stagnation point, r for two cases of favorable and unfavorable collectors. All the conditions are the same as those of Figure 5.5. In the case of favorable collector, particle deposition rate, *Sh* (solid line), is normally constant and independent of r up to the radial distance of 100 μm from the stagnation point implying that stagnation point flow system is a uniform collector with respect to deposition. By increasing the radial distance from the stagnation point, the *Sh* decreases. This significant decrease in the local Sherwood number at larger distances from the stagnation point is solely due to the flow distribution in the impinging jet system, characterized by the decrease in the normal velocity component at larger r [Adamczyk *et al.*, 2001]. In contrast, for the case of unfavorable collector, due to the repulsive electrostatic double layer interactions between the particles and the collector, the *Sh* is zero all over the collector surface as predicted by concentration profile in Figure 5.5.

5.9 Numerical Results for Particle Deposition: Heterogeneous Collectors

In this section, we focus on particle deposition rate over heterogeneous collectors with different values of favorable area fraction, $\lambda_{patterned}$. Furthermore, the effects of different parameters on particle deposition over heterogeneous collectors are studied. The results for particle deposition rate are then compared with those predicted by the patchwise heterogeneity model.

Particle concentration profile over a charge heterogeneous collector can be obtained by solving the convection-diffusion equation using finite element analysis and FEMLAB® software according to the procedure explained in Section 5.6. Making use of these results and Eqs. (5.12) and (5.14), one can calculate particle deposition rate represented by Sh_{ave} over a heterogeneous collector. Comparing the Sh_{ave} with those obtained for homogeneous collectors reveals to what extent the charge heterogeneity can affect the particle deposition behaviour in the impinging jet system.

The collector charge heterogeneity is modelled as concentric circular bands with specified width and pitch bearing different surface potentials. The surface potential of the collector, Ψ_s, changes periodically with respect to r, as described in Chapter 3.

5.9.1 Particle Concentration Profile

Solving the convection-diffusion-migration equation provides the particle concentration profile over a micropatterned collector and reveals the distribution of particles in the vicinity of each favorable and unfavorable band. Figure 5.7 shows the variation of particle concentration in the vicinity of the collector surface with r at two different vertical distances from the collector surface. Figure 5.7a shows the particle concentration close to the collector surface around the cut-off distance, $s = 5\ nm$. The region between $500\mu m < r < 600\mu m$ in Figure 5.7a is enlarged and shown in Figure 5.7b. Figure 5.7c depicts the particle concentration around the secondary minimum distance from the collector, $s = 72\ nm$. From this point on, for the sake of simplicity, we call these two distances as close and far from the collector surface, respectively. These results are obtained by solving the convection-diffusion numerically for a collector consisting of alternate negative and positive bands with surface potential of -1 and $+1$, respectively. The widths of negative and positive bands are equal ($\lambda_{patterned} = 50\%$) and assumed to be 10 μm. Throughout this study, the first band on the collector surface is assumed to be negatively charged. The parti-

cle radius and the particle surface potential are assumed to be 1 μm and -1 respectively. The solution ionic strength and flow Reynolds number are 10^{-3}M and 100, respectively.

According to Figure 5.7, the particle concentration profile shows a periodic behaviour over a collector consisting of alternate negative and positive bands. It can be seen in Figure 5.7a that close to the collector surface, the particle concentration is zero over the unfavorable bands throughout the collector surface due to presence of energy barrier and repulsive colloidal interactions between the particles and unfavorable bands. In contrast, inside each favorable band, there is a sharp increase in the particle concentration at the beginning of accessible part of each favorable bands. The particle concentration reaches to an almost constant value by approaching to the trailing edge of each favorable band. Figure 5.7b presents the concentration profile in Figure 5.7a for 500 $\mu m < r < 600$ μm. It can be seen from Figure 5.7b that by increasing the radial distance from the stagnation point, the regions of zero particle concentration over the unfavorable bands are extending to the beginning part of favorable bands. This implies the presence of inaccessible part at the leading edge of favorable stripes that was explained in detail in Section 4.4.

Figure 5.7c shows the variation of particle concentration with r far from the collector surface (i.e., $s = 72$ nm). This vertical distance is around the distance of secondary minimum corresponding to DLVO interactions between the particles and unfavorable bands. A comparison between Figure 5.7a and Figure 5.7c reveals that the concentration profile shows a different behaviour at these two different distances from the collector surface. According to Figure 5.7c, far from the collector surface, the particle concentration reaches its maximum value over the unfavorable band and then decreases as we proceed toward the next favorable band. The different particle concentration behaviour at two different vertical distances from the collector, $s = 5$ nm (Figure 5.7a) and $s = 72$ nm (Figure 5.7c) can be explained by considering the particle concentration profiles over favorable and unfavorable surfaces as was shown in Figure 5.5.

According to Figure 5.5, at the distance of secondary minimum ($s = 72\ nm$), the particle concentration over the favorable surface (solid line) is significantly smaller than the particle concentration over an unfavorable surface (dashed line). This behaviour is exactly similar to what is seen in Figure 5.7c. Figure 5.7c shows that far from the collector surface, the particle concentration reaches its maximum value over the unfavorable band and then decreases as we proceed toward the next favorable band. Considering the particle concentration profile far from the collector surface (Figure 5.7c), and the flow regime, the presence of concentration peak at the beginning of accessible part of each favorable band close to the collector surface (Figure 5.7a), can be explained.

At the distance of secondary minimum from the collector surface, $s = 72\ nm$, particles accumulate over the unfavorable bands at this distance and can not get closer to the collector surface due to the presence of the energy barrier. These particles can be transferred radially towards the next favorable band by means of two mass transfer mechanisms, convection and diffusion. The convection flux in radial direction is a result of the presence of tangential component of fluid velocity. The particles that could not deposit on the unfavorable band can thus be swept toward the next accessible favorable region. The diffusion flux in radial direction is a result of the presence of concentration gradient in radial direction between negative and positive bands. As shown in Figure 5.7c, far from the collector surface, there is a local concentration gradient at the edge of two patches results in radial flux of particles toward the low concentration regions (favorable bands) due to the diffusion effects.

For large particle sizes ($a_p > 1\ \mu m$) which corresponds to large values of Pe, the convective flux is the dominant mechanism in pushing the particles radially toward the next available favorable band. For small particle sizes ($a_p \leqslant 1\ \mu m$) which corresponds to small values of Pe, the diffusive flux along with convective flux are the mechanisms that push the particles radially toward the next favorable band. The variation of radial diffusive and convective flux with respect to r at the distance of secondary minimum from the collector surface,

$s = 72\ nm$, have been shown in Figure 5.8 and Figure 5.9 respectively. All the parameters are the same as those of Figure 5.7.

Figure 5.8 depicts the variation of radial (a) convective and (b) diffusive flux with respect to r for a particle with $a_p = 1\ \mu m$ whereas Figure 5.9 depicts the variation of radial (a) convective and (b) diffusive flux with respect to r for a particle with the radius of 0.1 μm. According to Eq. (5.10), the dimensionless radial convective and diffusive flux are given as $\bar{u}_r f_3 Pe\ c$ and $f_4 \frac{\partial \bar{c}}{\partial \bar{r}}$, respectively. Once the particle concentration is obtained, these expressions can be calculated at any point within the computational domain. Postprocessing routines of FEMLAB® calculate these expressions automatically once the solution is completed.

As shown in these two figures, the values of both radial convective and diffusive flux will increase at the end of each unfavorable band. The only difference is that for the 1 μm particle, the radial convective flux is significantly higher than radial diffusive flux while for 0.1 μm particle, the radial diffusive and convective flux are from the same order of magnitude.

The radial particle flux from unfavorable bands toward the consecutive favorable bands will cause an increase in the particle concentration at the beginning of each favorable band as was shown in Figure 5.7b. The particle concentration decreases by moving radially further towards the end of each favorable band. The particle concentration then reaches the value of zero over the next unfavorable stripe. This periodic behaviour is repeated over the collector surface.

5.9.2 Local Particle Deposition Rate

So far, the particle concentration profile over a heterogeneous collector consisting of alternate negative and positive bands has been obtained. Using these results along with Eq. (5.12), one can calculate local particle deposition rate over such a collector in an impinging jet flow system in form of *Sh*. Figure 5.10 depicts the variation of local Sherwood number with respect to r over a hetero-

geneous collector corresponding to the concentration distribution described in Figure 5.7. All the parameters are the same as those of Figure 5.7.

It can be seen from Figure 5.10a that the local Sherwood number shows a periodic behaviour with r similar to what was observed in Figure 5.7a for particle concentration profile close to the collector surface. The regions of $0 < r < 100\ \mu m$ and $500 < r < 600\ \mu m$ in Figure 5.10a are enlarged and depicted in Figure 5.10b and Figure 5.10c for clarity. It can be seen from Figure 5.10 that the particle deposition rate is zero over the unfavorable bands throughout the collector surface. At the beginning of each favorable band, the particle deposition rate increases drastically and forms the deposition peaks as can be seen in Figure 5.10b. At larger radial distances from the stagnation point, the region of zero deposition rate extends to the leading part of favorable bands due to the presence of inaccessible area at these regions (Figure 5.10c) as discussed in Section 4.4. This behaviour can be explained by considering the variation of particle concentration profile with r close to the collector surface (Figure 5.7a). A comparison between Figure 5.7a and Figure 5.10a clearly shows that the particle deposition rate is zero where the particle concentration is zero, and the particle deposition rate reaches its maximum exactly at the same radial position where the particle concentration reaches its maximum.

A comparison between the local Sherwood number over a homogeneous collector, Figure 5.6, and the local Sherwood number over a heterogeneous collector consisting of negative and positive bands, Figure 5.10, shows a significant difference in the behaviour of particle deposition rate over such surfaces. Although, they both show that the particle deposition rate decreases with increasing the distance from the stagnation point, the dependence of local Sherwood number on radial distance from the stagnation point shows different behaviour over homogeneous and heterogeneous collectors. This difference originates from the difference between the particle distributions over homogeneous and heterogeneous collectors.

5.9.3 Averaged Particle Deposition Rate

The overall particle deposition rate over a substrate is an averaged quantity which is characterized by the ratio of number of particles deposited on a surface to the total surface area of the substrate. In most of deposition applications, it is the total or overall particle deposition rate over a substrate that is important and not the local values of particle deposition rate. Overall particle deposition rate defines on average how many particles deposit on a unit area of a substrate. The overall particle deposition rate is represented by Sh_{ave} in Eulerian approach. Once the local Sh is obtained, the overall particle deposition rate can be calculated using Eq. (5.13) over a surface s in general, or Eq. (5.14) over a region designated by $r_1 < r < r_2$ in the impinging jet system. In order to understand how much the presence of alternate negative and positive bands on a heterogeneous collector surface can change the overall particle deposition rate relative to the overall deposition rate on a homogeneous surface, the Sh_{ave} is calculated for both heterogeneous and homogeneous collectors.

Figure 5.11 shows a comparison between the Sh_{ave} obtained for a heterogeneous collector and for a homogeneous collector for different segments on the collector surface, N_b (i.e., band number in radial direction, Section 3.4.2). The results are obtained for four different particle sizes; (a) $a_p = 1\ \mu m$, (b) $a_p = 0.5\ \mu m$, (c) $a_p = 0.25\ \mu m$, (d) $a_p = 0.1\ \mu m$. The scaled surface potential corresponding to the heterogeneous collector is $\Psi_s = (-1, +1)$ and the scaled surface potential corresponding to the homogeneous collector is $\Psi_s = +1$. All the other parameters are as stated in the Figure 5.7.

The horizontal axis in this figure represents the band number (N_b) in radial direction on the collector surface. The Sh_{ave} corresponding to the first negative and positive bands ($N_b = 1$) is obtained using Eq. (5.14) by defining r_1 and r_2 as $r_1 = 0$ and $r_2 = p$. The Sh_{ave} corresponding to the second negative and positive bands ($N_b = 2$) is obtained using Eq. (5.14) by defining r_1 and r_2 as p and $2p$, respectively. For each of these segments, using the results of Sh corresponding to homogeneous fully favorable collector, the Sh_{ave} is obtained

as well.

The Sh_{ave} corresponding to each band number predicted by the patchwise heterogeneity model is also presented in Figure 5.11. These results are obtained by using Eq. (4.14) and the Sh_{ave} corresponding to each segment on a homogeneous fully favorable collector. According to the patchwise heterogeneity model, Eq. (4.14), the overall deposition rate over a heterogeneous collector consisting of unfavorable and favorable bands can be given in context of Eulerian approach as

$$Sh_{ave} = \lambda_{patterned}\, Sh_{ave_f} \tag{5.23}$$

where Sh_{ave_f} is the averaged particle deposition rate over the homogeneous, fully favorable collector.

In spite of the significant difference between the values of local Sh over the homogeneous and heterogeneous collectors shown in Figure 5.10 and Figure 5.6, it can be seen in Figure 5.11 that for each segment on the collector surface, the values of averaged particle deposition rate, Sh_{ave_f}, over a homogeneous fully favorable collector and the values of Sh_{ave} over a heterogeneous collector with favorable area fraction of 50% are not significantly different. It can also be seen that the values of averaged deposition rate corresponding to each segment on the heterogeneous collector are significantly larger than those predicted by the patchwise heterogeneity model for all of the particle sizes.

According to the patchwise heterogeneity model, since the widths of favorable and unfavorable bands inside each segment on the surface of the heterogeneous collector are equal ($\lambda_{patterned} = 50\%$), the overall particle deposition rate on the heterogeneous collector inside each segment should be half of the overall particle deposition rate on a homogeneous fully favorable collector ($Sh_{ave} = Sh_{ave_f}/2$). Initially, this may sound intuitive. The particle deposition rate is zero over the unfavorable bands. If the deposition rate over the favorable band was equal to the deposition rate over the homogeneous collector, then the averaged deposition rate over the heterogeneous collector would be half of the averaged deposition rate of the homogeneous collector. However, a com-

parison between values of local Sh in Figures 5.6 and 5.10 shows that at the same radial distances from the stagnation point, the local deposition rate over each favorable band on the heterogeneous collector is significantly larger than the corresponding local deposition rate over the homogeneous collector. These relatively higher values of local deposition rate over favorable bands apparently overcome the zero values of deposition rate over unfavorable bands in the averaging process inside each segment. This brings the overall deposition rate over the heterogeneous collector significantly closer to the deposition rate over the homogeneous collector i.e., $Sh_{ave} \gg Sh_{ave_f}/2$.

It can be seen from Figure 5.11, that the particle deposition rate over a homogeneous collector is quite close to that over a heterogeneous collector with 50% favorable area fraction regardless of particle size. For all of the cases shown in Figure 5.11, the particle deposition rate inside each segment over the heterogeneous collector is significantly larger than the deposition rate predicted by the patchwise heterogeneity model, Eq. (5.23).

So far, for all of the cases that have been studied, the width of favorable and unfavorable bands were equal implying that half of the heterogeneous collector surface was covered with favorable charge. Using the convection-diffusion model, the overall deposition rate can also be calculated for heterogeneous collectors with different favorable area fractions, $\lambda_{patterned}$.

Figure 5.12 shows the variation of scaled overall deposition rate (Sh_{ave}/Sh_{ave_f}) with respect to collector favorable area fraction ($\lambda_{patterned}$). For a heterogeneous collector with a constant pitch, different values of $\lambda_{patterned}$ can be achieved by changing the ratio of the width of negative band to the width of positive band, w_n/w_p. In Figure 5.12, the solid line with square symbols denotes the Sh_{ave}/Sh_{ave_f} obtained by numerical simulation of the convection-diffusion-migration equation. The solid line with triangular symbols denotes the Sh_{ave}/Sh_{ave_f} predicted by the original patchwise heterogeneity model whereas the solid line with circular symbols depicts the Sh_{ave}/Sh_{ave_f} predicted by the modified patchwise heterogeneity model.

The results in Figure 5.12 were obtained for a heterogeneous collector consisting of alternate unfavorable and favorable bands with scaled surface potentials of -1 and $+1$ respectively. The pitch is constant and equal to 20 μm. The solution ionic strength and flow Reynolds number are 10^{-3}M and 100 respectively. The particle radius and scaled surface potential are assumed to be 1 μm and -1. All other parameters are the same as those of Figure 5.7.

According to Figure 5.12, the overall deposition rate obtained numerically by solving the convection-diffusion equation deviates significantly from those predicted by both the original and modified patchwise heterogeneity models. The numerical simulations in Figure 5.12 (square-legend line) show that inside the impinging jet system, the Sh_{ave} is zero for a homogeneous, fully unfavorable collector ($\lambda_{patterned} = 0$). However, for the values of $\lambda_{patterned}$ less than 50%, a slight increase in the $\lambda_{patterned}$ will result in a significant increase in the Sh_{ave}. This has been reported in literature before [Adamczyk *et al.*, 2003]. Furthermore, it can be observed that when $\lambda_{patterned}$ is around 50%, further increase in $\lambda_{patterned}$ does not affect the Sh_{ave} significantly. For the values of $\lambda_{patterned}$ larger than 50%, Sh_{ave} is very close to the Sh_{ave_f} for a homogeneous fully favorable collector ($\lambda_{patterned} = 100\%$). This was also evident in Figure 5.11 where the overall deposition rate over a heterogeneous collector with $\lambda_{patterned}$ of 50% was very close to the Sh_{ave_f} over a homogeneous fully favorable collector.

Overall, it can be seen from Figure 5.12 that the particle deposition rate based on the convection-diffusion-migration is larger than that predicted by the original and modified patchwise heterogeneity models for all $\lambda_{patterned}$. Similar to the results shown in Section 4.5.2, once again it has been observed that the modification of the original patch model by replacing $\lambda_{patterned}$ by its actual value does not improve the predictions of the patchwise heterogeneity model for the particle deposition rate. Consequently, it can be deduced that the failure of the patchwise heterogeneity model in predicting particle deposition in presence of micro-scale heterogeneity does not stem from the erroneous values of $\lambda_{patterned}$. This failure stems from the inadequate averaging process that this

model proposes for calculating particle deposition rate in case of micro-scale charge heterogeneity.

Comparing the results of overall deposition rate obtained by finite element analysis with those predicted by the patchwise heterogeneity model implies that, in the impinging jet system, the variation of scaled overall deposition rate, Sh_{ave}, with $\lambda_{patterned}$ is not linear as was predicted by the patchwise heterogeneity model. The reason can be better explained by incorporating some mathematical expressions. Let us imagine a scenario similar to Figure 5.11 where we compared the overall deposition rate inside a segment on a heterogeneous collector with the overall deposition rate inside the same segment on a homogeneous collector. First we consider one segment on the heterogeneous collector with favorable area fraction of $\lambda_{patterned}$. This segment consists of one unfavorable and one favorable band with surface areas of S_u and S_f implying that the total surface area of the segment is $S_{total} = S_u + S_f$. The width of this segment is equal to p. According to the definition of $\lambda_{patterned}$, we also know that $S_f/S_{total} = \lambda_{patterned}$.

The local Sh on unfavorable and favorable bands are assumed to be Sh_u and Sh_{fav}. Next, we consider the same segment on the homogeneous fully favorable collector with surface area of S_{total}. The local deposition rate over this segment is considered to be Sh_f. The ratio of overall deposition rate inside this segment on the heterogeneous collector to the overall deposition rate inside the same segment on the homogeneous collector can be written according to Eq. (5.13) as

$$\frac{Sh_{ave}}{Sh_{ave_f}} = \frac{\frac{1}{S_{total}}(\int_{S_u} Sh_u\, dS + \int_{S_f} Sh_{fav}\, dS)}{\frac{1}{S_{total}} \int_{S_{total}} Sh_f\, dS} \tag{5.24}$$

It can be assumed that the Sh_f on the homogeneous collector is constant inside the segment (due to the small width of the segment p) and thus can be removed from the integral. Knowing that $Sh_u = 0$, the above equation can then be simplified to

$$\frac{Sh_{ave}}{Sh_{ave_f}} = \frac{1}{S_{total}} \cdot \frac{1}{Sh_f} \int_{S_f} Sh_{fav}\, dS = \frac{1}{S_{total}} \int_{S_f} \frac{Sh_{fav}}{Sh_f}\, dS \tag{5.25}$$

where Sh_{fav} is the local deposition rate over the favorable band on the hetero-

geneous collector whereas Sh_f is the local deposition rate inside the segment on the homogeneous collector. If the value of Sh_{fav} is equal to Sh_f, Eq. (5.25) simplifies to

$$\frac{Sh_{ave}}{Sh_{ave_f}} = \frac{S_f}{S_{total}} = \lambda_{patterned} \tag{5.26}$$

which is identical to the patchwise heterogeneity model expression, Eq. (5.23). However, as was shown in Figure 5.10, the local deposition rate over favorable bands on the heterogeneous collector, Sh_{fav}, is significantly larger than the local deposition over homogeneous collector, Sh_f, due to the radial flux of non-deposited particles from the unfavorable bands towards the favorable bands.

According to Eq. (5.25), when the ratio of $Sh_{fav}/Sh_f > 1$, it indicates that $Sh_{ave}/Sh_{ave_f} > S_f/S_{total}$. Knowing that $S_f/S_{total} = \lambda_{patterned}$, one can deduce that $Sh_{ave}/Sh_{ave_f} > \lambda_{patterned}$. This indicates that the ratio of Sh_{ave} over Sh_{ave_f} is not equal to $\lambda_{patterned}$ as suggested by the patchwise heterogeneity model.

The non-linear relation between overall deposition rate and favorable area fraction of the collector has been observed once before in Figure 4.12. There, the trajectory analysis was used to calculate the particle deposition rate as η corresponding each value of $\lambda_{patterned}$. The results in Figures 4.12 and 5.12 show an identical qualitative behaviour of overall deposition rate with respect to $\lambda_{patterned}$. They both depict that the variation of Sh_{ave} with $\lambda_{patterned}$ does not follow a linear relationship in an impinging jet system in the presence of micro-size heterogeneity.

5.10 Summary

In this chapter, the particle deposition rate was obtained in context of Eulerian approach. The convection-diffusion equation with appropriate boundary conditions was solved numerically using finite element method inside the impinging jet flow system. Using the values of particle concentration, the local and overall particle deposition rates were calculated for both homogeneous and heterogeneous collectors. It was observed that the particle concentration and local

particle deposition rate increase significantly at the beginning of each favorable band on the surface of the heterogeneous collector. The presence of these spikes at the beginning of each favorable band was justified by considering the numerical results for radial convective and diffusive flux. These results revealed that the particles that did not deposit on the unfavorable bands due to the presence of the energy barrier were swept toward the next available favorable bands due to the tangential component of fluid velocity and lateral diffusion.

The averaged (overall) particle deposition rate was calculated for the heterogeneous collector with different values of favorable area fraction and the results were compared with those predicted by the patchwise heterogeneity model. It was seen that the overall particle deposition rate obtained by finite element analysis deviates significantly from those predicted by both the original and modified patchwise heterogeneity models. No linear relation was seen between the overall particle deposition and the collector favorable area fraction as was suggested by the patchwise heterogeneity model. The variation of overall deposition rate with favorable area fraction that was obtained by solving convection-diffusion equation shows the same qualitative behavoiur as was seen before through trajectory analysis. The result of overall deposition rate based on Eulerian approach was in agreement with that found previously based on Lagrangian approach.

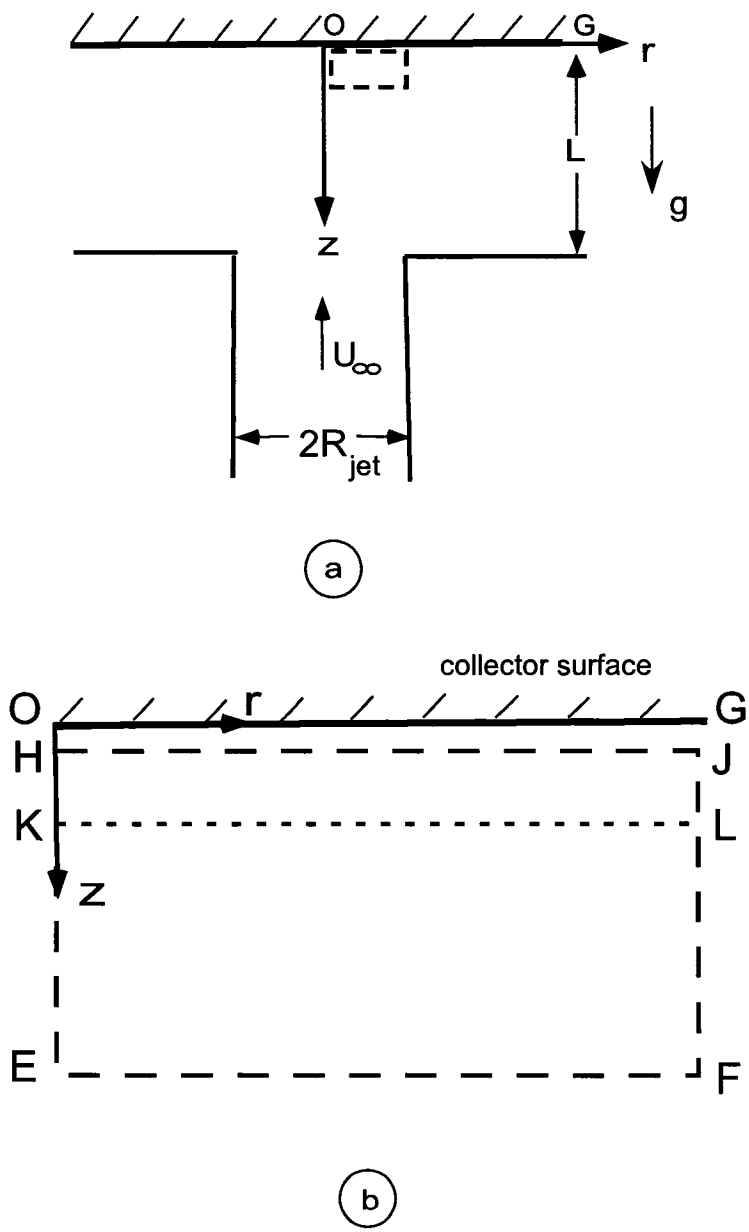

Figure 5.1: (a) A schematic presentation of impinging jet system geometry. The dashed rectangular depicts the computational domain shown in detail in part(b). (b) Computational domain used in solving convection-diffusion equation by finite element method.

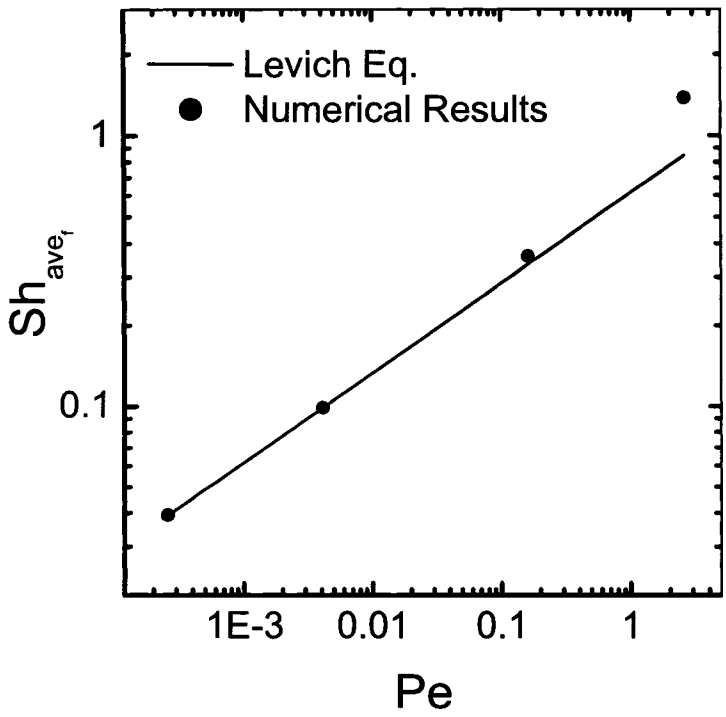

Figure 5.2: Variation of overall deposition rate with respect to Peclet number for a homogeneous fully favorable collector in the absence of energy barrier, inside the stagnation point region. Solid line denotes the values of Sh_{ave_f} calculated by Levich equation whereas symbols represents the Sh_{ave_f} obtained by solving convection-diffusion equation numerically.

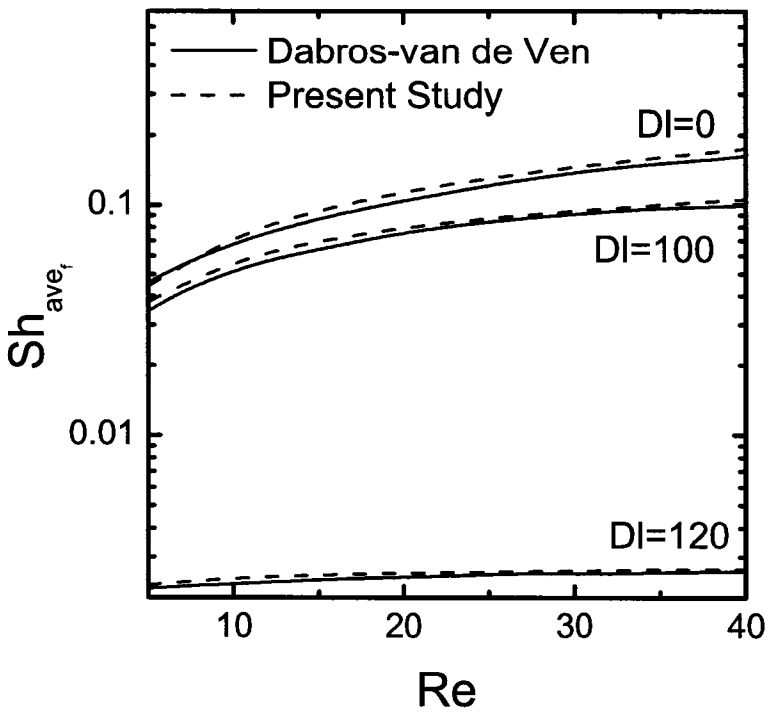

Figure 5.3: Variation of overall deposition rate with respect to flow Reynolds number for a homogeneous unfavorable collector in the presence of energy barrier, inside the stagnation point region. Solid line denotes the values of Sh_{ave} caculated numerically by Dabros and van de Ven for three different values of double layer parameter, Dl . Dashed line represents the Sh_{ave} obtained by solving convection-diffusion equation numerically.

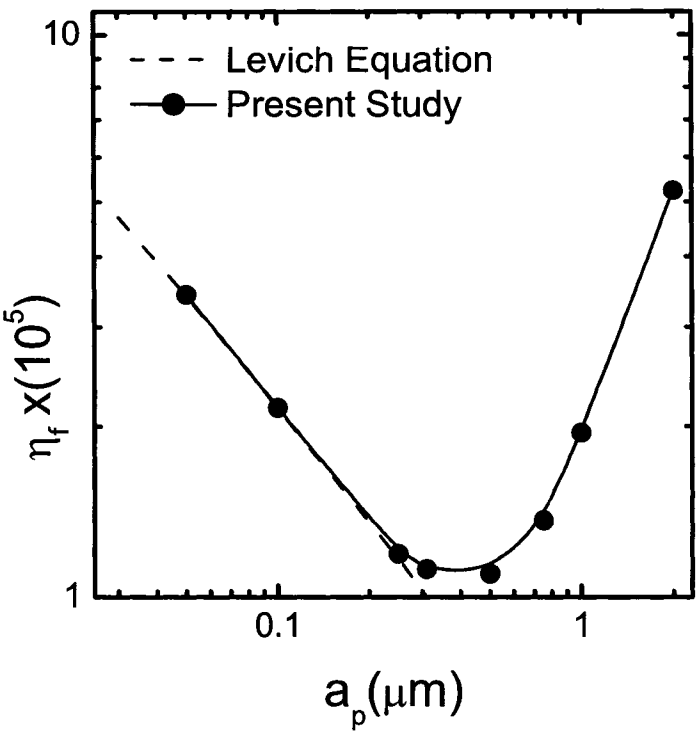

Figure 5.4: Variation of overall deposition efficiency, η_f, with respect to particle radius for a homogeneous fully favorable collector inside the stagnation point flow domain. Solid line with circular symbols denotes the values of η_f calculated by solving convection-diffusion equation numerically ($\Psi_s = +1$, $\Psi_p = -1$, $Re = 100$, $I = 10^{-3}$ M). Dashed line denoted the η_f obtained using Levich equation.

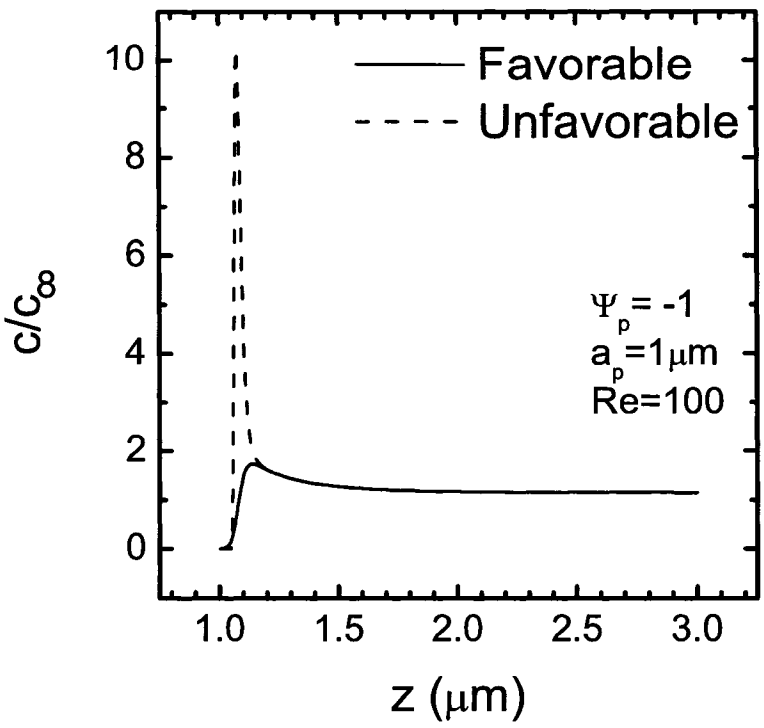

Figure 5.5: Variation of particle concentration with the vertical distance from the collector surface, z, at the stagnation point, $r = 0$. The results are obtained by solving convection-diffusion numerically inside the impinging get flow geometry. Solid line depicts the particle concentration profile over a homogeneous fully favorable collector with $\Psi_s = +1$. Dashed line denotes the particle concentration profile over a homogeneous fully unfavorable collector with $\Psi_s = -1$. All the other parameters are the same as in Figure 5.4.

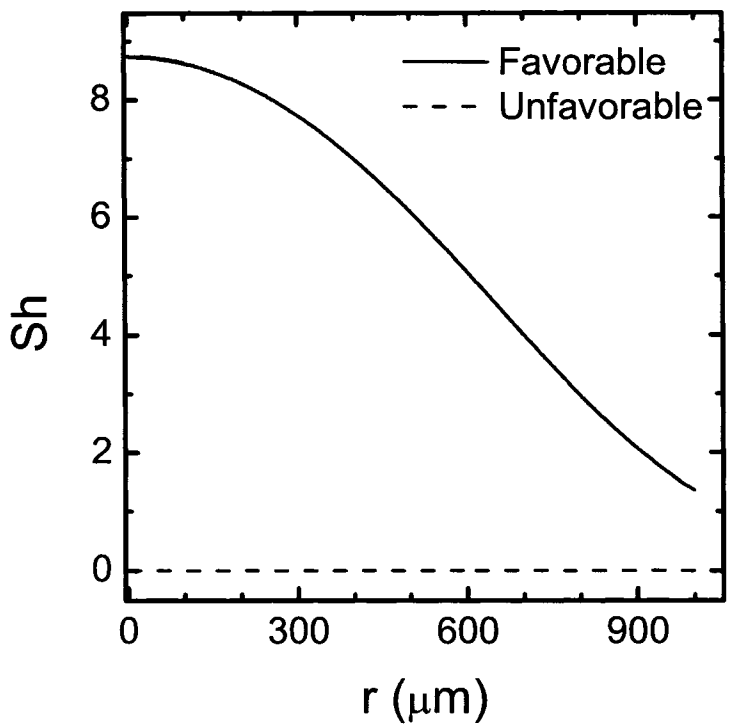

Figure 5.6: Variation of local particle deposition rate, *Sh* with the radial distance from the collector surface, r. Solid line depicts the particle concentration profile over a homogeneous fully favorable collector with $\Psi_s = +1$. Dashed line denotes the particle concentration profile over a homogeneous fully unfavorable collector with $\Psi_s = -1$. All the other parameters are the same as in Figure 5.4.

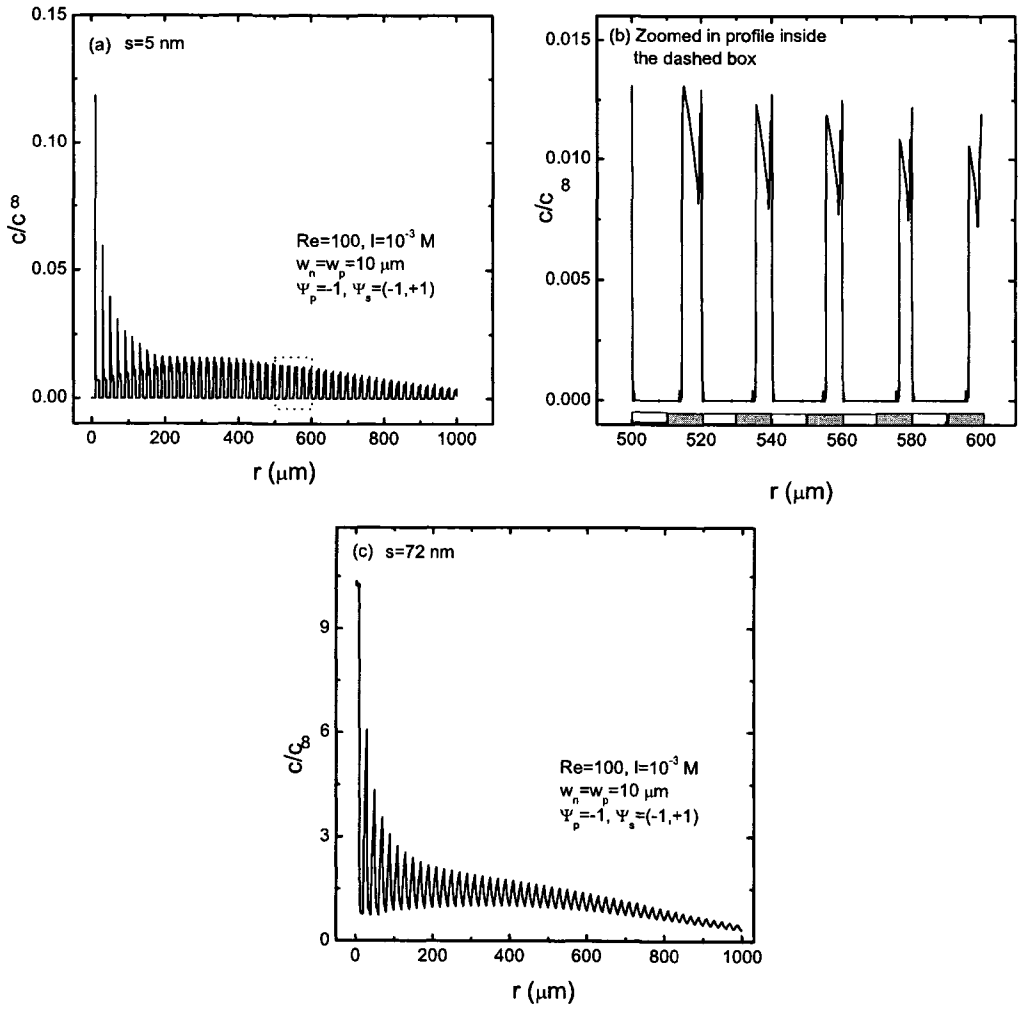

Figure 5.7: Variation of scaled particle concentration with the radial distance from the stagnation point, r, at two different vertical distances from the collector surface, (a) $s = 5\ nm$ where the regions between $500\ \mu m < r < 600\ \mu m$ is enlarged in (b).(c)$s = 72\ nm$.

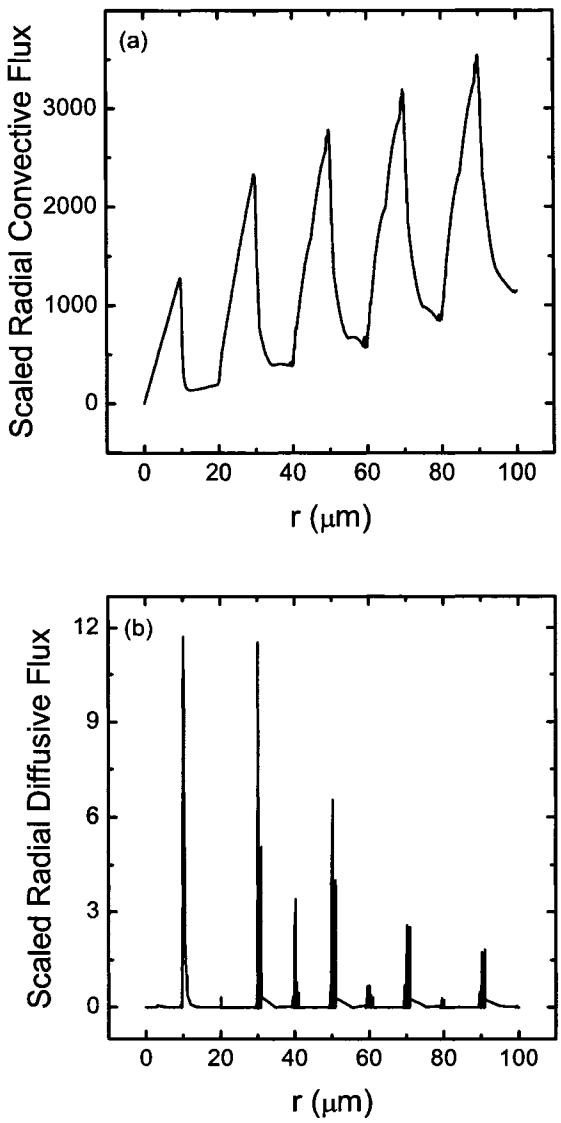

Figure 5.8: Variation of scaled radial (a) convective (b) diffusive flux on the radial distance from the stagnation point, r, at the vertical distance from the collector surface around the secondary minimum. Particle radius is assumed to be 1 μm. All the other parameters are the same as in Figure 5.7

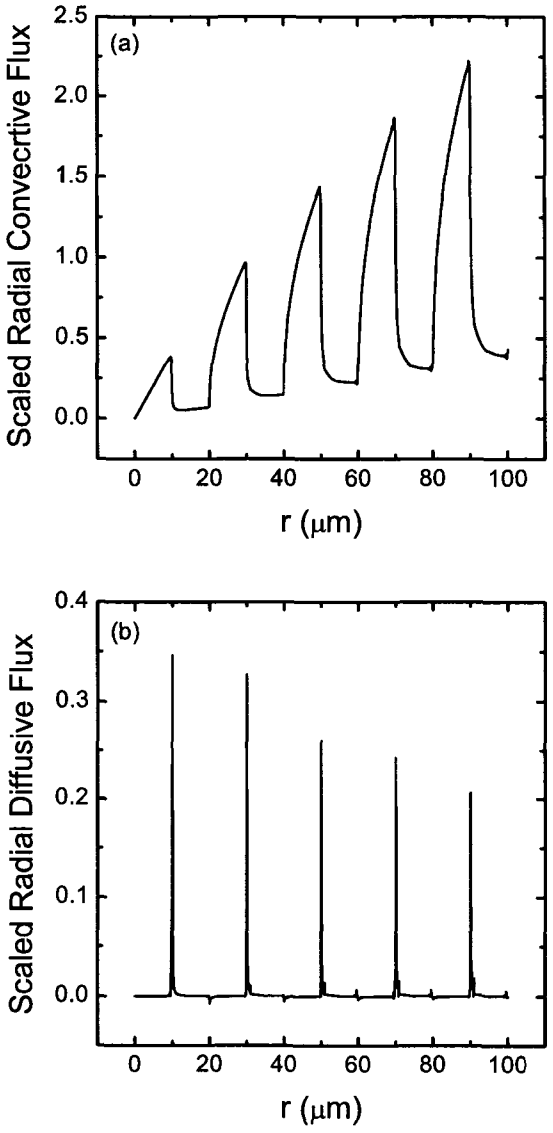

Figure 5.9: Variation of scaled radial (a) convective (b) diffusive flux on the radial distance from the stagnation point, r, at the vertical distance from the collector surface around the secondary minimum. Particle radius is assumed to be 0.1 μm. All the other parameters are the same as in Figure 5.7

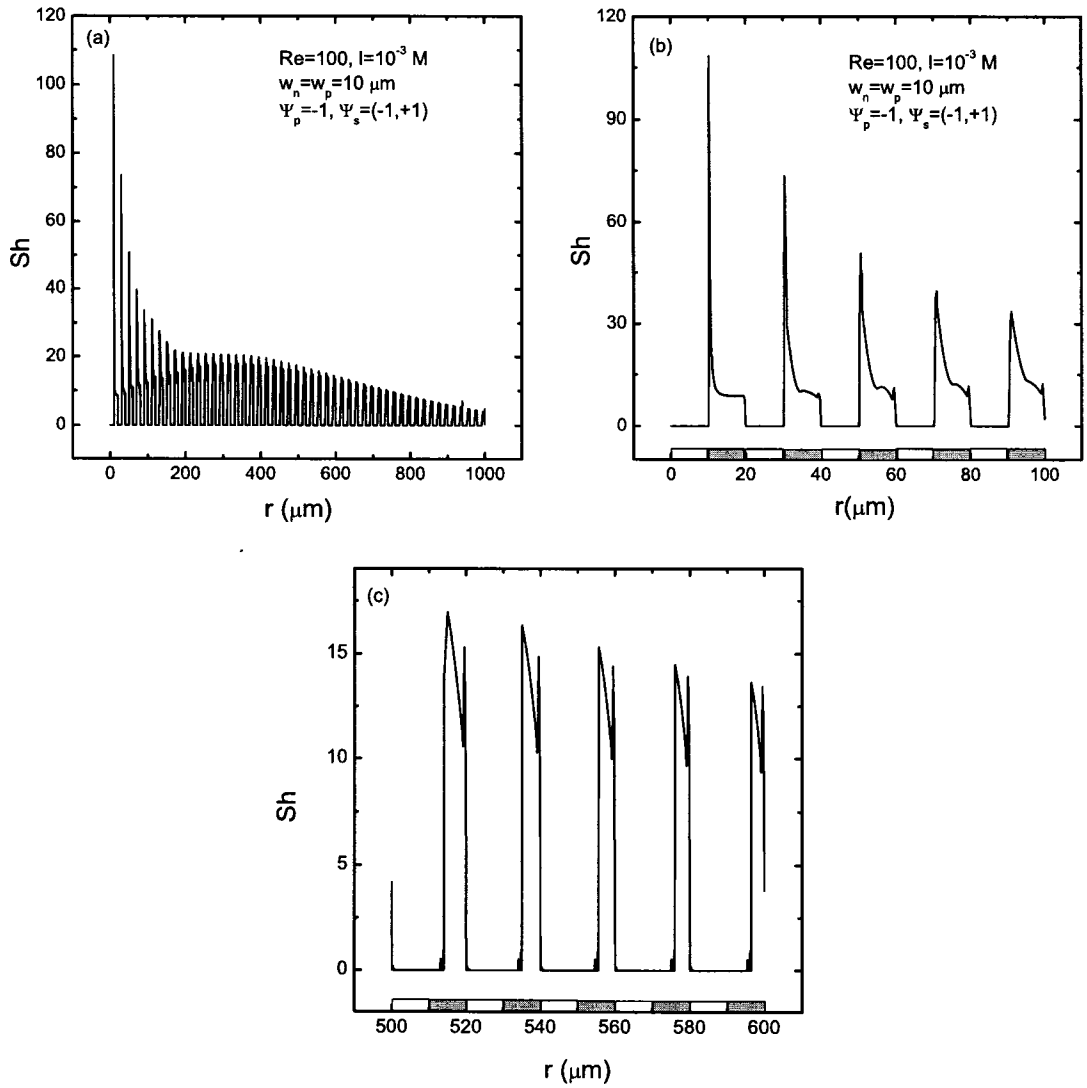

Figure 5.10: Variation of local particle deposition rate, Sh, with radial distance from the stagnation point, r, at the collector surface. The region with $0 < r < 100\ \mu m$ of this figure is enlarged in part (b). The region with $500\ \mu m < r < 600\ \mu m$ of this figure is enlarged in part (c).

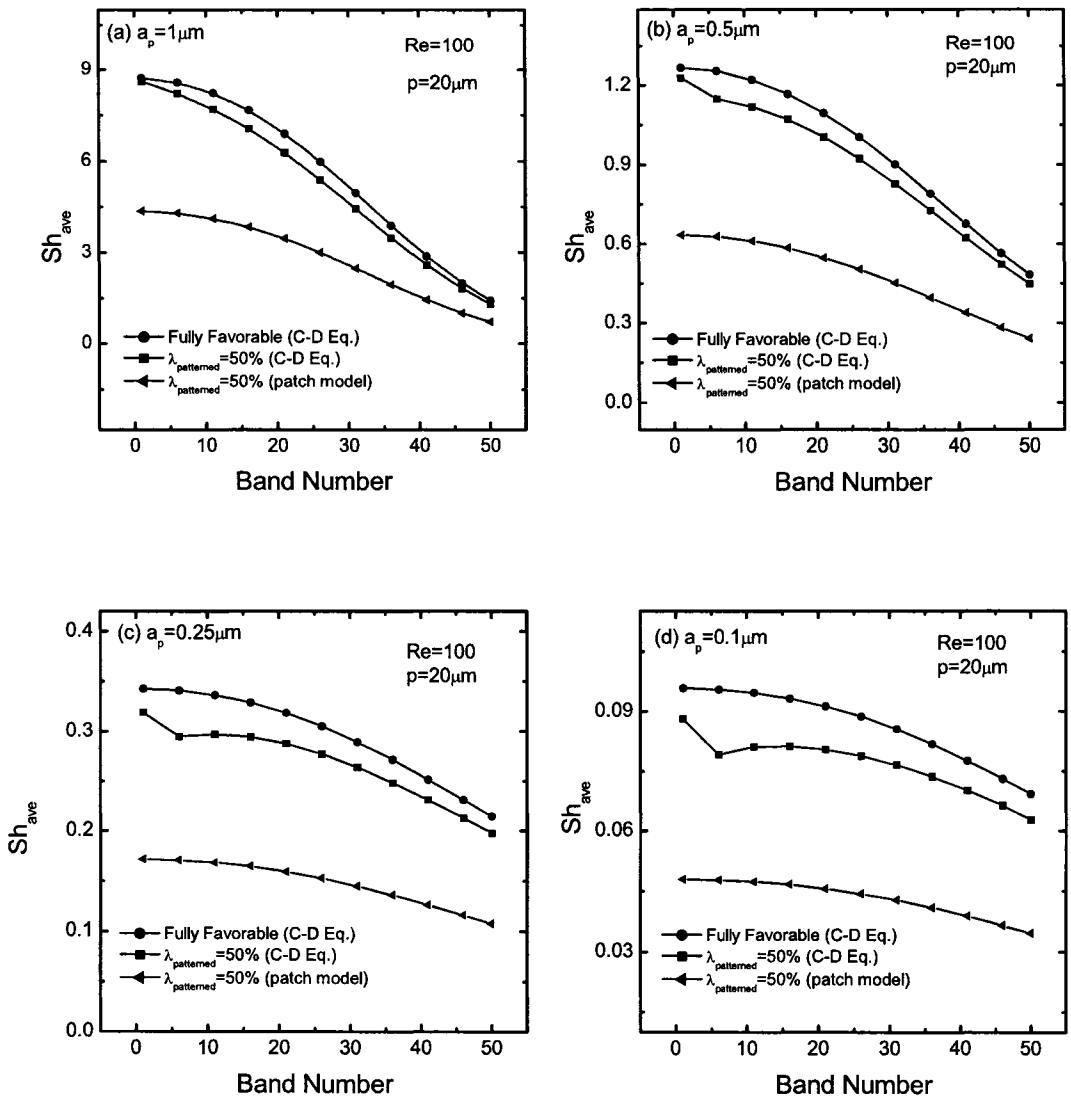

Figure 5.11: Variation of Sh_{ave} with band number, N_b for four particle sizes i.e., (a) $a_p = 1\ \mu m$, (b) $a_p = 0.5\ \mu m$, (c) $a_p = 0.25\ \mu m$, (d) $a_p = 0.1\ \mu m$. Square-legend line denotes Sh_{ave} over a heterogeneous collector with $\psi_s = (-1, +1)$ obtained by numerical simulation. Triangle-legend line denotes Sh_{ave} predicted by the patchwise heterogeneity model over a heterogeneous collector with $\psi_s = (-1, +1)$ and circle-legend line denotes Sh_{ave_f} over a homogeneous fully favorable collector with $\psi_s = +1$.All the other parameters are the same as in Figure 5.7.

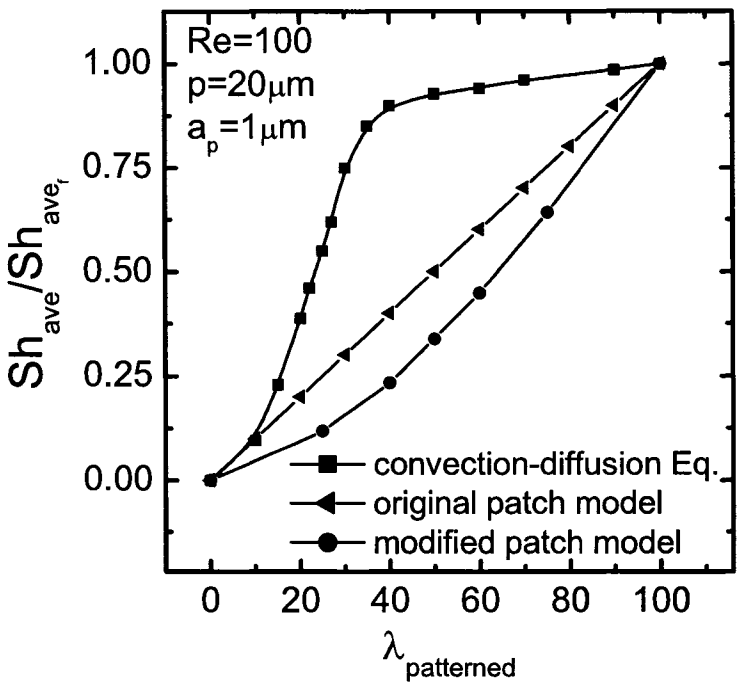

Figure 5.12: Variation of scaled overall particle deposition rate, Sh_{ave}/Sh_{ave_f}, with favorable area fraction of the collector, $\lambda_{patterned}$. The square-legend line denotes the overall deposition rate obtained by solving convection-diffusion equation. The triangle-legend line denotes values of overall deposition rate obtained by the original patchwise heterogeneity model. The circle-legend line denotes values of overall deposition rate obtained by the modified patchwise heterogeneity model. All the other parameters are the same as in Figure 5.7.

Chapter 6

Conclusion and Future Work

6.1 Concluding Remarks

The simulations performed in this study reveal the effects of micro-scale charge heterogeneity on particle deposition onto the smooth substrates inside the radial impinging jet flow geometry. In addition to particle deposition, the particle trajectory and particle distribution in the vicinity of the heterogeneous collector in the presence of external forces were studied. Based on the literature review, a number of publications have been found that focus on the study of particle deposition inside the radial impinging jet geometry onto the homogeneous surfaces using various numerical and experimental techniques. However, there was a lack of systematic studies on particle deposition in the presence of microscopic surface charge heterogeneity. One method that has been used frequently to calculate particle deposition rate over heterogeneous surfaces is based on a spatial averaging process and is called the patchwise heterogeneity model. It has been shown in this study that although this model works well for macroscopic heterogeneity, it fails to predict the particle deposition rate in the presence of micro-scale charge heterogeneity.

The major conclusions that can be drawn from this study of particle deposition onto micropatterned charge heterogeneous substrates are

1. The fluid flow field of the impinging jet flow is characterized by two different velocity profiles close and far from the stagnation point. In the

vicinity of the stagnation point, the normal component of fluid velocity is dominant compared to radial component of fluid velocity whereas far from the stagnation point, the radial component of the fluid velocity plays dominant role. This has been considered as an advantage for impinging jet system since it allows for the study of the effects of hydrodynamic interactions on particle deposition behaviour by comparing the particle deposition process close and far from the stagnation point.

2. The presence of periodic charge heterogeneity gives rise to an oscillating particle trajectory in the vicinity of the collector surface consisting of alternate positive and negative bands due to the alternating attractive and repulsive particle-substrate colloidal forces. The wavelength and amplitude of this oscillating trajectory can be controlled by changing the width of the favorable and the unfavorable bands, the particle and substrate surface potentials, and solution ionic strength.

3. Due to the hydrodynamic interaction effects, one can render a partially favorable surface to act as a fully unfavorable surface with respect to deposition at different ratios of normal to tangential fluid velocity when all of the other parameters are maintained constant.

4. As a result of the coupled influence of hydrodynamic and colloidal forces, there exists a region near the leading edge of each favorable band on the collector surface that is not accessible to particle deposition, implying that the actual favorable area fraction of the collector is less than its nominal value. The inaccessible area increases further away from stagnation point owing to the dominant role of the tangential fluid velocity.

5. The particle deposition results based on the trajectory analysis method deviate significantly from the particle deposition results based on averaging process proposed by the patchwise heterogeneity model. According to the results obtained by trajectory model, the variation of particle deposition over a heterogeneous substrate with respect to favorable area fraction

of the surface is not linear as was predicted by the patchwise heterogeneity model.

6. Based on trajectory analysis, when the substrate is initially fully unfavorable, the particle deposition rate increases significantly by the presence of the charge heterogeneity in form of a slight fraction of favorable charge on the substrate surface. In contrast, when the surface is initially fully favorable, the particle deposition rate remains almost unaffected by the presence of charge heterogeneity in form of unfavorable charge on the substrate surface.

7. Solution of convection-diffusion-migration equation numerically provides the particle deposition rates over both homogeneous and heterogeneous collectors. Using this model, it was observed that due to the tangential component of fluid velocity and Brownian motion of the particles, there is a radial flux at the boundary between unfavorable and favorable bands that pushes the particles accumulating over the unfavorable stripes due to the energy barrier, toward the next accessible favorable region. This causes a sharp increase in the particle concentration as well as particle deposition at the accessible part of favorable bands over the heterogeneous collector. The high value of particle deposition rate at the favorable bands was considered as the reason for high values of overall particle deposition over heterogeneous collectors inside the impinging jet region compared to the particle deposition rate predicted by the patchwise heterogeneity model for such surfaces.

6.2 Future Works

The study presented in this work is an initial step toward a general systematic investigation on the role of micro-scale charge heterogeneity on particle deposition process. During this study, some simplifications have been made which

may not be suitable for a more general investigation. Based on the results that were obtained during this study, the following recommendations can be made to achieve a more rigorous model for predicting particle deposition in the vicinity of the micro-scale charge heterogeneity.

1. In this study, the charge heterogeneity was modelled as concentric circular bands bearing different surface potentials. This allows a systematic investigation on the role of heterogeneity in particle deposition since if the distribution of the heterogeneous patches is known *a priori*, their influence on particle deposition becomes more tractable. On the other hand, the simulation of charge heterogeneity as circular bands allows the use of two-dimensional cylindrical coordinate system for modelling the particle deposition inside the radial impinging jet geometry. However, natural surfaces contain surface charge heterogeneity that are randomly distributed, of arbitrary geometrical shapes, and having widely varying chemical properties. Therefore, a more rigorous model can be developed by simulating charge heterogeneity as randomly distributed patches over the surface bearing different surface charges. This requires that the numerical simulation be conducted in a three dimensional coordinate system.

2. The electrostatic double layer interaction force between the charged particle and the heterogeneous collector was calculated using the well-known Hogg, Healy, and Fuerstenau (HHF) expression. In order to justify the use of this equation in our study, some simplifications and assumptions were made. It was assumed when the particle center passes over a positive band, the electrostatic interaction is solely that between the negatively charged particle and an infinite planar surface bearing a positive surface potential. Similarly, as long as the particle is directly facing a negative band on the surface, the electrostatic interaction is calculated assuming the entire surface to have a negative surface potential. This assumption is clearly a gross simplification of the actual electrostatic double layer interaction between a charge heterogeneous substrate and the particle. It

also imposed a limitation on the range of the band width that can be selected in this study since this assumption is valid as long as the individual band width is larger than the particle size, the particle is sufficiently close to the substrate, and the electrostatic double layer interactions are sufficiently screened (large κa_p). A more rigorous approach of calculating the force between the particle and the charged stripes can be achieved by solving the Poisson-Boltzmann equation numerically and calculating the electrostatic interaction force between the particle and the substrate. Calculating F_{edl} numerically allows selecting a wide range of band width with respect to particle size.

3. The lateral (tangential) force between the particle and the substrate is assumed to be negligible in this study. This assumption is only valid for values of κa_p equal or greater than 100 (which is the range used in the present work). Evaluating the electrostatic double layer force between the particle and the heterogeneous substrate numerically by solving the Poisson-Boltzmann equation may enable us to obtain the value of lateral force exerted on particles due to the presence of alternate bands on the collector surface.

4. In this study, the particle deposition process is considered to be at the initial stages when the collector surface is clean and not blocked by the already deposited particles. A more realistic model can be achieved by considering deposition when the blocking effects play a significant role in defining the particle deposition rate on the collector surface. The deposited particles on the collector surface often substantially reduce deposition rates because they create a blocked surface area, that can be greater than the size of a particle itself. The surface charge heterogeneity may manifest itself differently in the presence of blocking effects. In order to take into account the surface blocking effects in the present study, one has to implement the convection-diffusion equation in form of time vari-

ant problem. There are various functions available in literature that can be employed to model the surface blocking process inside the convection-diffusion equation.

5. Finally, using the micropatterning techniques and the impinging jet apparatus, an experimental investigation can be performed to explore the role of charge heterogeneity on particle deposition inside the impinging jet flow regime.

Bibliography

Adamczyk, Z. (1989). Particle deposition from flowing suspensions. *Colloids and Surfaces* **39**(1-3), 1.

Adamczyk, Z. and T. G. M. van de Ven (1981). Deposition of particles under external forces in laminar-flow through parallel-plate and cylindrical channels. *Journal of Colloid and Interface Science* **80**(2), 340.

Adamczyk, Z., B. Siwek, P. Warszynski and E. Musial (2001). Kinetics of particle deposition in the radial impinging-jet cell. *Journal of Colloid and Interface Science* **242**(1), 14.

Adamczyk, Z., B. Siwek, P. Weronski and K. Jaszczolt (2003). Particle deposition at electrostatically heterogeneous surfaces. *Colloids and Surfaces a-Physicochemical and Engineering Aspects* **222**(1-3), 15.

Adamczyk, Z., M. Zembala, B. Siwek and J. Czarnecki (1986). Kinetics of latex particle deposition from flowing suspensions. *Journal of Colloid and Interface Science* **110**(1), 188.

Bitton, G., D. B. Ivanoff and B. Koopman (1991). Int reduction as a basis for determining bakers-yeast viability. *International Journal of Food Science and Technology* **26**(3), 307.

Boluk, M. Y. and T. G. M. van de Ven (1990). Effects of polyelectrolytes on flow-induced deposition of titanium-dioxide particles onto a cellophane surface. *Colloids and Surfaces* **46**(2-4), 157.

Brenner, H. (1961). The slow motion of a sphere through a viscous fluid towards a plane surface. *Chemical Engineering Science* **16**(3-4), 242.

Dabros, T. and T. G. M. van de Ven (1983). A direct method for studying particle deposition onto solid-surfaces. *Colloid and Polymer Science* **261**(8), 694.

Dabros, T. and Z. Adamczyk (1979). Noninertial particle transfer to the rotating-disk under an external force-field (laminar-flow). *Chemical Engineering Science* **34**(8), 1041.

Deshpande, M. D. and R. N. Vaishnav (1982). Submerged laminar jet impingement on a plane. *Journal of Fluid Mechanics* **114**(JAN), 213.

Elimelech, M. (Menachem) (1995). *Particle Deposition and Aggregation : Measurement, Modelling, and Simulation.* Colloid and surface engineering series. Oxford [England] ; Boston : Butterworth-Heinemann.

Elimelech, M., Z. A. Kuznar and J. Y. Chen (2003). Deposition of colloidal particles on chemically heterogeneous surfaces: Role of microscopic surface charge heterogeneity. *Abstracts of Papers of the American Chemical Society* **226**, U479. Part 1.

Goldman, A. J., R. G. Cox and H. Brenner (1967*a*). Slow viscous motion of a sphere parallel to a plane wall .II. couette flow. *Chemical Engineering Science* **22**(4), 653.

Goldman, A. J., R. G. Cox and H. Brenner (1967*b*). Slow viscous motion of a sphere parallel to a plane wall .I. motion through a quiescent fluid. *Chemical Engineering Science* **22**(4), 637.

Goren, S. L. (1970). Normal force exerted by creeping flow on a small sphere touching a plane. *Journal of Fluid Mechanics* **41**, 619.

Goren, S. L. and M. E. Oneill (1971). Hydrodynamic resistance to a particle of a dilute suspension when in neighbourhood of a large obstacle. *Chemical Engineering Science* **26**(3), 325.

Hirtzel, C. S. and R. Rajagopalan (1985). Stability of colloidal dispersions. *Chemical Engineering Communications* **33**(5-6), 301.

Hogg, R., T. W. Healy and Fuersten.Dw (1966). Mutual coagulation of colloidal dispersions. *Transactions of the Faraday Society* **62**(522P), 1638.

Honig, E. P., Roeberse.Gj and P. H. Wiersema (1971). Effect of hydrodynamic interaction on coagulation rate of hydrophobic colloids. *Journal of Colloid and Interface Science* **36**(1), 97.

Hunter, Robert J. (1981). *Zeta potential in colloid science : principles and applications.* (Colloid science (London, England : 1976)ISSN0305-9723 ; 2). London ; New York : Academic Press.

Israelachvili, J.N. (1985). *Intermulecular and Surface Forces.* 2nd ed.. Academic Press. London.

Khachatourian, A. V. M. and A. O. Wistrom (1998). Electrostatic interaction force between planar surfaces due to 3-d distribution of sources of potential (charge). *Journal of Physical Chemistry B* **102**(14), 2483.

Kihira, H., N. Ryde and E. Matijevic (1992). Kinetics of heterocoagulation .2. the effect of the discreteness of surface-charge. *Journal of the Chemical Society-Faraday Transactions* **88**(16), 2379.

Koopal, L. K. and S. S. Dukhin (1993). Modeling of the double-layer and electrosorption of a patchwise heterogeneous surface on the basis of its homogeneous analog .1. noninteracting patches. *Colloids and Surfaces a-Physicochemical and Engineering Aspects* **73**, 201.

Levich, V. G. (1962). *Physicochemical Hydrodynamics.* Prentice-Hall. Englewood Cliffs, New Jersey.

Masliyah, Jacob Heskel (1994). *Electrokinetic Transport Phenomena.* AOSTRA technical publication series ; no. 12. Edmonton, Alta. : Alberta Oil Sands Technology and Research Authority.

McCarthy, J. F. (1989). Correction. *Environmental Science and Technology* **23**(7), 752.

Nelson, K. E. and T. R. Ginn (2005). Colloid filtration theory and the happel sphere-in-cell model revisited with direct numerical simulation of colloids. *Langmuir* **21**(6), 2173.

Polat, S., Huang B. Mujumdar A.S. Douglas W.J.M. (1991). *Numerical Flow and Heat Transfer under Impinging Jets-a Review..* Vol. 2 of *Ann. Rev. Num. Fluid Mech. and Heat Transfer.* Hemisphere. New York.

Prieve, D. C. and M. M. J. Lin (1980). Adsorption of brownian hydrosols onto a rotating-disk aided by a uniform applied force. *Journal of Colloid and Interface Science* **76**(1), 32.

Prieve, D. C. and Ruckenst.E (1974). Effect of london forces upon rate of deposition of brownian particles. *Aiche Journal* **20**(6), 1178.

Rajagopalan, R. and C. Tien (1976). Trajectory analysis of deep-bed filtration with sphere-in-cell porous-media model. *Aiche Journal* **22**(3), 523.

Rajagopalan, R. and C. Tien (1977). Single collector analysis of collection mechanisms in water filtration. *Canadian Journal of Chemical Engineering* **55**(3), 246.

Rajagopalan, R. and J. S. Kim (1981). Adsorption of brownian particles in the presence of potential barriers - effect of different modes of double-layer interaction. *Journal of Colloid and Interface Science* **83**(2), 428.

Richmond, P. (1974). Non-retarded vanderwaals,hg der waals energies between a finite rod and a planar substrate. *Journal of the Chemical Society-Faraday Transactions Ii* **2**(70), 229.

Ruckenstein, E. and D. C. Prieve (1973). Rate of deposition of brownian particles under action of london and double-layer forces. *Journal of the Chemical Society-Faraday Transactions* **69**(10), 1522.

Shellenberger, K. and B. E. Logan (2002). Effect of molecular scale roughness of glass beads on colloidal and bacterial deposition. *Environmental Science and Technology* **36**(2), 184.

Song, L. F., P. R. Johnson and M. Elimelech (1994). Kinetics of colloid deposition onto heterogeneously charged surfaces in porous-media. *Environmental Science and Technology* **28**(6), 1164.

Spielman, L. A. and J. A. Fitzpatrick (1973). Theory for particle collection under london and gravity forces. *Journal of Colloid and Interface Science* **42**(3), 607.

Suzuki, A., N. F. H. Ho and W. I. Higuchi (1969). Predictions of particle size distribution changes in emulsions and suspensions by digital computation. *Journal of Colloid and Interface Science* **29**(3), 552.

Tien, Chi (1989). *Granular filtration of aerosols and hydrosols.* Boston : Butterworths Publishers.

Tufenkji, N., G. F. Miller, J. N. Ryan, R. W. Harvey and M. Elimelech (2004). Transport of cryptosporidium oocysts in porous media: Role of straining and physicochemical filtration. *Environmental Science and Technology* **38**(22), 5932.

Vaidyanathan, R. and C. Tien (1991). Hydrosol deposition in antigranulocytes media under unfavorable surface conditions. *Chemical Engineering Science* **46**(4), 967.

van de Ven, T. G. M. (1989). *Colloidal Hydrodynamics.* Academic Press. San Diego.

Vreeker, R., A. J. Kuin, D. C. Denboer, L. L. Hoekstra and W. G. M. Agterof (1992). Stability of colloidal particles with a nonhomogeneous surface-potential - application to colloidal nickel hydroxy carbonate. *Journal of Colloid and Interface Science* **154**(1), 138.

Walz, J. Y. (1998). The effect of surface heterogeneities on colloidal forces. *Advances in Colloid and Interface Science* **74**, 119.

Wnek, W. J., D. Gidaspow and D. T. Wasan (1975). Role of colloid chemistry in modeling deep bed liquid filtration. *Chemical Engineering Science* **30**(9), 1035.

Yang, C., T. Dabros, D. Q. Li, J. Czarnecki and J. H. Masliyah (1998). Kinetics of particle transport to a solid surface from an impinging jet under surface and external force fields. *Journal of Colloid and Interface Science* **208**(1), 226.

Yang, C., T. Dabros, D. Q. Li, J. Czarnecki and J. H. Masliyah (1999). Analysis of fine bubble attachment onto a solid surface within the framework of classical dlvo theory. *Journal of Colloid and Interface Science* **219**(1), 69.

Yao, K. M., M. M. Habibian and C. R. Omelia (1971). Water and waste water filtration - concepts and applications. *Environmental Science and Technology* **5**(11), 1105.

Zienkiewicz, O. C., Taylor R. L. Zhu J. Z. (1989). *The finite element method : its basis and fundamentals.* Elsevier Butterworth-Heinemann. Oxford; Boston.